Department of Physics and Astronomy
Ruprechts-Karls-University Heidelberg

Bachelor Thesis in Physics
submitted by

Jonas Werner Danisch

born in Nagold (Germany)

2022

Search for the O_{16}^{4+}/O_{18}^{4+} isotope shift in the photoionization of Be-like oxygen with monochromatic soft X-ray synchrotron radiation.

This Bachelor Thesis has been carried out by Jonas Werner Danisch at the
Max Planck Institute for Nuclear Physics in Heidelberg
under the supervision of
Prof. Dr. José Ramon Crespo López-Urrutia

Abstract

Highly charged oxygen ions exist in astrophysical plasmas in a variety of charge states. The experimental investigation of the transitions of these ions in the soft X-ray region is therefore of great importance for the validation and improvement of astrophysical models. One of the strongest transitions is the K_α transition $1s^2 2s^2 \rightarrow 1s2s^2 2p_{3/2}$ of Be-like oxygen O^{4+}.
The aim of this work was to investigate this transition at $554\,\mathrm{eV}$ by resonant excitation with soft X-ray synchrotron radiation. The ions were produced and trapped in an electron beam ion trap and excited with synchrotron radiation from the Elettra synchrotron in Trieste, Italy. With the EBIT, both radiative decay channels and autoionizing decay channels can be measured in parallel. The charge state distribution is determined via a time-of-flight measurement, so that ions with different charges and masses can be resolved separately. This makes it possible to search for an isotope shift. In addition to searching for an isotope shift of O_{16}/O_{18} in the photoionization from the K_α transition of Be-like oxygen, the energy for this transition is determined absolutely in this work and compared with other sources.

Kurzzusammenfassung

Hochgeladene Sauerstoffionen kommen in astrophysikalische Plasmen in einer Vielzahl von Ladungszuständen vor. Die experimentelle Untersuchung der Übergänge dieser Ionen im weichen Röntgenbereich ist daher von großer Bedeutung für die Bestätigung und Verbesserung astrophysikalischer Modelle. Einer der stärksten Übergänge ist der K_α-Übergang $1s^2 2s^2 \rightarrow 1s2s^2 2p_{3/2}$ von Be-artigen Sauerstoff O^{4+}.
Ziel dieser Arbeit war es, diesen Übergang bei $554\,\mathrm{eV}$ durch resonante Anregung mit weicher Synchrotron-Röntgenstrahlung zu untersuchen. Die Ionen wurden in einer Elektronenstrahl-Ionenfalle erzeugt und eingefangen und mit Synchrotronstrahlung des Elettra-Synchrotrons in Triest, Italien, angeregt. Mit der EBIT können sowohl radiative Zerfallskanäle als auch autoionisierende Zerfallskanäle parallel gemessen werden. Über eine Flugzeitmessung wird die Ladungszustandsverteilung bestimmt, sodass Ionen mit unterschiedlichen Ladungen und Massen getrennt voneinander aufgelöst werden können. Dadurch ist es möglich, nach einer Isotopenverschiebung zu suchen. Neben der Suche nach einer Isotopenverschiebung von O_{16}/O_{18} in der Photoionisation von dem K_α-Übergang von Be-ähnlichem Sauerstoff wird in dieser Arbeit die Energie für diese Linie absolut bestimmt und mit anderen Quellen verglichen.

Contents

1 Introduction

Spectroscopy, literally translated from the Latin term "spectrum" for "image" and the Greek "skopein" for "to look at", describes the study of the interaction between matter and electromagnetic waves. With the help of spectroscopy, it is possible to gain insights into the physics of quantum mechanics, which is expressed in discrete energy levels of atoms, by observing only very specific emitted or absorbed wavelengths. In the modern sense, spectroscopy covers a multitude of methods which have the function of investigating atomic, nuclear and molecular transitions; determining the composition of substances or also providing diagnostics of it with regard to state parameters such as pressure, temperature or the degree of ionization.

One of the first to perform (absorption) spectroscopy and lay the foundation for what we call spectroscopy today, was Joseph Fraunhofer (1787-1826). In 1815 he investigated the dark lines in the solar spectrum, which had previously been observed independently by Wollaston in 1802. He catalogued these 574 lines - the so-called Fraunhofer lines - and marked the strongest lines with the capital letters A-K [13]. The origin of these lines and the reason why they are dark in the solar spectrum could not be solved by him. This riddle could only be solved about 50 years later in 1861 by Robert W. Bunsen (1811-1899) and Gustav Kirchhoff (1824-1887), who worked in Heidelberg. The reason for this was Bunsen's attempt to identify substances on the basis of the flame colour that is produced when they burn in the flame. By spectral analysis of the burning of different salts they found out that characteristic features in the solar spectrum could be assigned to emission lines of certain elements. They concluded that the Fraunhofer lines must be absorption lines and that the D line (actually a doublet line) comes from sodium [24].
Today we know that the solar spectrum can be regarded as the continuous blackbody radiation spectrum introduced by Max Planck in 1901 [41], where the Fraunhofer lines are the absorption lines of gases originating in the outer and relatively cold solar photosphere. The Fraunhofer lines can only be observed because it is made up of lightly ionized atoms that can interact with light. If atoms are so strongly ionized by higher temperatures that they lose all electrons, they can no longer interact with light and become transparent to light. They disappear in the absorption spectrum. This is the case, for example, for hydrogen and helium in the hotter core of the sun. Since in the case of heavy ions the ionization energies necessary to lose all electrons are greater due to the strong attraction of the remaining electrons to the more positively charged nucleus, these elements, like iron, manage to retain some of their electrons. These are called highly charged ions (HCIs) [16]. In contrast to the Fraunhofer lines found in the visible electromagnetic wavelength range, the inter-shell transitions produced by highly charged ions are usually in the soft X-ray regime or even higher in energy. However, when searching for X-ray sources in space, it must be noted that the Earth's atmosphere absorbs electromagnetic waves in the X-ray region almost completely, such that the observation point can no longer be on Earth. X-ray astronomy has been of great interest because most of the visible matter in the universe, also called ordinary or baryonic matter, occurs up to 99% in highly ionized states [26] and therefore, emits and absorb in the X-ray regime.

In the search for X-ray sources in space, such a source was identified for the first time at the end of the 1940s. Using X-ray detectors on a converted V2 rocket, the Naval Research Laboratory succeeded in identifying the Sun's corona as the first cosmic X-ray source [25]. Since the detectors available in the 60 years were too insensitive, no other X-ray sources outside the sun could be detected at first. It was not until 1962 that a second astronomical X-ray source was identified, which was discovered by chance by R. Giaconni. He observed the X-ray binary Scorpius X-1 with a Geiger Müller counting tube on an Aerobee rocket when he originally wanted to measure the sun's X-rays reflected from the lunar surface

[15]. In 1971, the first X-ray satellite Uhuru was launched, which scanned the entire sky for X-ray sources for the first time and discovered 339 sources. Other X-ray telescopic satellites followed, such as the Einstein Oberservatory (1978) [19] or the NASA Chandra X-ray Observatory and ESA's XMM-Newton [40, 43] at the end of the 90s, which are still active today. The special feature of the last two was the fact that charged-coupled devices (CCD) were used for the first time, which significantly increased the resolution of the measurable spectra. With these telescopes, it was possible to identify around 150,000 X-ray sources at the end of the 1990s.

With the possibility of precision measurements of absorption and emission spectra from astronomical X-ray sources, the demand for experimental precision measurements of highly charged ions has grown. With the help of laboratory measurements, the production, storage and interaction of highly charged ions with electrons and photons can be measured with a high possible accuracy, which can then be incorporated into improved astronomical models. One of the most important astrophysical elements besides iron, which has been studied in [26, 51], is oxygen. Its the most abundant element in gas with solar like composition [37]. How important oxygen HCIs are for astrophysical models becomes clear in the "riddle of the missing baryons". It has been known for decades that the number of baryons that must have existed at the beginning of the universe, predicted by big bang nucleosynthesis, does not correspond to the number of baryons measured in the local universe today. The number of baryons found today in stars, cold or warm interstellar matter, hot intracluster gas or residual photoionized intergalactic medium is between $30\% - 40\%$ below the expected value [37, 36]. One theoretical solution, found with the help of a numerical astronomical model, predicts the absence of baryons in the form of HCIs within hot and tenuous filamentary gas between galaxies. According to the leading model of cosmological structure formation [37], it was predicted that during the structure formation of the universe, diffuse baryons in the intergalactic medium condense into a filamentary network - the so-called warm-hot intergalactic medium (WHIM). The tenuous WHIM is a plasma with a low baryon density and has a temperature between $T \approx 10^5 - 10^7\,\mathrm{K}$. At these temperatures, hydrogen, the main component of the WHIM, is ionized and can no longer interact with light. Other elements are also ionized that the WHIM can only interact with far-ultraviolet (FUV) and soft X-ray photons. At the same time, the low baryon density makes it difficult to detect HCI. Mainly light interacts with lines of highly ionized (Li-like, He- like, or H-like) C, O, Ne, and Fe. With 80% of the total WHIM temperature range, He-like oxygen O^{6+} is the dominant ion. But also Li-like oxygen O^{5+} is important [37]. Nicastro et al. [36] published the first two very significant observations of two absorbers of highly ionized He-like oxygen K_α and K_β, both of which point to the missing baryons.

The lines of lower charged oxygen HCIs (O^{4+} and down) can also be important. These are hardly visible in the emission spectrum due to the fact that in the excited state they decay dominantly via autoionization instead of photon emission, but they can result in deep spectral absorption features [3]. With the knowledge of such absorption features, for example, the flow velocity of plasmas moving around galatic nuclei can be determined. These calculations are based on measuring the Doppler shift of a given absorption line in the absorption spectrum of the galatic nuclei. For this, the wavelength of a specific transition at rest must be known as precisely as possible. Theoretical calculations of complex HCI systems often have larger inaccuracies than the observational inaccuracies of the telescopes [3]. As these are greatly improved with upcoming X-ray telescopes such as XRISM, which are equipped with high-precision microcaliometers, the need for high-precision laboratory measurements is becoming urgent in order to take full advantage of the high-quality observational data. However, the few experimentally determined results available, e.g. of the K_α transition of $1s^22s^2 \rightarrow 1s2s^22p_{3/2}$ Be like oxygen at $554\,\mathrm{eV}$ determined

in Gu et. al. 2005 [18] but also McLaughin et. al. 2016 [33] determined significant differences in resonance energy ($> 100\,\mathrm{meV}$).

Therefore, it will be part of this work to excite these transition resonant with soft X-ray synchrotron radiation and perform a total energy calibration for this line. In addition, an isotopic shift of O_{16}/O_{18} is searched for in the photoionization with the same line of Be-like oxygen.
To perform this measurement, a light source is required that can provide soft X-ray radiation with sufficient flux and a production and storage facility for the HCI to be investigated. Since standard table-top lasers cannot provide sufficient flux in the soft X-ray range [51] monochromatised synchrotron radiation is used. Therefore, in this work the Elettra synchrotron in Trieste is used as a light source to excite highly charged ions resonantly produced and trapped in a compact electron beam ion trap (EBIT). As the maximum available beamline resolution of the used gas phase beamline, a resolution of up to 10000 [53] is possible in the used energy interval at $540\,\mathrm{eV}$. This is higher than the resolution of most X-ray detectors at space observatories. At the same time, the EBIT is able to control the maximum available charge state of an element and determine the charge state distribution, which is obtained with a time-of-flight measurement. Thus, in addition to the detection of photoionization, ions with different charges and masses can be resolved separately. The detection of photoionization is especially relevant for the K_α transition of Be-like oxygen, since the excited state decays mainly by autoionization. The resolving of ions with different charges and masses makes it possible to search for an isotope shift.

The first chapter deals with the theoretical basics that are necessary for understanding this work. With the second chapter, the functionality and structure of the PolarX EBIT used in the experiment is described. Emphasis is placed on the detection system, which is used to detect photons and ions. Before the analysis takes place, the working principle of a synchrotron is explained, as well as the GasPhase beamline used with its important parameters for the experiment.

2 Theory

In the framework of this thesis, an electron beam ion trap (EBIT) has been utilized to study the interaction of highly charged ions (HCI) with monochromatic synchrotron radiation. It is able to ionize atoms, store them and measure their interaction with electrons or photons. Highly charged ions have lost a considerable amount of bound electrons in comparision to their neutral counterparts. HCIs have a different energy level structure because of, among other things, various effects such as the fine structure and the Lamb shift being significantly enhanced in HCIs. Before discussing and understanding the physics of HCI as well as its fundamental interactions with photons and electrons within the EBIT in the second half of this chapter, a theoretical foundation of modern atomic physics is necessary. Therefore, the first half of this chapter first discusses the basic atomic structure of single-electron, followed by a discussion of multi-electron systems, including the methods by which they can be calculated.

2.1 Atom structure

In 1897, the British physicist Joseph J. Thomson (1856-1940) proved that atoms are by no means indivisible, as defined in the philosophical conception of antiquity (Greek "átomos": indivisible), by showing through scattering experiments with an electron beam on matter that smaller, electrically charged particles can be knocked out of atoms - the electrons [49]. This gave rise to the so-called raisin cake model, which states that these electrons, like raisins in a cake batter, are embedded in the evenly distributed mass of the positively charged atom.
Not even 15 years later, in 1911, Ernest Rutherford (1871-1937) revolutionized this picture. He was able to show, by the scattering of ${}^4_2He$ nuclei with a thin gold foil, that the mass in atoms is by no means as evenly distributed as Thomson assumed, but that there is a small ($\approx 10^{-15}\,\mathrm{m}$) positively charged nucleus which contains almost the entire mass of an atom [42]. Rutherford showed that the atom consists of a positively charged core, which is surrounded by a number of electrons equal to the total charge of the core. While being advanced for the time, Rutherfords model did not align with the laws of classical radiation physics, because accelerated charges radiate energy. An electron orbiting the atomic nucleus would therefore have to radiate energy constantly - and would consequently collide with the atomic nucleus. In 1913, the Danish physicist Niels Bohr (1885-1962) presented a model that provided an approach to solve this problem. He postulated a semiclassical model in which electrons can only move on certain classical paths around the atomic nucleus without emitting electromagnetic radiation: A change in energy is only possible through discrete jumps - either through emission or absorption of radiation [7]. The theory, which was initially postulated by Bohr, was not based on established physics. This laid the foundation for one of the fundamental theory of modern physics - quantum mechanics. Erwin Schrödinger developed wave mechanics in 1926, which is fundamental to quantum mechanics. The basis for this was provided on the one hand by the astonishing observation that elementary particles sometimes behave like particles, sometimes like waves, and on the other hand by Louis deBroglie's consideration that every particle can be assigned a wavelength $\lambda = h/p$. In contrast to Bohr's idea that electrons move as small spheres on elliptical orbits, the modern understanding of electrons assumes particles that can no longer be localized and can only be described using wave functions $\psi(\vec{r}, t)$. Each wave function represents a state of the system and can change over time. $|\psi(r, \theta, \phi)|^2$ gives the time-averaged spatial probability that the electron is located at the position $\vec{r}$ according to the Bohr's probability interpretation.

The wave functions can be calculated with the Schrödinger equation [44, 45, 46], which describes the temporal change of the wave function due to the action of a Hamiltonian $\hat{H}$:

$$\hat{H}\psi(\vec{r},t) = \underbrace{\Big[\frac{-\hbar^2}{2m}\nabla^2 + V(\vec{r},t)\Big]}_{\hat{H}=\hat{H}_{\mathrm{kin}}+\hat{H}_{\mathrm{pot}}}\psi(\vec{r},t) = i\hbar\frac{\partial}{\partial t}\psi(\vec{r},t) \tag{1}$$

where $\hat{H}$ is the Hamilton operator. It is the sum of the kinetic $\hat{H}_{\mathrm{kin}}$ and potential term $\hat{H}_{\mathrm{pot}}$ of the system. In addition, it can be extended by interaction terms, such as the interaction term of an electron with an external field or the Coulomb interaction between the electrons of a system. In the case of a time-independent potential $V(\vec{r})$, the wave function can be separated into a space and time dependent part: $\psi(\vec{r},t) = \psi(\vec{r})\chi(t)$. In this way, the Schrödinger equation can be transformed into a time-independent form.

$$\hat{H}\psi(\vec{r}) = E\psi(\vec{r}) \tag{2}$$

The solutions $\psi(\vec{r})$ of the time-independent Schrödinger equation are the steady states with time evolution $\chi(t)$, where the eigenvalue E of the Hamilton operator describes the energy of the system. For the time development follows directly $\chi(t) = e^{-iEt/\hbar}$.

2.1.1 Hydrogen

The hydrogen atom is the simplest many-particle system and at the same time the only one that can be solved analytically. The system consists of a nucleus (location $\vec{r_2}$, mass: M) with a proton and an electron (location $\vec{r_1}$, mass: m_{e}), which is located in the central potential $\phi(r) = \frac{Ze}{4\pi\epsilon_0|\vec{r}|}$ with distance $|\vec{r}| = |\vec{r_1} - \vec{r_2}|$ to the nucleus. The Schrödinger equation for such a system is [10]:

$$-\frac{\hbar^2}{2m_{\mathrm{e}}}\nabla_1^2\psi(\vec{r_1},\vec{r_2}) - \frac{\hbar^2}{2M}\nabla_2^2\psi(\vec{r_1},\vec{r_2}) - \frac{Ze^2}{4\pi\epsilon_0|\vec{r}|} = E\psi(\vec{r_1},\vec{r_2}), \tag{3}$$

with $Z = 1$, elementary charge e, vacuum permittivity ϵ_0 and the distance r between the proton and the electron. The first term describes the kinetic energy of the electron, the second the kinetic energy of the nucleus and the third the potential energy $V(r) = -e\phi(r)$ of the coulomb interaction between the nucleus and the electron. If one transfers eq. 3 into the center of mass system and introduces the reduced mass $\mu = \frac{m_{\mathrm{e}}M}{m_{\mathrm{e}}+M}$, two separate equations result [10]. One describing the kinetic energy of the center of mass motion, whose solution is a plane wave with the de Broglie wavelength. The other equation describes the relative motion between nucleus and electron, which is identical to the Schrödinger equation of a particle in the spherical symmetric potential $\phi(r)$:

$$\Big[\frac{-\hbar^2}{2\mu}\nabla^2 + V(r)\Big]\psi(\vec{r}) = E\psi(\vec{r}). \tag{4}$$

where the first term in the bracket describes the kinetic energy and the second term the potential energy. Eq. 4 can be solved analytically using a product approach, where $\psi(\vec{r})$ is split into a radial part $R_{nl}(r)$ and an angular part $Y_{lm}(\Theta,\Psi)$: $\psi(\vec{r}) = R_{nl}(r)Y_{lm}(\theta,\phi)$. Each wave function that solves eq. 4 solves is characterised by three so-called quantum numbers n,l,m. By inserting the product wavefunction in eq. 4 the radial wavefunction can be given as:

$$R_{nl}(r) = \sqrt{(\frac{2}{na_0})^3\frac{(n-l-1)!}{2n(n+l)!}}e^{-\frac{Zr}{na_0}}(\frac{2Zr}{na_0})^l L_{n+l}^{2l+1}(\frac{2Zr}{na_0}), \tag{5}$$

where a_0 is the classical Bohr radius $a_0 = \frac{4\pi\epsilon_0\hbar^2}{m_e e^2}$ and L_{n+l}^{2l+1} are the Laguerre Polynom. The solution for Y_{lm} are the spherical harmonics. Solving the Schrödinger eq. 4 with this solution yields the following eigenvalues:

$$E_n = -\frac{\mu e^4}{8e_0^2 h^2}\frac{Z^2}{n^2} = -R_y^*\frac{Z^2}{n^2}, \tag{6}$$

where R_y^* is the Rydberg constant. This result is identical to the semiclassical Bohr atomic model. Each set n, l, m_l characterises a unique wave function $\psi_{n,l,m_l}(\vec{r})$ with different spatial distribution representing certain level of the electron. The principal number $n = 1, 2, 3, ..., \infty$ indicates which shell (K,L,M,N,..etc.) the electron occupies in the Bohr atomic model. The orbital angular momentum quantum number l determines the magnitude of the orbital angular momentum $\vec{l}$ of the electron $|\vec{l}| = \sqrt{l(l+1)}\hbar$ where in addition $0 \leq l \leq n-1$ applies. The magnetic quantum number m_l gives the projection of the orbital angular momentum along a specified direction (in most cases z) $m_l = \frac{l_z}{\hbar} = -l, .., +l$. Since eq. 6 depends only on n, $\sum_{l=0}^{n-1}(2l+1) = n^2$ energetically degenerate levels exist. If in addition a magnetic field $\vec{B}$ is applied, the magnetic orbital moment $\vec{\mu_l} = -\frac{e}{2m_e}\vec{l}$ interferes with the B-field, resulting in an energy splitting of $\Delta E = -\vec{\mu_l}\vec{B}$. This is called the normal Zeeman splitting. If the B-field acts in the z-direction, $\Delta E = \mu_B m_l B_z$ applies, where $\mu_B = \frac{e\hbar}{2m_e}$ is the Bohr magenton.

Relativistic Correction (Finestructure)

So far, no relativistic effects have been taken into account. Electrons have the characteristic property of an intrinsic angular momentum $\vec{s}$ -the electron spin- with which a magnetic moment $\vec{\mu_s} \approx -2\frac{e}{2m_e}\vec{s}$ is associated. The electron spin $\vec{s}$ with spin quantum number $s = 1/2$ couples with the orbital angular momentum $\vec{l}$ to the total angular momentum $\vec{j} = \vec{l} + \vec{s}$ $(j = l \pm 1/2)$. Analogous to the orbital angular momentum, there exists a magnetic quantum number m_j, with $m_j = -j, ..., j$. If the electron is considered in its center of mass system, the nucleus orbits the electron and generates a magnetic field. The magnetic spin moment $\vec{\mu_s}$ interacts with the B-field produced in this way, analogous to the Zeeman effect, which again leads to a degeneracy of the levels. This correction, as well as the relativistic mass change of the electron and a third correction (Darwin term), are combined in the so-called fine structure correction. This makes eq. 6 also dependent on the total angular momentum quantum number j [10]:

$$E_{n,j} = E_n\Big[1 + \frac{(Z\alpha)^2}{n}\Big(\frac{1}{(j+1/2)} - \frac{3}{4n}\Big)\Big] \propto \frac{(Z\alpha)^4}{n^3}. \tag{7}$$

This result can be achieved as a direct solution of the Dirac equation, which is a relativistic version of the classical Schrödinger equation and was formulated by Paul Dirac in 1928 [26]. Another possibility to obtain eq. 7 is to add correction terms to the Hamiltonian. For example the spin orbit interaction correction Hamilton is as follows [51]:

$$\hat{H}_{s-o} = \frac{1}{2m_e^2 c^2}\frac{1}{r}\frac{dV}{dr}\hat{\vec{l}}\cdot\hat{\vec{s}}. \tag{8}$$

QED effects like vacuum polarization are not considered in finestructure. Further information can be found in [12, 26].

2.1.2 Many electron systems

Starting from the Hamilton operator of the single-electron system 4, the Hamilton operator of a multi-electron system can be constructed. This must contain all kinetic and potential terms of all single electrons and the interaction between the electrons $\hat{H}_{\text{interaction}}$ with distance $|\vec{r_{i,j}}| = |\vec{r_i} - \vec{r_j}|$.

$$\begin{aligned}\hat{H}_{\text{tot}} &= \hat{H}_{\text{kin}} + \hat{H}_{\text{pot}} + \hat{H}_{\text{interaction}} + \hat{H}_{\text{Corr}} = \\ &- \sum_{i=1}^{N}\left(\frac{\hbar^2}{2m_e}\nabla^2 - \frac{Ze^2}{4\pi\epsilon_0|\vec{r}|}\right) + \sum_{i<j}\frac{e^2}{4\pi\epsilon_0|\vec{r_i} - \vec{r_j}|} + \hat{H}_{\text{Corr}},\end{aligned} \tag{9}$$

where N is the number of electrons in the system. This Hamilton can be corrected with $\hat{H}_{\text{Corr}}$ depending on the degree of consideration of effects (e.g. spin-orbit operator $\hat{H}_{\text{s-o}}$).
If the interaction energy of all individual orbital angular momenta $\vec{l_i}$ or all individual spins $\vec{s_i}$ is large compared to the coupling energy between the spin and orbital angular momentum of an electron, i.e. the spin-orbit interaction is small, then the so-called LS coupling applies. For this purpose, all individual orbital angular momenta $\vec{l_i}$ and spins $\vec{s_i}$ are combined into a total orbital angular momentum $\vec{L} = \sum_i \vec{l_i}$ and a total spin $\vec{S} = \sum_i \vec{s_i}$. These couple in the spin-orbit interaction to a total angular momentum $\vec{J} = \vec{L} + \vec{S}$ [10].
The energy fine structure splitting between the maximal an minimal total angular momentum of the system $\Delta E_{FS} = E_{J_{max}} - E_{J_{min}}$ is small compared to the energetic distance of terms with different L and S. This is especially valid for light atoms. For heavy elements, the fine-structure splitting (interaction between the spin and orbital angular momentum of a single electron) dominates because of larger distances so that now the jj coupling holds: $\vec{J} = \sum_i \vec{j_i} = \sum_i \vec{l_i} + \vec{s_i}$.

Configuration, Term, Level and State

It is useful to briefly explain the differences between configuration, level and state. A configuration refers to a multi-electron system. It describes the position of each electron with its principal quantum number n and orbital quantum number l. For example, the ground state of a lithium-like system is in the configuration $1s^2 2s^1$. The "term" gives the total spin S or orbital momentum L, fixed at ${}^{2S+1}L$. The LS coupling is assumed here. Each term has $2S+1$ levels (fixed L, S and J) if in addition the fine structure, i.e. the spin-orbit interaction, is taken into account. $2S+1$ is also called multiplicity M. Each level in turn has $2J+1$ states when a magnetic field is applied (Zeeman effect). In fig. 1, the difference between the mountains for a $n_1 p, n_2 p$ configuration is shown schematically.

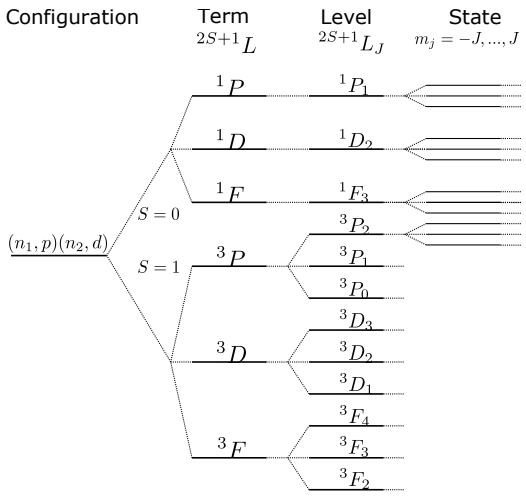

Figure 1: Overview: Configuration, Term, Level and State

2.1.3 Hartree-Fock method

An exact analytical solution of the Schrödinger equation is only possible for the hydrogen atom or single-particle systems. In order to obtain a multi-electron wave function $\Psi(\vec{r_1}, \vec{r_2}, .., \vec{r_N})$ for a certain state of a configuration, a simplification must be made in order to reduce the problem to a single-electron problem. For this purpose, the Coulomb interaction of the N electrons with respect to one electron is summarised in an effective potential ϕ_{eff}, in which the single electron can move independently of the location of the other electrons [10]. This results in a one-dimensional problem, and the Schrödinger equation can be solved for each electron with the spherical effective potential. This method is the so-called Hartree method [20]. It results in the single particle wave function $\psi_i(\vec{r_i})$ with fixed single electron quantum numbers $n_i, l_i, m_{l,i}, m_{s,i}$. If all N single wave functions are multiplied, the total wave function $\Psi(\vec{r_1}, \vec{r_2}, .., \vec{r_N})$ is obtained for a certain state k and electron configuration with the fixed quantum numbers n, l, m_l, m_s with the energy E_{n,l,m_l,m_s}:

$$\Psi(\vec{r_1}, \vec{r_2}, .., \vec{r_N}) = \prod_{i=1}^{N} \psi_i(\vec{r_i}) \tag{10}$$

To obtain the one-electron wave function $\psi_i(\vec{r_i})$, a spherically symmetric effective potential of

$$\phi_i^{(0)}(r_i) = -\frac{e}{4\pi\epsilon_0}(\frac{Z}{r} - ae^{-br}) \tag{11}$$

is first assumed, where a and b must be adjusted. The solution of the Schrödinger equation $\psi_i^{(0)}$ with this potential differs only in the radial part from the solution of hydrogen. Subsequently, the found single-particle solution functions $\psi_i^{(0)}$ can update each single potential as follows [10]:

$$\phi_{\text{eff}}^{(1)}(r) = -\frac{e}{4\pi\epsilon_0}\Big[\frac{Z}{r} - \sum_{j\neq i}\int \frac{1}{r_{ij}}|\psi_j(\vec{r_j})|^2 d\tau_j\Big] \tag{12}$$

The potential takes into account the attractive potential of the nuclear charge (Z) as well as the screening of the time averaged charge distribution of the remaining electrons. With the help of the new potential, the Schrödinger equation can be solved again for all electrons. This iteration process according to the scheme:

$$\phi_{\text{i,eff}}^{(0)}(r_i) \rightarrow \psi_i^{(0)}, E_i^{(0)} \rightarrow \phi_{\text{i,eff}}^{(1)}(r_i) \rightarrow \psi_i^{(1)}, E_i^{(1)} \rightarrow ... \rightarrow \psi_i^{(final)}, E_i^{(final)} \Rightarrow \Psi(\vec{r_1}, \vec{r_2}, .., \vec{r_N}) \tag{13}$$

is now performed until the obtained eigenvalues converge to a minimum value. This is because the improved wave function always has lower eigenvalues than the unimproved one. However, the overall wave function must be antisymmetric against the interchange of two electrons (Pauli principle). Two electrons cannot have the same quantum number $n_i, l_i, m_{l,i}, m_{s,i}$. The requirement is not fulfilled with eq. 10. This can be achieved by the so-called Slater determinant. This method allows the construction of the wave function of a multi-particle system for a special configuration from the antisymmetric linear combination of all N single-particle wave functions.

$$\Psi(\vec{r_1}, \vec{r_2}, .., \vec{r_N}) = \frac{1}{\sqrt{N!}} \cdot \begin{vmatrix} \psi_1(\vec{r_1}) & \psi_1(\vec{r_2}) & \dots & \psi_1(\vec{r_N}) \\ \psi_2(\vec{r_1}) & \psi_2(\vec{r_2}) & \dots & \psi_2(\vec{r_N}) \\ \vdots & \vdots & \ddots & \vdots \\ \psi_N(\vec{r_1}) & \psi_N(\vec{r_2}) & \dots & \psi_N(\vec{r_N}) \end{vmatrix} \tag{14}$$

However, it must be noted that the Hartree Fock method still does not take relativistic effects into account. The so-called post-Hartree Fock methods take these effects into account and use the Dirac equation instead of the Schrödinger equation. Further information can be found in [12, 26].

2.1.4 Configuration Interaction

The Hartree-Fock method [48] uses single electron wave function $\psi_i(\vec{r_i})$ to construct an overall wave function $\Psi_k(\vec{r_1}, \vec{r_2}, ..., \vec{r_N})$ for a special state k and configuration with fixed quantum numbers. This method does not take into account the mixing of the possible configurations respectively the electron-electron interaction, which often leads to unacceptably large deviations. With the help of the configuration interaction (CI), this limitation can be removed by calculating the total wave function $\Psi_{\mathrm{CI}}(\vec{r_1}, \vec{r_2}, .., \vec{r_N})$ for a certain configuration and state from a finite linear combination of n configurations Ψ_k. Thus the result of eq. 14 can be improved. For the different configurations Ψ_k the Hartree-Fock method is used in each case:

$$\Psi_{\mathrm{CI}}(\vec{r_1}, \vec{r_2}, .., \vec{r_N}) = \sum_{k}^{n} c_k \Psi_k(\vec{r_1}, \vec{r_2}, .., \vec{r_N}). \tag{15}$$

If each configuration is taken into account, the solution is exact. This is also called complete CI. Since a complete set of configurations usually has an infinite number of configurations, the exact calculation is technically impossible. However, many configurations are negligible and can be sorted out based on specific rules. For more on this, see [51]. CI is used in the Flexible Atomic Code (FAC), which is used for the calculation of energy levels and transitions in this work [17].

2.2 Highly Charged Ions

If an atom loses a large part of its bound electrons, one speaks of highly charged ions (HCIs). In most cases, highly charged ions are produced by stepwise ionization, usually with electrons. The degree of ionization q_+, from which an atom is considered to be highly charged [26], has not been clearly clarified in the literature. HCIs are usually called the atom which has as many electrons in the new state as the HCI. For example, if an oxygen atom with originally 8 electrons loses 4 electrons, it is called a Be-like atom O^{4+}. In spectroscopy, the roman representation is also used, in which the neutral atom has the charge state I and increases with a constant degree of ionization. In the previous example for Be-like Oxygen O^{4+} it would be O_{V}. In total, each element with the nuclear charge number Z has $Z+1$ charge states (isonuclear sequence). If the ions with the same electron number but different Z are compared, this is described as the isoelectronic sequence [16]. This is primarily because as z increases on the isoelectric sequence, the Coulomb potential for each electron changes. The closer the electron is to the nucleus, the more it is influenced by the nuclear charge number. Also on the isonuclear sequence, the electrons are influenced differently with increasing charge Q (fewer electrons), because the shielding of the remaining electrons on a single electron becomes smaller and thus the influence of the nuclear charge becomes larger (different Z_{eff}). The dependence of the energy structure for hydrogen-like systems is directly expressed in eq. 6 and eq. 7. There, the energy levels with different principal quantum numbers scale with Z^2, whereas the fine structure even scales with Z^4. These relations are generally also valid for all other HCI [16].
The dependence of the energy structure on the effective nuclear charge Z_{eff} also affects the ionization energy E_{B}, which describes the energy required to remove the weakest bound electron. E_{B} of HCI scales with Z^2 on the isoelectric sequence, while on the isonuclear sequence the dependence on Q (respectively

Z_{eff}, since fewer electrons contribute to the shielding as Q increases) is smaller and less smooth [16]. The latter is due to the fact that when a shell is changed, the distance of the outer bound electron is reduced and thus the energy level of the outermost electron and E_{B} increases significantly. Table 1 shows the ionization potentials for different HCI.

Table 1: Ionization energy in eV for HCIs in the range from q = 0 to q = 8, data from [2]. One column corresponds to an isonuclear sequence. The diagonals correspond to the isoelectronic sequence.

Charge	H	He	Li	Be	B	C	N	O
1^+	13.6	24.59	5.39	9.32	8.3	9.0	11.5	13.61
2^+		54.42	75.64	18.21	25.15	21.7	26.2	35.15
3^+			122.45	153.89	37.93	47.89	43.9	54.93
4^+				217.71	259.31	64.49	77.48	77.39
5^+					340.24	392.06	97.89	113.87
6^+						490.01	552.06	138.12
7^+							667.06	739.27
8^+								871.39

Due to the different influences of the effective nuclear charge Z_{eff} on the different energy levels, there is a separation of the energy levels and thus also different excitation energies of HCIs. This explains why HCIs show significantly larger energetic distances of the transitions compared to their neutral or less charged ions. As a rule, the transitions are in the soft X-ray range or even higher energy ranges.
Also, the decay probability of an excited HCI to decay via a radiative or autoionizing decay depend on the nuclear charge Z. As mentioned in the introduction, HCIs play an important role in astrophysics because visible matter in the universe occurs in highly ionized states up to 99%. An accurate measurement of the energy level of HCI is therefore of extraordinary importance for astrophysical models.

2.3 Isotope Shift

The atomic structure of an ion does not only depend on the properties of the charged particles, but also on the mass and size of the nucleus. A different nuclear mass M and a different shape of the nucleus causes a change in energy, which leads to an energy shift of the energy levels. This shift is also called isotope shift. The contribution to the shift caused by the different masses M of the nucleus is called mass shift. The mass shift can be easily identified in the two-body problem (see section 2.1.1), since the reduced mass depends on M. This is also true for multi-electron systems. The shift caused by the different size and shape of the nucleus is called field or volume shift. The change in the mass distribution in the nucleus, which occurs in isotopes due to the different number of neutrons, also causes a change in shape and size of the charge distribution in the nucleus. This has an influence on the potential of the electrons, which in turn changes the energy structure.

2.3.1 Mass Shift

As discussed in the two particle problem, the energy of the levels depends on the reduced mass $\mu = m_0 M/(m_0 + M)$ of the system, with the nuclear mass M and the rest energy m_0 of the electron. In the case of a multiple electron system, the electron-electron interaction must be taken into account, which causes an additional shift. A commonly used approximation, first described by Hughes and Eckart

[22], is to separate the influence of the nuclear mass into two parts, the normal mass shift (NMS) and the specific mass shift (SMS). The latter describes contributions from a multi-body problem.
According to [52], the two associated Hamiltonians are as follows

$$H_{\mathrm{NMS}}^{\mathrm{nr}} = \frac{1}{2M}\sum_i \hat{\vec{p}}_i^2, \qquad H_{\mathrm{SMS}}^{\mathrm{nr}} = \frac{1}{2M}\sum_{i\neq j} \hat{\vec{p}}_i \hat{\vec{p}}_j. \tag{16}$$

where $\hat{\vec{p}}_i$ are the momentum operators. In contrast to H_{NMS} is H_{SMS} a two particle operator where i and j denote the electrons. Relativistic description can take place only in the framework of quantum electrodynamics, which was first carried out by Shabaev. He formulated a Hamlitonian

$$H_M^{\mathrm{rel}} = H_{\mathrm{NMS}}^{\mathrm{rel}} + H_{\mathrm{SMS}}^{\mathrm{rel}} = \frac{1}{2M}\sum_{ij}\Big[\hat{p}_i\hat{p}_j - \frac{\alpha Z}{r_i}(\vec{\alpha_{\mathbf{i}}} + \frac{(\vec{\alpha_{\mathbf{i}}}\cdot\vec{r_i})\vec{r_i}}{r_i^2}\cdot\hat{\vec{p}_j})\Big], \tag{17}$$

with which it is possible to calculate the mass shift in the lowest relativistic approximation order ($\approx (v/c)^2$) and in the first order in m_0/M. $\vec{\alpha}$ is the vector containing the Dirac matrices, α is the fine structure constant and $\hat{\vec{p}}_{i,j}$ is the four-momentum operator. The expectation value of H_M^{rel} regarding the Dirac wave function returns the mass shift. To calculate the mass isotope shift between two ions with masses m_1 and m_2, the difference between these expectation values of H_M^{rel} must be calculated with

$$\delta E_{\mathrm{MS}}^{\mathrm{rel}} = \Big\langle\psi\Big|H_{\mathrm{M1}}^{\mathrm{rel}}\Big|\psi\Big\rangle - \big\langle\psi\big|H_{\mathrm{M2}}^{\mathrm{rel}}\big|\psi\big\rangle = \big\langle\psi\big|H_{\mathrm{M1}}^{\mathrm{rel}} - H_{\mathrm{M2}}^{\mathrm{rel}}\big|\psi\big\rangle, \tag{18}$$

where $|\psi\rangle$ is the eigenvector of the Dirac-Coulomb Breit Hamiltonian [52].

2.3.2 Field Shift

From classical electrodynamics, it is known that a symmetric spherical charge distribution $\rho(r, R)$ outside its radius R can be considered as a point charge. Inside the charge distribution, the potential is different and depends on the location r. This explains the differences in the influence on electrons whose wave function extends into the charge distribution. Since isotopes have different atomic nuclear radii (different neutron number) and charge distributions, it follows that they have a different influence on the electrons and thus also on the energetic levels. The presence of other electrons affects the magnitude of the field shift only slightly [38]. The potential of an extended nucleus is given by

$$V_N(r,R) = -4\pi\alpha Z\int_0^\infty dr' r^2 \rho(r',R)\frac{1}{r_>}, \qquad r_> = max(r,r'), \tag{19}$$

where a Fermi model can be assumed for the nuclear charge distribution [52]. For the field shift then holds:

$$\delta E_{\mathrm{FS}}^{\mathrm{rel}} = \Big\langle\psi\Big|\sum_i \delta V_N(r_i,R)\Big|\psi\Big\rangle = \Big\langle\psi\Big|\sum_i V_N(r_i,R+\delta R) - V_N(r_i,R)\Big|\psi\Big\rangle, \tag{20}$$

where δR is the difference of the root-mean-square (rms) nuclear charge radius of the two isotopes.

In general, it can be said that the mass shift dominates for light atoms (small Z) and field shift for heavy atoms [52]. For heavier atoms, the ratio of $\Delta m_0/M$ decreases, so that the mass shift becomes less important. At the same time, the orbitals become smaller (due to the larger nuclear charge) and their overlap with the nucleus increases, such that the influence of the field shift increases.
This chapter is based on [52, 38] and can be read in more detail there.

2.4 Electronic and photonic processes

The interaction possibilities of electrons and photons with ions are diverse. Electrons as well as photons can excite bound electrons in an atom resonantly, lifting them to a higher state. If a free electron is captured (electron capture), the charge state of the atom is reduced by one. At the same time, an excited state can be deexcited by ionizing a less strongly bound electron (autoionization). If the excited atom deexcites itself via a photon, the charge state is conserved (radiative decay). Depending on the way in which an atom is excited, it is decided whether the atom will be ionized (Auger: first photonexciation then autoionization), recombine (dieletronic recombination: first electron capture then radiative decay) or retain its charge state (resonant scattering). So far, only resonant interactions have been considered. Non-resonant processes can also lead to ionization or recombiantion. In non-resonant photoionization, a photon excites an electron directly into the continuum. Unlike the two step DR process, this is a direct process. In the recombination process, a free electron is captured and a photon is released. Free electrons can interact with atoms in a non-resonant way via scattering processes by either exciting the bonded atom (electron excitation) or even ionizing it (electron impact ionization). The latter process is the most important ionization process within an EBIT. Before explaining both resonant and non-resonant ionization and recombination processes in this subchapter, the most important excitation and deexcitation processes are explained. These represent the components from which the resonant ionization and recombination processes are formed.

2.4.1 Excitation

Electron capture (DC) In the dielectronic electron capture process (DC), a free electron interacts with an ion in the state $|\Psi_i\rangle$ resonantly by being captured and while transferring its kinetic energy to a bounded electron, which is thereby lifted. The result is a doubly excited state $|\Psi_k\rangle$, since both the free electron is trapped at an energetically high energy level, and the bonded electron is excited. The charge of the ion is decreased. It holds

$$A^{q+} + e^- \rightarrow A^{[(q-1)+]**}, \tag{21}$$

while A^{q+} stands for a q-charged ion in the initial state and $*$ indicates the degree of excitation of the ion, so that $A^{[(q-1)+]**}$ is a doubly excited state. This nomenclature will be used throughout this subchapter. The kinetic energy of the electron has to include the energy it needs to lift the bonded electron (ΔE), minus the energy that is released when the electron is captured (bond energy E_{B}):

$$E_{\mathrm{Kin}} = \Delta E - E_{\mathrm{B}}. \tag{22}$$

The doubly excited state is not stable and decays (see chapter. 2.4.2). Electron capture as an excitation process is the reverse process to the autoionization process. In a non-relativistic view the capture rate $A_{\mathrm{DC}}^{i\rightarrow k}$

$$A_{\mathrm{DC}}^{i\rightarrow k} \sim Z^0 \tag{23}$$

of this process does not depend on the nuclear charge Z [4]. Electron capure is the reverse process to autoionsiation. The excitation rates and deexcitation rates of DC and Auger respectively, are coupled.

Photonexcitation (PE) Analogous to the resonant absorption of electrons, this can also happen with photons. If an atom in the state $|\Psi_i\rangle$ is in an electromagnetic radiation field with spectral energy density $\rho(\nu)$, it can absorb a photon with energy $h\nu$ and be excited to a higher state $|\Psi_k\rangle$ with energy $E_k = E_i + h\nu$.

$$A^{q+} + h\nu \rightarrow A^{(q+)*} \tag{24}$$

The probability for this transition process is proportional to the spectral energy density $\rho(\nu) = n(\nu)h\nu$, where $n(\nu)$ describes the number of photons in a volume per unit interval $\nu = 1\,\mathrm{s}^{-1}$ [10]. The proportionality factor is the so-called Einstein coefficient of induced absorption $B_{i,k}$. Thus, the probability that an atom absorbs a photon per second is given:

$$P_{i,k} = B_{i,k}\rho(\nu) \tag{25}$$

Multiplying $P_{i,k}$ by the number of ions present in state i gives the total absorption rate $A_{\mathrm{PE}}^{i\rightarrow k}$. This depends in the fourth power on the nuclear charge Z [4].

$$A_{\mathrm{PE}}^{i\rightarrow k} = P_{i,k}N_i \sim Z^4 \tag{26}$$

The photon absorption rate is closely related to the photon emission rate, since photon emission is the conversion process to photon excitation.

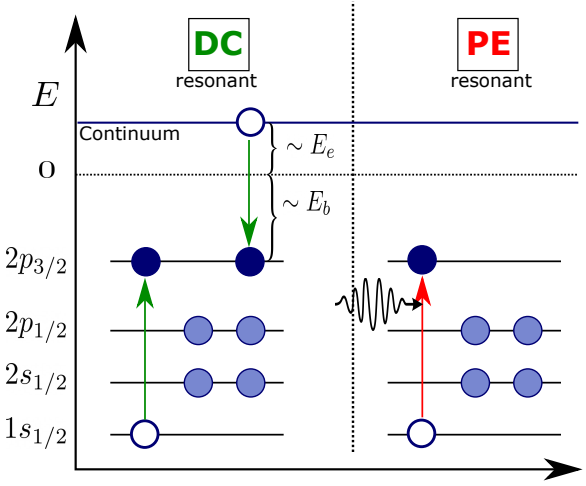

Figure 2: Overview of two possible excitation processes: Electron Capture (DC), Photon exciation (PE).

2.4.2 Deexcitation

Radiative decay (RD) Radiative decay describes the deexcitation of an excited atom, in which an electron falls into an energetically more attractive level, emitting a photon. It corresponds to the inverse process of photon excitation.

$$A^{(q+)*} \rightarrow A^{q+} + h\nu \tag{27}$$

Analogous to photon absorption, a radiation field can also induce the emission of a photon, whereby the excited state is deexcited and emits another photon. The inducing photon has the same energy and direction as the emitted photon $h\nu = \Delta E$. As with photon excitation, the probability of this process taking place can be described with the help of the Einstein coefficients of induced emission $B_{k,i}$.

$$P_{k,i}^{IE} = B_{k,i}\rho(\nu) \qquad P_{k,i}^{SE} = A_{k,i} \tag{28}$$

An atom can also be deexcited without the presence of an external field and with random direction. $A_{k,i}$ is the Einstein coefficient of spontaneous emission. In the stationary case, the absorption rate must be equal to the emission rate: $B_{i,k}N_i = (B_{k,i}\rho(\nu) + A_{k,i})N_k$
where N_i,N_k is the number of atoms in the respective state. If we now take advantage of the fact that the Boltzman distribution holds for the population numbers of the states in thermal equilibrium, we can derive an expression for $\rho(\nu)$, which may be simultaneously equated with the Planck formula. It follows [11]:

$$B_{i,k} = B_{k,i}\frac{2J_k + 1}{2J_i + 1} \qquad A_{k,i} = \frac{8\pi h\nu^3}{c^3}B_{ki} \tag{29}$$

$2J + 1$ describes the statistical weight, i.e., the number of energetically degenerate sublevels. From eq. 29 it can be seen that for equal statistical weights $g_i = g_k$ the Einstein coefficients for induced emission and absorption are equal. For the total radiation decay rate $A_{\mathrm{RD}}^{k\rightarrow i}$ the following applies

$$A_{\mathrm{RD}}^{k\rightarrow i} = (P_{k,i}^{\mathrm{IE}} + P_{k,i}^{\mathrm{SE}})N_k \sim Z^4 \tag{30}$$

Multiple states usually emit several photons, but it is also possible for several electrons to emit their energy via one photon. This is also called the "two electron one photon process" (TEOP) [4].

Autoionizing decay (AI) Another form of deexcitation is via an electron. This process is the reverse of resonant electron capture and competes with radiative decay. AI is part of the resonant Auger ionization process. In this process, an electron relaxes to a lower energetic state and the excess energy is transferred radiation-free to a less strongly bonded electron. When the released energy is above the ionization energy, the electron can leave the atom and ionize it.

$$A^{(q+)*} \rightarrow A^{(q+1)+} + e^- \tag{31}$$

Due to conservation of energy, the kinetic energy of the leaving electron is equal to the energy difference between the excited and the deexcited state minus the binding energy of the released electron.

$$E_{\mathrm{Kin}} = \Delta E - E_{\mathrm{B}} \tag{32}$$

As mentioned before, there is a relation between Autoionization rate $A_{AI}^{i\to k}$ and capture rate $A_{\mathrm{DC}}^{i\to k}$ [4]

$$A_{\mathrm{DC}}^{i\to k} = \frac{2J_k + 1}{2(2J_i + 1)} A_{AI}^{i\to k} \tag{33}$$

Thus, due to eq. 23, $A_{\mathrm{AI}}^{i\to k} \sim Z^0$ is also valid. If one compares this with eq. 30, then it can be seen that the radiative decay channel for highly charged ions on the isoelectric sequence ($\sim Z^4$) is more likely than the autoionizing one ($\sim Z^0$). So for more neutral atoms the autoionizing decay dominates. This is also true for HCI on the isonuclear sequence, since a higher charge state increases the effective nuclear charge potential of the remaining electrons, making radiative decay more likely for HCI on the isonuclear sequence here as well. This will play a role in the further course of the analysis.

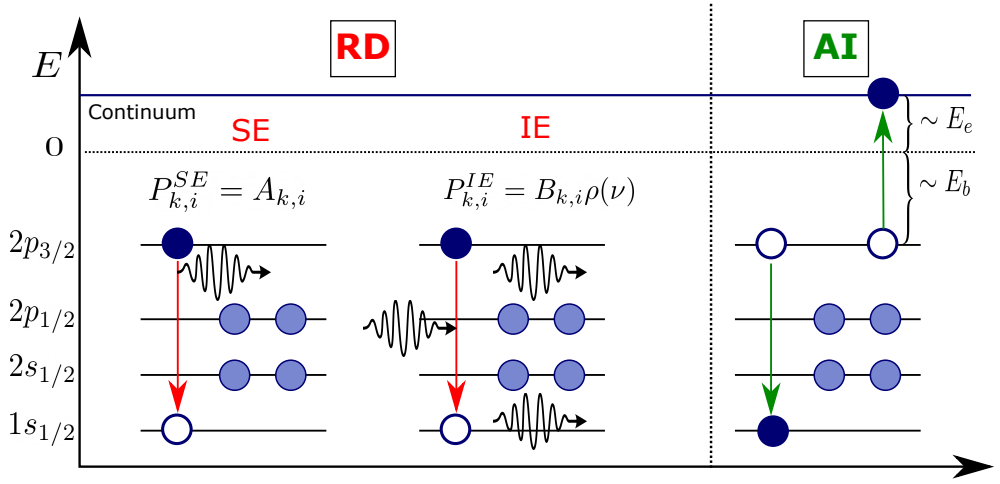

Figure 3: Overview of the two dexcitation processes: radiative decay (RD) with induced emission (IE), spontaneous emission (SE) and autoionization (AI).

2.4.3 Ionization

As mentioned earlier, the resonant ionization process is a two-step process consisting of a radiative excitation followed by an autoionization (Auger). The two non-resonant ionization processes are inelastic electron impact ionization and non-resonant photoionization, where a photon lifts a bound electron into the coontimuum. Electron impact ionization process is mainly responsible for the HCI in the EBIT due to the fact that there is an enormous current density of the electron beam ($\approx 10^4\,\mathrm{A\,cm^{-2}}$).
A typical assumed σ_{EII} crosssection of $\sigma^{\mathrm{EII}} \approx 10^{-16}\ \mathrm{cm}^{-2}$ leads, to an initial ionization rate in the range of MHz. This is much faster than any other process [14].

Electron impact ionization (EII) If free electrons with sufficient kinetic energy (E_{Kin}) interact with atoms, they can release bound electrons from the atom. This inelastic collision only happens as long as the ionization energy of the atom is not undercut. The reaction mechanism is described by:

$$A^{q+} + e^-(E_{\mathrm{e}}) \to A^{(q+1)} + e^-(E_1) + e^-(E_2) \tag{34}$$

Due to energy conservation follows: $E_\mathrm{e} - E_\mathrm{B} = E_1 + E_2$. As soon as E_Kin of the free electron is larger than the binding energy of an electron, it contributes to the total effective cross-section σ^EII. All electrons in a shell contribute to $\sigma^\mathrm{EII} = \sum_{i=1}^{N} \sigma_i$ where N is the number of subshells. $i = 1$ is the outermost shell, $i = 2$ is the the inner subshell etc. Typically, the general cross-section increases from zero to a broad maximum at about two to three times the ionization energy, after which it gradually returns to zero. With the help of the empirically determined Lotz formula [31, 32], this behaviour of σ^EII can be determined:

$$\sigma_i^\mathrm{EII} = a_i k_i \frac{ln(E_\mathrm{Kin}/E_{B,i})}{E_\mathrm{Kin} E_{B,i}} \Big\{ 1 - b_i exp\Big[-c_i (\frac{E_\mathrm{Kin}}{E_\mathrm{B}} - 1) \Big] \Big\}, \tag{35}$$

where $E_{B,i}$ is the binding energy of electrons in the i^{th} subshell, k_i is the number of electrons in subshell i and a_i, b_i, c_i are element dependent experimental values. For very high electron energies ($E_\mathrm{Kin} \gg E_{B,i}$), eq. 35 results in

$$\sigma_i^\mathrm{EII}[cm^2] = a_i k_i \frac{ln(E_\mathrm{Kin}/E_{B,i})}{E_\mathrm{Kin} E_{B,i}} = 4,49 \cdot 10^{-14} k_i \frac{ln(E_\mathrm{Kin}/E_{B,i})}{E_\mathrm{Kin} E_{B,i}} \propto \frac{ln(E_\mathrm{Kin})}{E_\mathrm{B}}. \tag{36}$$

If $E_\mathrm{Kin} < E_\mathrm{B} \rightarrow \sigma_i^\mathrm{EII} = 0$, ionization is no longer possible. As the charge state that has to be reached is higher, further ionization is more difficult, since E_B increases with increasing charge state. E_B will increase since the effective nuclear charge Z_eff, which keeps the electron to be removed bound, increases with increasing charge state. At about the ($E_\mathrm{Kin} \approx 2.3 E_{B,i}$), σ^EII reaches its maximum. However, since the next higher charge state is usually reached earlier than the maximum of the charge state to be reached, the equilibrium maximum is often somewhat below the maximum of the effective cross-section (higher excited state falls back) [16].

Auger (AU) In the two-step Auger process, the atom is excited by photoexcitation (PE) in the first step and then decays via the autoionizing decay channel (AI):

$$A^{q+} + h\nu \overset{\mathrm{PE}}{\rightarrow} [A^{(q+)}]^* \overset{\mathrm{Auger}}{\rightarrow} A^{(q+1)+} + e^- \tag{37}$$

Due to conservation of energy, the kinetic energy of the extracted electron is equal to the energy difference between the excited and the deexcited state minus the binding energy of the released electron.

$$E_\mathrm{Kin} = \Delta E - E_\mathrm{B} = h\nu - E_\mathrm{B} \tag{38}$$

As already mentioned, the autoionizing decay in HCI is weaker than the radiative one, in contrast to neutral atoms. A radiative excitation after a photonic resonant excitation corresponds to a resonant photon scattering.

Photoionization (PI) Non-resonant photoionization is a one-step process. The reaction mechanism is described by:

$$h\nu + A^{q+} \rightarrow A^{(q+1)+} + e^- \tag{39}$$

Direct photoionization can only take place as long as $h\nu > E_\mathrm{B}$. For the energy of the electron follows:

$$E_\mathrm{Kin} = h\nu - E_\mathrm{B} \tag{40}$$

Below the ionization energy E_{B}, the effective cross section of this process is zero. For $h\nu > E_{\mathrm{B}}$, applies to $\sigma_{\mathrm{PI}} \propto Z^5 E_\gamma^{-7/2}$ [4]. A special case besides direct photoionization would be the process in which several photons together release an electron. However, the probability of this process depends strongly on the number of photons required, which means that very high intensities are needed.

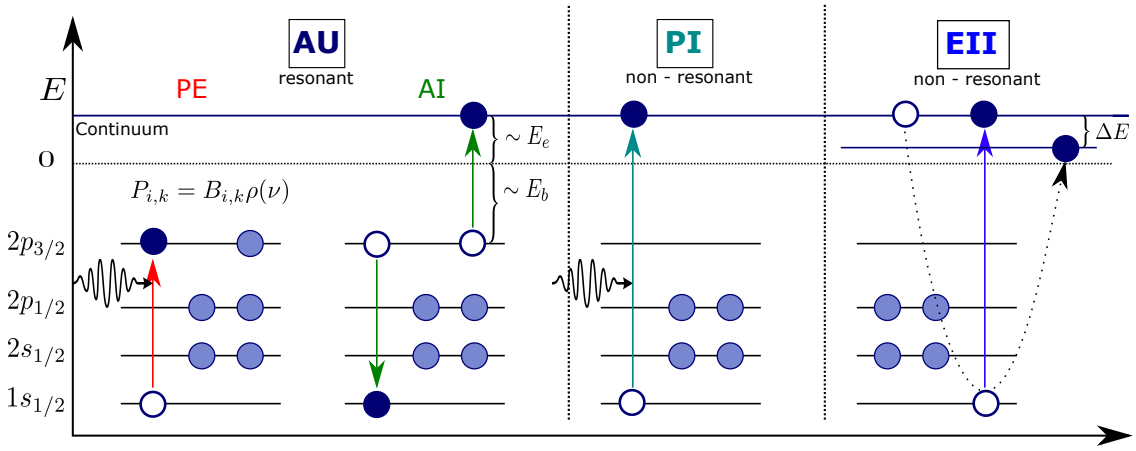

Figure 4: Overview of ionization processes: Augerprocess (AU), Photonionization (PI) and Electron impact ionization (EII).

2.4.4 Recombination

The reversal process of ionization is recombination. Similar to ionization, a distinction is made between (direct) recombination, i.e. the reversal process of non-resonant photoionization, and the resonant two-step process of dielectronic recombination. 2.4.4, the reversal process of an Auger process.

Radiative Recombination (RR) In radiative recombination, an ion captures a free electron non resonantly ($E_{\mathrm{Kin}} > E_{\mathrm{B}}$) and the energy released is radiated via a photon. This process is the reverse of photoionization.

$$A^{q+} + e^- \rightarrow h\nu + A^{(q-1)+} \tag{41}$$

Due to energy conservation, the photon energy is equal to the sum of the kinetic energy of the electron and the binding energy of the ion in the final state:

$$E_\gamma = h\nu = E_{\mathrm{Kin}} + E_{\mathrm{B}} \tag{42}$$

Dielectronic Recombination (DR) Dielectronic recombination is the reverse process of the Auger process, i.e. a two-step process in which first a free electron with a certain kinetic energy is captured in an ion (DC), whereby a bound electron is excited by the non-radiatively transfered energy. The double excited state is unstable and decays again radiatively (RD).

$$A^{q+} + e^- \overset{\mathrm{DC}}{\rightarrow} [A^{(q+1)+}]^{**} \overset{\mathrm{RD}}{\rightarrow} [A^{(q+1)+}]^{*} + h\nu \tag{43}$$

As described in 2.4.1, it holds that the kinetic energy includes the energy required to lift the bound electron (ΔE) minus the energy released when the electron is captured (binding energy E_{B}).

$$E_{\mathrm{e}} = \Delta E - E_{\mathrm{B}} \tag{44}$$

Thus, the energy of the emitting photon that changes to the ground state is also greater than that of the initial electron ($\Delta E = E_{\gamma} = E_{\mathrm{Kin}} + E_{\mathrm{B}}$). If the excited state would decay via autoionization, it would be resonant electron scattering. In the nomenclature of a DR process, the shell from which the bound electron is excited is usually given first, followed by the shell in the excited state and finally the shell in which the free electron was captured. For example, a KL-M Process describes the capture of a free electron into the M shell, where an electron from the K shell is excited into the L shell.

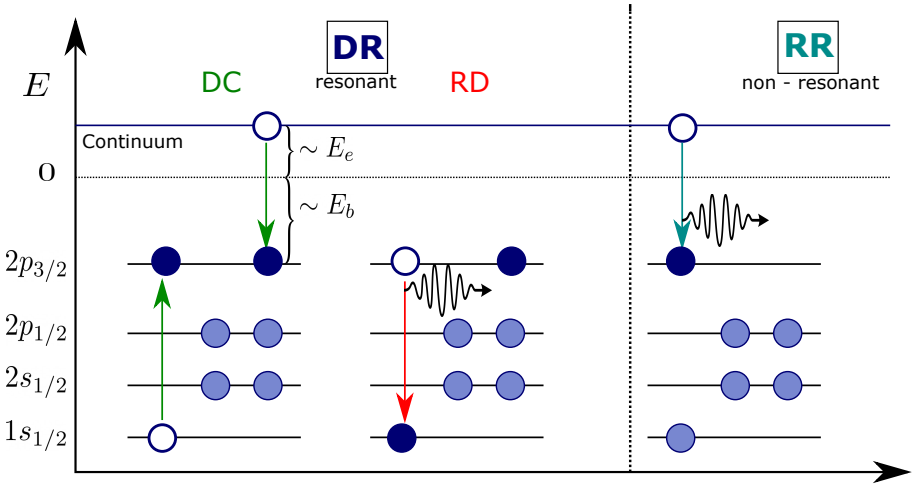

Figure 5: Overview of recombination processes: Dieletronic recombination (DR) and radiative recombination (RR)

3 EBIT

An electron beam ion trap (EBIT) is a tool for the production, storage and investigation of highly charged ions (HCI). To capture an HCI, one needs an electromagnetic field that traps the ion from all directions in space, i.e. that there is a restoring force as soon as the desired position is left. According to the Earnshaw theorem, this cannot be realised with a static purely electric or magnetic field [27]. There are two basic ways to trap particles. Either a time-varying electric field is used, as in the Paul trap, or a superposition of an electric and a magnetic field, as in the Penning traps or the EBIT. The EBIT is used in this work. This chapter first discusses the basic operating principle of the general EBIT and then describes the PolarX EBIT used in this work specifically. Here, both the individual components and the detection system are discussed.

3.1 Basic principle

In order to be able to trap HCI, they must first be produced. A very efficient way for the ionization of ions to do this is as described in section 2.4.3 by electron impact ionization (EII). With a typical assumed σ_{EII} crosssection of $\sigma^{\mathrm{EII}} \approx 10^{-16}\ \mathrm{cm}^{-2}$ initial ionization rate in the range of MHz can be reached. For this purpose, a monoenergetic beam produced by an electron gun is used, which ionizes the atoms by electron impact. Since the effective cross-section σ_{EII} decreases for each further ionization, the current density should be as high as possible to achieve the maximal possible ionization rate. To achieve this, a magnetic field concentrically aligned to the trap axis is used to compress the electron beam towards the trap center, as an increasing Lorentz force leads to smaller cyclotron radii. Since the electrons always have a velocity component perpendicular to $\vec{B}$ due to both the thermal motion and the mutual repulsion, a cyclonic motion occurs. Without a magnetic field, the beam would diverge rapidly because the electrons would repel each other. This results in an extremely high current density in the order of $10^4\,\mathrm{A\,cm}^{-2}$ within the trap, leading to an electron density of $10^9 - 10^{10}\,\mathrm{cm}^{-3}$ and an almost equally high positive charge density of ions $10^5 - 10^6\,\mathrm{cm}^{-3}$. In addition to the function of ionizing the atoms, the electron beam has the ability to trap ions radially through its produced space charge potential. The entire EBIT is operated in an ultra high vacuum to ensure that the electron beam reaches the inside of the trap without having completely interacted with atoms outside the trap chamber. The timescale in which neutral atoms move at thermal velocities is in the order of microseconds or less [14]. Figure 6 shows the basic working principle of an EBIT.

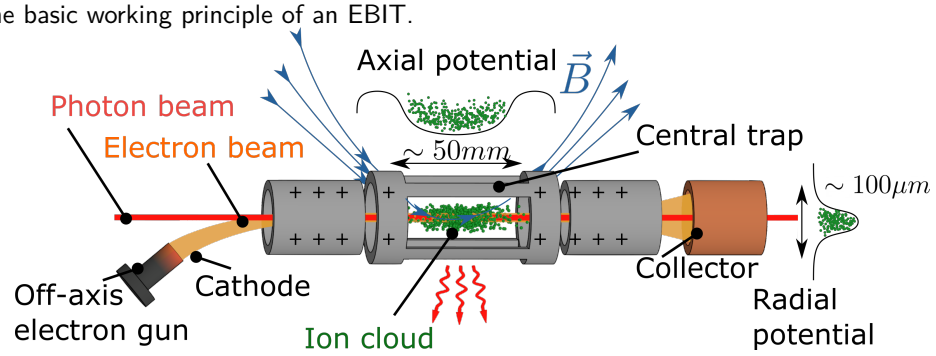

Figure 6: EBIT working principle: The magnetic field (blue) compresses the electron beam (orange) from the electron gun, resulting in a high current density in the trap enclosed by the outer drift tubes. This ionizes the atoms, which are trapped both radially by the magnetic field and electron beam and axially by the drift tube. Adopted and modified from [28]

Both the space charge potential ("line charge") generated by the electron beam and the cyclone motion trap the ion radially. Up to now, however, the ions can still break out axially, i.e. alongside the electron beam. This is prevented with the help of edge potentials that are applied in the so-called drift tubes. The ions are trapped axially by the voltage difference between the trap and the neighbouring electrodes. Together with radial trapping, this leads to the storage of the ion cloud formed by the electron beam with a radius of a few tens of micrometres, a length of a few millimetres and a temperature of $10^5 - 10^7\,\mathrm{K}$. The trap can be emptied by reversing the axial trap potential. After the electrons have left the drift tube assembly, they are collected on a collector electrode. The ratio of the current arriving at the collector to the emission current of the electron gun is called transmission.

3.2 Electron beam

The electron beam is produced by a heated cathode inside an electron gun. The size of the electron beam, which is compressed as described above due to the Lorentz force, can be determined with the approximations of Hermann [21]. This approximation takes into account the repulsive Coulomb interaction, the temperature of the cathode, as well as the cyclotron motion, which is dependent on the thermal motion of the electron v:

$$r_\mathrm{H} = \sqrt{\frac{m_e I}{\pi\epsilon_0 e v B^2} + \sqrt{\left(\frac{m_e I}{\pi\epsilon_0 e v B^2}\right)^2 + \frac{8 k_b T_\mathrm{C} m_e}{e^2 B^2} r_c^2 + \frac{B_\mathrm{C}^2}{B^2} r_\mathrm{C}^4}}, \tag{45}$$

, where I is the beam current, v the velocity of the electrons, B the magnetic field inside the trap, B_C the magnetic field at the cathode, T_C the temperature of the cathode, r_C the radius of the cathode, k_b the Boltzmann constant and e the elementary charge of the electron. Within this radius 80% of the electronic current I. can be found. It becomes clear that the magnetic field at the cathode should be as close to zero as possible and that inside the trap the field should be maximal. The velocity of the electrons can be calculated with relativistic considerations

$$v_\mathrm{el} = c\sqrt{1 - \frac{1}{\left(1 + \frac{qU}{m_e c^2}\right)^2}}, \tag{46}$$

where c is the light velocity and U is the acceleration potential between the cathode and the trap. Taking typical values for an EBIT, used within the scope of this work, $B = 0.86\,\mathrm{T}$, $B_\mathrm{C} \leq 100\,\mu\mathrm{T}$, $T_\mathrm{C} = 1400\,\mathrm{K}$, $r_\mathrm{C} = 3.4\,\mathrm{mm}$, $I = 80\,\mathrm{mA}$ and $U = 5\,\mathrm{keV}$, we get a diameter of $r_\mathrm{H} = 72\,\mu\mathrm{m}$ according to eq. 45 [35].

3.3 Potential

The electrostatic potential acting inside the EBIT, which is responsible for both the trapping of the ions and the movement of the electrons, is the superposition of several contributions. On the one hand, there is the negative space charge potential Φ_e of the electrons, which binds the positively charged ions. Φ_e is given as the solution of the Poisson equation

$$\vec{\nabla}^2 \Phi_e = -\frac{\rho}{\epsilon_0}, \tag{47}$$

where ρ describes the local charge density, and ϵ_0 is the permittivity of the free space. It is assumed that the uniform electron beam (electrons are distributed uniformly in the beam) with radius r_H is of infinite

length and propagates coaxially to the trap with radius r_{D}. Furthermore, there is the assumption that the charge density is zero outside the electron beam and constant inside. For ρ follows

$$\rho = \frac{I}{\pi r_H^2 v_{el}}, \tag{48}$$

where I is the current and v the longitudinal velocity. Due to the cylindrical symmetry of the trap electrode, $\Phi_e(r)$ depends only on the radius.

$$\frac{1}{r}\frac{\partial}{\partial r}(r\frac{\partial}{\partial r}\Phi_e) = -\frac{\rho}{\epsilon_0}\Phi_e(r) \Rightarrow \Phi_e(r) = \begin{cases} \Phi_0(\frac{r^2}{r_H^2} + ln(\frac{r_H^2}{r_{\mathrm{D}}^2} - 1)) & r \leq r_{\mathrm{H}} \\ \Phi_0 ln(\frac{r}{r_{\mathrm{D}}}) & r > r_{\mathrm{H}} \end{cases}, \tag{49}$$

where the boundary assumption was used that $\Phi_e(r = r_{\mathrm{D}}) = 0$ is valid. For $r = r_{\mathrm{D}}$ only the drift tube potential Φ_{D} is given. Φ_0 is given by

$$\Phi_0 = \frac{I_e}{4\pi\epsilon_0 v_{\mathrm{el}}}. \tag{50}$$

Figure 7 shows the course of this radial potential for typical values. It is clear that the electron beam scales linearly with the current.

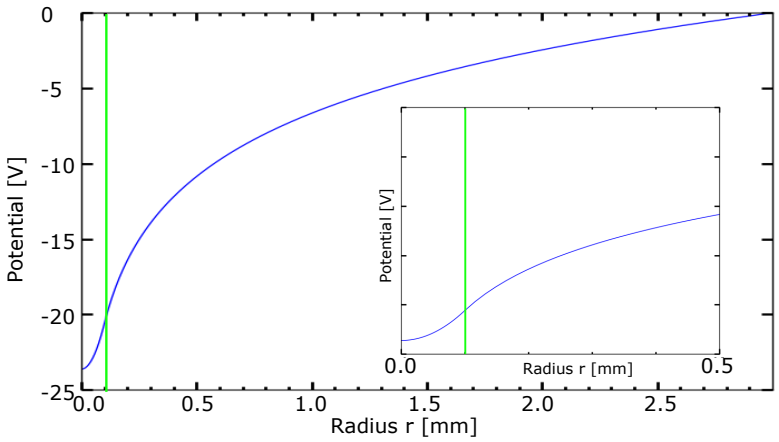

Figure 7: Potential in EBIT: typical electric space charge potential, calculated with $r_{\mathrm{D}} = 5\,\mathrm{mm}$, $I = 10\,\mathrm{mA}$, $U = 2500\,\mathrm{V}$. A beam radius of $r_{\mathrm{H}} = 100\,\mu\mathrm{m}$ (green band) was assumed. Adopted from [27].

In addition to the electric space charge potential, there is also a positive space charge potential which arises from the ions Φ_i.

Electron energy

The knowledge of the kinetic energy of the electrons E_{Beam} in the trap is of great importance since the highest charge state that can arise through the EII process depends on E_{Beam}.
In general, the electron beam energy at the location $(\vec{r})$ depends on the difference between the electric potential Φ acting there and the cathode potential Φ_{Cath}. If initially only the potentials attached to the drift tubes are considered, an axial potential landscape results. In fig.8 a typical axial potential curve caused by the applied voltages is shown. The axial trapping in the trap is clearly visible. For further information on the individual potentials, see section 3.5.2.

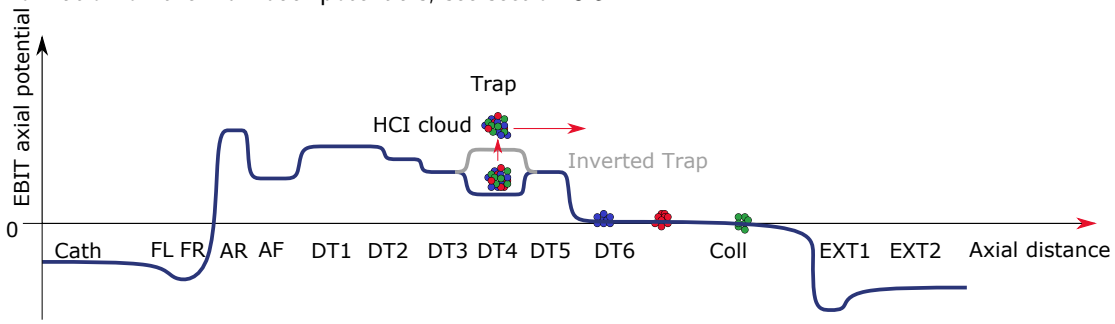

Figure 8: Potential in EBIT: b) typical axial potential curve.The axial trapping of the ions becomes clearly visible. In addition, an inverted trap is drawn that releases trapped ions. More about the individual potential in section 3.5.2.

Since only the electron beam energy in the center of the trap is of relevance, in the following the axial distance is fixed to the center of the trap. The axial electron potential in the center of the trap is that of drift tube 4 Φ_D. This potential difference to Φ_{Cath} must be corrected for the space charge potential of the ions Φ_i and electrons Φ_e. Since these depend on the radial distance, the electron beam energy has an energetic distribution. In addition, E_{Beam} must be corrected for the work function Φ_A of the electrons from the cathode.
Thus, the following applies:

$$E_{\mathrm{Beam}} = eU = e(\Phi_{\mathrm{D}} - \Phi_{\mathrm{Cath}} + \Phi_i - \Phi_e - \Phi_{\mathrm{A}}). \tag{51}$$

The difference between the nominal energy $(\Phi_{\mathrm{D}} - \Phi_{\mathrm{Cath}})$ and the actual energy depends on the depth of fall $(\Phi_{\mathrm{DT3/5}} - \Phi_{\mathrm{DT4}})$ and the current I. If the trap depth increases in the axial direction, more ions are trapped and the positive space charge potential increases. Conversely, if the current increases, the electric space charge potential Φ_e and thus the energy increases. However, the number of ions also increases. Since higher currents cause the ions to heat up, the associated Doppler broadening must be taken into account [30]. More about the energy of the electron beam can be found in [27, 35].
The energy width ΔE of the electron beam due to the radial expansion depends mainly on the self-induced potential Φ_e and can be calculated from the difference of Φ_e at the trap center $(r = 0)$ and at the Herman radius $(r = r_{\mathrm{H}})$. A smaller current reduces Φ_e and thus also ΔE. Another possibility to reduce the energy width ΔE of the electron beam is to reduce the size of the ion cloud, since the maximum radial distance of electrons that can interact with the ions is reduced. This can be improved by cooling the ion cloud. Cooling, in that case evaporative cooling, is achieved by a flat gradient in the axial direction, which allows the hot and thus fast ions to leave the trap and thus lower the temperature.

Ion movement

The movement of the ions within the trap is now considered based on [5]. The positively charged ion is affected by the Lorentz force, which arises due to the existing E and B fields:

$$m\ddot{\vec{r}} = q(\vec{E}(\vec{r}) + (\dot{\vec{r}} \times \vec{B}(\vec{r})) \tag{52}$$

If we assume that $\vec{B}$ is parallel to the z-axis (along the EBIT) ($B_x = B_y = 0$, $B_z = B$) and the E-field is rotationally symmetric to this axis ($E_x = E(r)\cos\phi, E_y = E(r)\sin\phi, E_z = 0$), then two coupled equations of motion for the radial and angular motion follow. After a transfer into a rotating reference frame with constant angular velocity Ω ($\rightarrow \dot{\phi} = \dot{\tilde{\phi}} + \Omega$) the equation of motion for the radial motion follows:

$$|\ddot{\vec{r}}| = \frac{q}{m}E(r) + r \cdot [\dot{\tilde{\phi}}^2 - \Omega^2], \tag{53}$$

where $\Omega = -\frac{q}{2m}B$ is the so-called Lamor frequency. One can easily see the above mentioned component of the radial trapping of ions by E and B field. Both capture the ions radially ($E(r)$ has a negative sign because it is generated by the negative electron beam). It is also clear that even without an electric beam, ions can only be radially trapped by $\vec{B}$ ($-r\Omega^2$). This is the so-called magnetic trap mode. If the Lamor radius $r_{\mathrm{Larmor}} = mv_\perp/qB$ induced by the magnetic field is larger than the trap, the ions cannot be stored. $v_\perp$ is the radial velocity. The higher the temperature, the more difficult the storage is. Since the EBIT used for this work has a relatively small magnetic field ($860\,\mathrm{mT}$), q/m must be very large to enable a magnetic trap mode.

3.4 Physical Processes in an EBIT

As mentioned above, the electron beam energy is relevant for the highest charge state that can be produced within the plasma in an EBIT. In addition to the non-resonant electron impact ionization, a number of other processes take place parallely, some of which can decrease or increase the charge state. For example, the charge state is increased by the resonant Auger process, whereas the also resonant DR process and the non-resonant RR process decrease the charge state by recombination. Due to the different interaction processes, there is never a certain charge state, but always a distribution, whereby two processes have to be considered: On the one hand, the effective cross-section σ_{EII} for lower charge states decreases when the beam energy is increased. On the other hand, a higher charge state also means that the recombination probability increases. Charge-conserving processes can also take place, such as inelastic collisions between ions and electrons or classical excitation and discharge processes of photons.

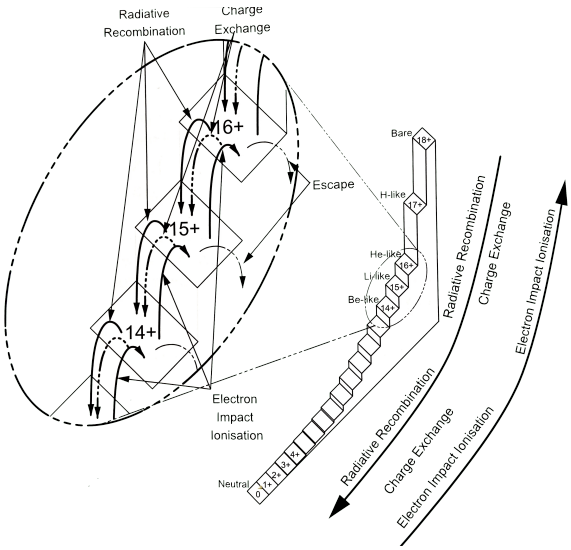

Figure 9: Overview processes which influences charge state distribution, adopted from [23]

Figure 9 shows an overview of the processes responsible for the charge state distribution.

3.5 PolarX-EBIT

In the following, the design of the PolarX EBIT is discussed, which is the EBIT used for the experiment presented in this thesis. The PolarX EBIT is one of the so-called MiniEBITs or Compact EBITs built at the Max Planck Institute for Nuclear Physics in Heidelberg and was mainly built by S. Kühn [26]. As the name suggests, it is much more compact and lighter than the original EBITs, such as the HeidelbergEBIT or FLASH-EBIT. Its dimensions are just $120\,\mathrm{cm}$ in length and $44\,\mathrm{cm}$ wide, and its total weight is less than half a ton. Unlike existing EBITs, the PolarX does not have a superconducting magnet system, but instead uses permanent magnets that can be operated at room temperature. These features give the PolarX a high degree of flexibility in its experimental use. Another main advantage of the PolarX EBIT is that it has an off-axis electron gun, which makes the central beam path freely accessible and thus enables laser spectroscopy experiments, as was done in this work.

Design

The EBIT, which can be seen in the CAD generated graphic in fig. 11, can be divided into four different functional areas: A magnetic system, which is responsible for generating the magnetic field; an electrostatic part, which is responsible for generating, guiding and collecting the electron beam; a vacuum system and an injection system. All four parts are combined into a common housing, whereby the magnetic system encloses the trap chamber with a central beam path in which the electrostatic system is located. The injection system is located at the side of the trap chamber, which itself, as well as the inlets and outlets and the injection system, is pumped out by the vacuum system. The electrostatic part consists of 3 parts: the electron gun, which is responsible for generating, regulating the electron beam; the 6 drift tubes, which are responsible for both the conduction and axial trapping of the ions and the collector, which absorbs the electron beam. A cross-section of these electrostatic elements together with the simulated electron beam path can be seen in the fig.10.

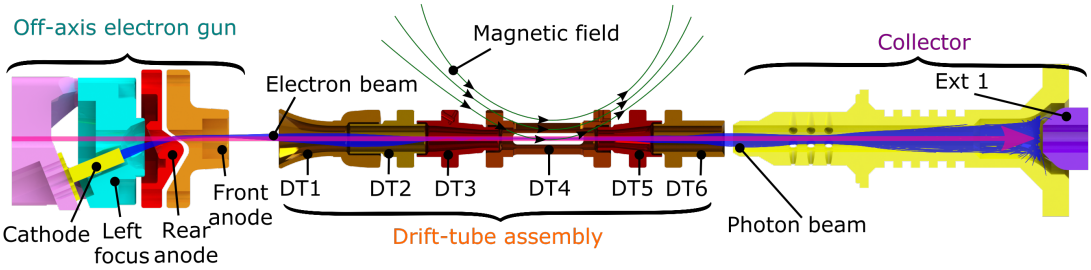

Figure 10: Electrostatic components of the PolarX EBIT in cross-sectional view consisting of off axis electron gun, drift tube assembly and collector. The calculated electron trajectory is also shown. Adopted from [35].

One EBIT has optional connections. The front part of the EBIT can be coupled to the synchrotron radiation beamline end station, the back part to an electric extraction beamline for ions (see section 3.6.2). Both options are used in this experiment. On the side, the EBIT has 2 ports (perpendicular to the axis and shifted 90° to each other), e.g. for SDD (silicon drift detectors) to measure fluorescent light. More on this in section 3.6.1. The following subchapters will explain the four components addressed in more detail.

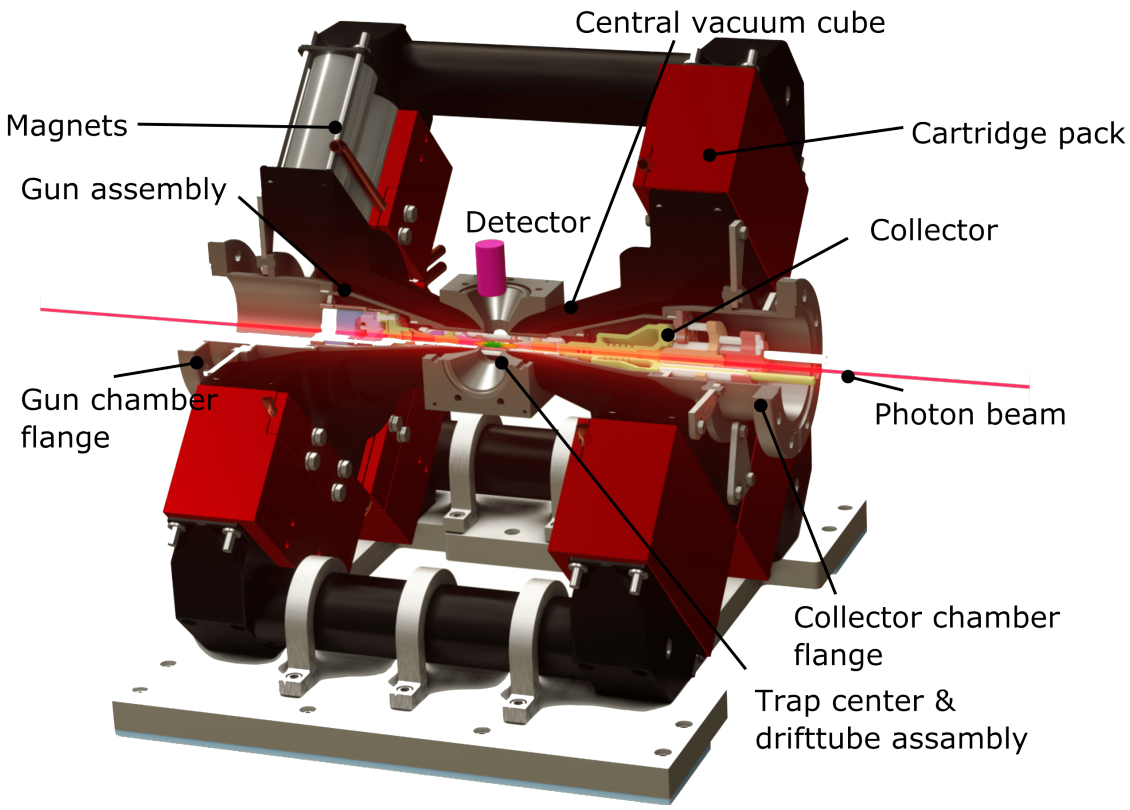

Figure 11: CAD model of the PolarX EBIT: The design allows both the electron beam generated in the off-axis cannon and an external photon beam to hit the trap center in an axial direction. The magnetic field is generated by permanent magnets in the cartridge packs. The size of the PolarX is $1200\,\mathrm{mm}$ x $440\,\mathrm{mm}$. Adopted from [26].

3.5.1 Vacuum system

The vacuum system uses a two-stage pumping system with a pre-vacuum system and individual turbo-molecular pumps (TMP). This guarantees a stable high vacuum even if one of the pumps fails. The injection area, the electric gun (in front of the trap), the trap and the collector (behind the trap) have their own pumps and can be regulated against each other with valves, so that partial ventilation is possible. In total, a pressure of between $10^{-8} - 10^{-9}\,\mathrm{mbar}$ can be achieved, depending on the range. However, it can take some time (weeks) to reach this pressure, as individual components (cathode, chamber, etc.) have to outgas first. In order to minimise the outgassing of components inside the EBIT, the internal parts have been electropolished. When assembling the EBIT, care must be taken to ensure that no hydrocarbons or other highly outgassing substances get into the EBIT, otherwise the pressure will be insufficient.

3.5.2 Electrostatic elements

a) Off-axis electron gun

An electron gun (shown in fig. 12) consists of three essential components: the cathode, anode and an electrode, which is to focus and regulate the electron beam. The cathode is to provide electrons which are then accelerated by the electric field of the anode. The cathode consists of a porous tungsten matrix at the tip in which barium oxide is dispersed [26]. During operation, the cathode must be heated to an operating temperature of about $1300\,\mathrm{K}$. In the beginning, the cathode is slowly heated in the so-called conditioning process, such that the barium oxide on the surface is reduced with other additives to a thin layer of barium. This has a very low work function ($\approx 2\,\mathrm{eV}$), which again allows an low working temperature. According to Hermann (see eq. 45), this favors a high current density. During operation, the cathode is very sensitive to oxygen and humidity, which is why the gun should always be in the ultrahigh vacuum range.

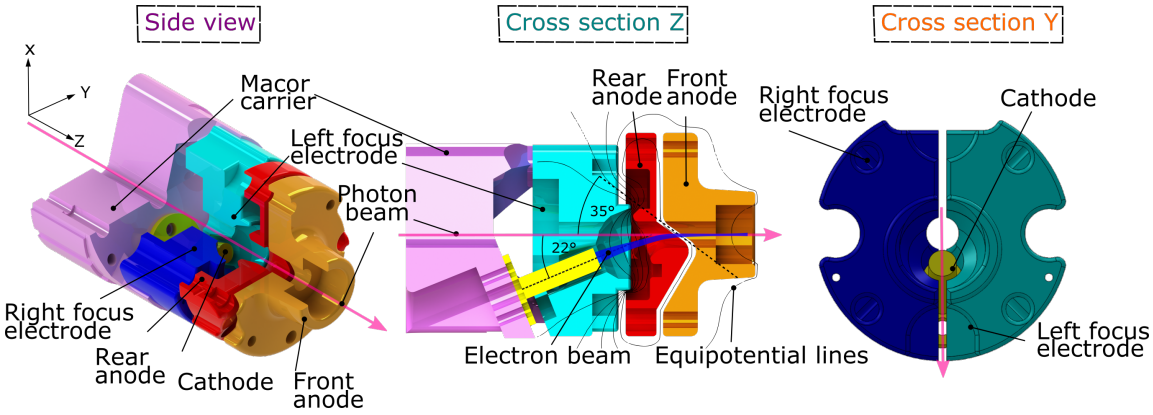

Figure 12: CAD model off-axis electron gun. The tilting of the gun (yellow) of $35°$, which allows optical access to the trap, is clearly visible. The split anode as well as the focal electrode are responsible for bending the beam. Graph adopted from [26]

The electron gun is an off-axis gun inclined at an angle of $22°$ to the main axis. The gun can be positioned in place by means of an XYZ manipulator, which is especially important for the alignment in the magnetic field. This design allows only smaller currents than an on-axis gun, as the electron beam has to be bent by additional electrodes, but it opens the optical access to the trap ($4\,\mathrm{mm}$ aperture for a $\approx 1\,\mathrm{mm}$ photon beam is enough). For bending of the electron beam, the anode is divided into a front and rear anode, with the edges of the two parts tilted at $35°$ to the horizontal. The rear anode is used for acceleration inside the gun, whereas the front anode is used for bending. In practice, the rear anode has approximately twice the (positive) voltage as the front anode. Since the electron beam is no longer emitted parallelly to the magnetic field, the resulting Lorenz force deflects the beam sideways. This can be compensated for with the help of a split focus electrode (left/right). The lower the cathode's voltage, the higher the voltage difference between FR and FL. In most cases, a voltage difference of less than $10\,\mathrm{V}$ is sufficient. The optimal value depends only slightly on the acceleration voltage [35]. Another main function of the focal electrode is to regulate the maximum emitted current. The focus electrodes are usually set to a more negative potential than the cathode and thus represent a hurdle for the electrodes - set as the cathode (see fig. 8). The emitted current therefore decreases. The cathode is

always negatively charged, so that the electrons always have a potential and thus a velocity to ground. The smaller the potential compared to ground, the more difficult it is to achieve a good transmission. To heat the cathode at the same time, the heating current supply must also be set to the negative voltage of the cathode. High transmission ($> 99\%$) is possible at high currents with a strongly negatively charged cathode ($-2000\,\mathrm{V}$) and thus high electron beam energy.

b) Drifttubes

The total of 6 drift tubes (cylindrical electrodes) have the task of both directing the beam inside the trap and catching the ions axially. In contrast to the electrodes near the cathode, the drift tubes have only a small influence on the strength of the emission current due to their distance, but they have a considerable influence on the transmission. Altogether, the drift tubes are $10\,\mathrm{cm}$ long and have an inner diameter of $4 - 6\,\mathrm{mm}$ ($r_{\mathrm{DT4}} = 5\,\mathrm{mm}$). DT1 and DT2 are directed towards the electron gun with a trumpet-like entrance and are responsible for directing the electron beam, DT3, DT4 and DT5 are used for axial trapping of the ions, whereby DT3 and DT5 always have the same voltage in this EBIT (a power supply). The difference to DT4 represents the drop depth and directly influences the number and temperature of the ions ("evaporative colling"). A greater drop depth also allows heavier ions to be trapped. With the help of a HV switch transistor (BEHLKE), DT4 can be switched within nanoseconds between the "normal" drittube potential of DT4 and an inverted trap potential U_{Kick}. The switch is triggered by a TTL pulse from a function generator that determines the kick frequency f_{Kick} (see chapter 3.7). This allows the trap to be emptied abruptly and the ions extracted with the extraction beamline (see section 3.6.2). If the trap is emptied too quickly, the possible charge states may not have formed yet. If the trap is discharged too slowly, the trap may be filled with unwanted ions (if light ions are to be observed). The center of the trap has four optical access ports perpendicular to the axis with a length of $16\,\mathrm{mm}$ and a width of $2.5\,\mathrm{mm}$. The cut out holes are covered with a stainless steel mesh to prevent fringe effects. A picture of the drift tubes can be seen in fig. 13a.

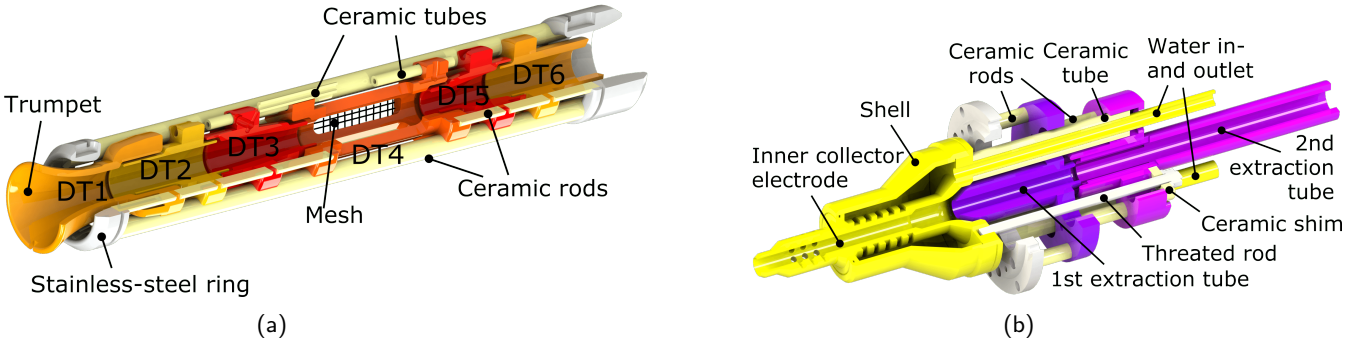

Figure 13: a) Cross-sectional view of the drift tube assembly. The trumpet-shaped inlet is oriented towards the gun. The incision with the mesh enables the detection of fluorescence photons. b) Cross-sectional view of the collector, the water-cooled main electrode and the two extraction electrodes for slowing down the electrons can be seen. Both images are from [35].

c) Collektor

The collector captures the electron beam and measures how much current flows through the EBIT compared to the emission current from the cathode. The collector consists of three electrodes - the main collector electrode, which is at ground to slow down the electrons, and two extraction electrodes, each at a much more negative potential than the cathode to prevent the electron beam from damaging rear components. At the same time, the extraction electrodes can be used as ion optics (see also section 3.6.2). In addition to deceleration, the attenuated B-field there also favors electron extraction as the beam spreads out and hits the collector wall. The collector electrode, which is grounded ($U_{\mathrm{coll}} = 0$), heats up due to the energy carried by the electrodes with the heating cable P:

$$P = (U_{\mathrm{cath}} - U_{\mathrm{coll}}) \cdot I_{\mathrm{coll}} = U_{\mathrm{cath}} \cdot T \cdot I_{\mathrm{cath}} = U_{\mathrm{cath}} \cdot \frac{U_R}{100\Omega}, \tag{54}$$

where $T = I_{\mathrm{col}}/I_{\mathrm{cath}}$ is the transmission, i.e., the ratio of the collector current to the emission current. The collector current is measured by means of a $100\,\Omega$ resistor connected to the collector (see also chapter 3.7). In order to dissipate the heating power, a copper housing is built around the electrode, which is made of copper, through which a water cooling system passes. Otherwise, the high vacuum can no longer be guaranteed. A cross section of the collector is shown in fig. 13b.

3.5.3 Magnetic system

The magnet system consists of a set of 72 NdFeB permanent magnets with a diameter of $45\,\mathrm{mm}$ and a height of $30\,\mathrm{mm}$. Nine of these magnets are arranged in a cartridge in three columns of three stacked magnets. Four such cassettes - each fixed between magnetisable steel - are arranged in an X-shape at the beginning and end of the EBIT, perpendicular to the beam axis. Inwardly, the cartridges are mounted on a soft iron piece which tapers towards the center of the trap. In addition, the cartridges are connected axially at the end by soft iron bars in order to increase the magnetic flux. In fig. 14, a simulated magnetic flux of the EBIT is shown on the left and the axial course of the magnetic flux density along the beam axis is shown in the right plot. For an optimal electron compression according to eq. 45, the cathode should be at the zero crossing of the B-field ($-95.5\,\mathrm{mm}$) in order to achieve the highest possible current density. In the radial direction, the magnetic field is almost perfectly rotationally symmetrical. With the described magnet system, a flux density of more than $860\,\mathrm{mT}$ can be achieved.

3.5.4 Injection system

If gases not naturally existing in the EBIT have to be measured in the experiment, the gases have to be supplied from the outside. The desired element may already be gaseous or have a high vapour pressure so that it evaporates in the UHV. Naturally occurring elements include hydrogen, oxygen, nitrogen and carbon, the last of which is evaporated from the vacuum chamber. The injection system consists of two sections connected by a fine dosing valve, both of which are connected to a turbomolecular pump. The front section is connected to the element chamber, while the rear section is connected to the central chamber of the EBIT via a $5\,\mathrm{mm}$ orifice. The front part is flooded with the element to be investigated and placed in a high vacuum ($< 10^{-3}\,\mathrm{mbar}$). Via the fine dosing valve, the rear part can now be filled with the gas that has now been generated at the latest. During this process, the pressure in the UHV is maintained. To prevent any inaccuracies when manually setting the injection pressure in the rear section, this is provided with an additional valve to the EBIT, which is closed during setting [26, 27].

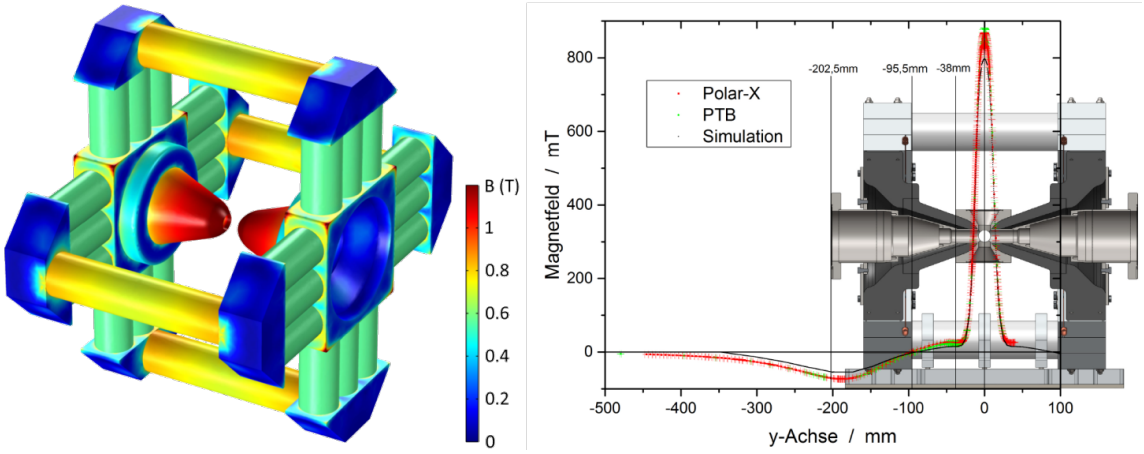

Figure 14: Left: Magnetic flux on the surface of the EBIT simulated with COMSOL. The 72 permenant magents NdFeB (green) generate the magnetic field, which is guided into the trap interior by magnetic steel and softness (blue/yellow shades). Figure adopted from [35], Right: Axial magnetic field flux profile. For optimal electron compression, the cathode should be in the zero crossing of the B-field ($-95.5\,\mathrm{mm}$). Figure adopted from [27].

3.6 Detection systems

The EBIT is able to detect fluorescence photons as well as to read out the charge state distribution of the HCI within the trap. Both information are very important in the evaluation, because e.g., the charge state distribution can give information about a photoionization that has taken place, whereas the fluorescence photons give information about the charge conserving radiative decay channel of a transition. More on this in the analysis. Both detection systems are discussed in the following two subchapters.

3.6.1 Photon detection

SDD For photon detection, a silicon drift detector is used, which can be attached to one of the four openings on the trap. Figure 15 shows the SDD Detector schematically. The cylindrical SDD consists of a moderately n-doped silica substrate, which is covered on both sides with a highly doped p-doped substrate. In contrast to the subset, the upper surface is not homogeneously covered but is occupied by equidistant rings. The underside acts as a radiation entrance window. A relatively small anode is located near the center. Despite the small size of the anode, it is possible to fully depleted the SDD by applying a voltage in the reverse direction (anode is positively charged with respect to the bulk) between the front and rear sides, similar to a reverse-biased diode. In addition, by applying a negative voltage with respect to the anode to the outermost and innermost rings, a horizontal electric field is generated so that there is no field-free area in the charged SDD. The outer ring electrodes (U_{OR}) have compared to the inner one a more negative potential (U_{IR}).
When a photon falls on the SDD, it lifts a valence electron into the conduction band if the energy is large enough. The primary electron can generate further pairs of electron-holes in a cascade-like manner, whereby the number of electrons generated is proportional to the energy. The pairs are separated by the electric field of the reverse-biased diode and by the horizontal electric field of the ring electrodes, with the electrons flowing to the central anode. The electrons flow to the n-doped anode, the holes to

the p-doped substrate. The anode is connected to an integrated JFET, which acts as a preamplifier to convert each current pulse into a voltage pulse. The electrons generated by the incident photon charge the capacitance in addition to leakage currents. The voltage jump at the preamplifier thus corresponds to the energy of the photon. If a certain threshold voltage is reached, the capacitance is cleared via an offset pulse, which results in a sawtooth voltage [26]. The small capacity has the advantage that the SDD has a very short rise time of the output signal, which makes it possible to get high count rates [29]. This voltage signal of one photon is fed into a spectroscopy shaping amplifier (Ortec 672), which converts the step-shaped signal from the pre-amplifier into a Gaussian signal, where the area under the Gaussian corresponds to the height of the step function. This signal is now digitised in an analog-to-digital converter (ADC). More about that topic in [12, 26].

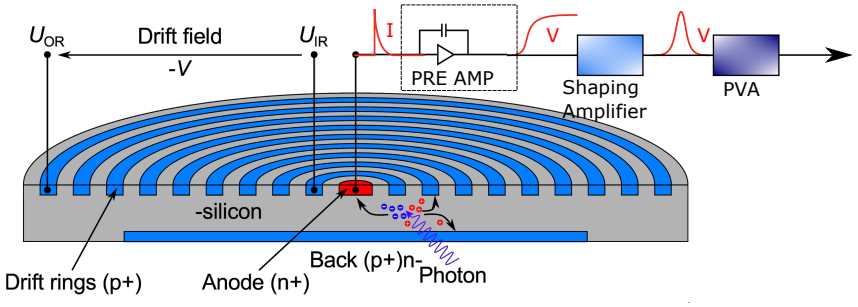

Figure 15: SDD: Each photon with sufficient energy generates electron-hole pairs which are separated by the electric field of the concentrically arranged electrodes but also by the space charge zone of the substrate. The electrons are collected on the anode.The current pulse generated by a single photon in the SDD detector, whose pulse height is proportional to the energy, is converted into a voltage pulse in an internal amplifier (JFET). A shaping amplifier converts this signal into a Gaussian signal whose area corresponds to the pulse height. Finally, the signal is digitised in an ADC (more on this in chapter 3.7). Graphic taken and modified from [12, 51].

Resolution The resolution of the SDD detector is limited by the count rate. The number of mean generated electron-hole pairs $\bar{N}$ for an incoming photon with energy E is $\bar{N} = E/w$, where w=3.62 eV is the experimentally determined generation energy for an electron-hole pair in a solid state silicon wafer at room temperature. $\bar{N}$ is subject to fluctuations, where the variance is given by $\sigma^2 = F \cdot \bar{N}$. $F = 1$ means that the counting behaviour follows the Poissons statistic $F = 0$ that no fluctuation is present. Silcium has an F of approx. 0.1 For the resolution thus applies:

$$\frac{\Delta\bar{N}}{\bar{N}} = \frac{\sqrt{F \cdot \bar{N}}}{\bar{N}} = \frac{\Delta E}{E} \rightarrow \Delta E = \sqrt{w \cdot F \cdot E} \approx 0.6 \cdot \sqrt{E} \tag{55}$$

The lines measured in this experiment, e.g. K_α of He-like oxygen at $574\,\mathrm{eV}$ means a FWHM width of $FWHM = 2\sqrt{2ln(2)} \cdot 0.6 \cdot \sqrt{E} \approx 33.8\,\mathrm{eV}$, which is still slightly below the theoretically possible resolution of $60\,\mathrm{eV}$. Since the SDD can measure not only the interesting X-ray radiation but also interfering radiation (black body radiation, etc.), a filter was pre-installed to block visible and ultraviolet light. A $500\,\mathrm{nm}$ thick aluminium filter was used [26].

3.6.2 HCI detection

Time of Flight In order to be able not only to measure fluorescence photons but also to determine the charge state distribution, an additional HCI detection system must be used. For this purpose, a time-of-flight spectrometer can be used, which takes advantage of the mass- and charge-dependent time required for the ions to travel a distance L between the ion trap and the detector. The ions are accelerated out of the trap via an extraction potential ($U = |U_{\text{kick}}| + |U_{\text{ext}}|$) and directed via a beamline to an multichannel plate (MCP) detector, which registers signals at different times depending on the TOF of the ions.
In the simplified model, it is assumed that all ions are at the same location in the trap at time t=0 and receive energy $E = qU$ through a voltage U. Only after the acceleration is finished, the timing starts and the potential would not change anymore, the ions hit the detector and emit secondary electrons. Figure 16 shows the basic principle of a time-of-flight spectrometer, then the time-of-flight Δt to the detector is valid:

$$\Delta t = \frac{L}{v} = L\sqrt{\frac{m}{2qU}} \rightarrow \frac{q}{m} = \frac{L^2}{2\Delta t U} \tag{56}$$

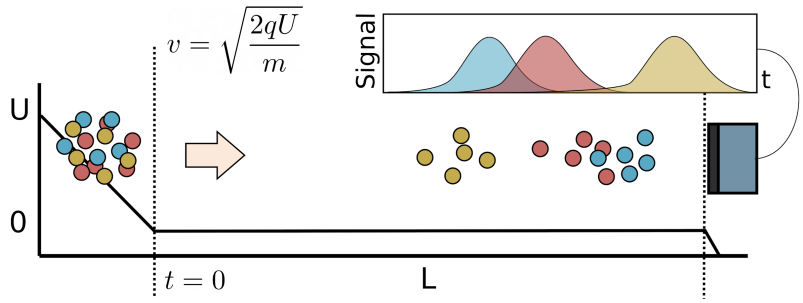

Figure 16: Operating principle Time-of-Flight Spectrometer, which can resolve between different q/m. Adopted from [51].

However, there are a few things that need to be taken into account which will cause the detector signal to smear in time. First, the acceleration potential is not the same for all ions because they are not all in the same location. Also, the kick signal is used as the temporal starting point. That is, the ions must first accelerate, which would extend the eq. 56 in the form of an additional acceleration time term. In addition, the potential generated by the ion optics accelerates and decelerates the ion differently depending on q/m, and during flight there are space charge effects due to repulsion that can also lead to time smearing. However, all these effects are relatively small due to the strong accelerated E-fields and can therefore be neglected.

HCI selection electronics The electronic analysis circuit is shown in fig. 17.
After the ions have been kicked as described in section 3.5.2, they are accelerated by the extraction potential ($U = |U_{kick}| + |U_{ext}|$) and hit an MCP detector. Since the time-of-flight spectrometer cannot be set up axially to the end of the EBIT, but perpendicular to it at a 90-degree angle, an ion optics consisting of several Sikler lenses (upper-ST, left-SL, right-SR, lower-SB) and benders (outer-OB, inner-IB) must deflect the ions. The flight of the ions is influenced by these potentials and must therefore be optimised.

An MCP is a secondary electron multiplier. When a charged particle hits the inside of the channels, it releases electrons from the detector. These are accelerated in the channels due to a applied voltage and generate a cascade of secondary electrons when they hit the inside.
The joined MCP has a front and rear terminal that is supplied with your HV input voltage. In order for the generated electron pulse to flow to an anode, the anode must be electrically more positive. A voltage divider (R1 and R2) is used to ensure that a more negative voltage is applied to the MCP back than to the grounded anode. An additional capacitor between the HV input and the ground prevents the coupling of an alternating voltage. First, consider the uncharged capacitor. The charge Q_{MCP} (order of magnitude $10^{7}\,\mathrm{C}$) generated in the MCP by the HCI pulse hits the anode within the pulse duration dt (order of magnitude $10^{-10}\,\mathrm{s}$) and charges the capacitor C2 according to its capacity $dU = \frac{dQ}{C}$. This leads to a current pulse of $I_{charge} = C\frac{dU}{dt} = \frac{dQ}{dt}$. When the charge pulse of the MCP is finished, the capacitor discharges via R3 (RC element with $\tau = RC$). Since this is a discharge process, the current $I_{\mathrm{discharge}}$ is negative and approaches the zero line exponentially:

$$I_{\mathrm{discharge}}(t) = -I_{max}e^{-t/\tau} = -\frac{U}{R}e^{-t/\tau} \tag{57}$$

where $U = \frac{Q}{C}$ is the voltage close to charging at the capacitor. Only now is the signal of the HCI pulse is completed. The current pulse is now converted by a pre-amplifier into a voltage pulse, which is displayed on the oscilloscope. In order to keep the amplitude of the discharge current as small as possible, the resistance R and capacity C must be as large as possible. However, this also increases the half-life of the discharge process ($T_{1/2} = \tau \ln 2 = RC \ln 2$). Thus, a compromise must be found between the signal strength of $I_{\mathrm{discharge}}$ and the duration of the discharge process. If one observes ions with very small ToF differences, RC must be chosen small. Furthermore, it should be noted that there is another electrical artifact besides the discharge process. This is discussed in more detail in section 5.4.3.

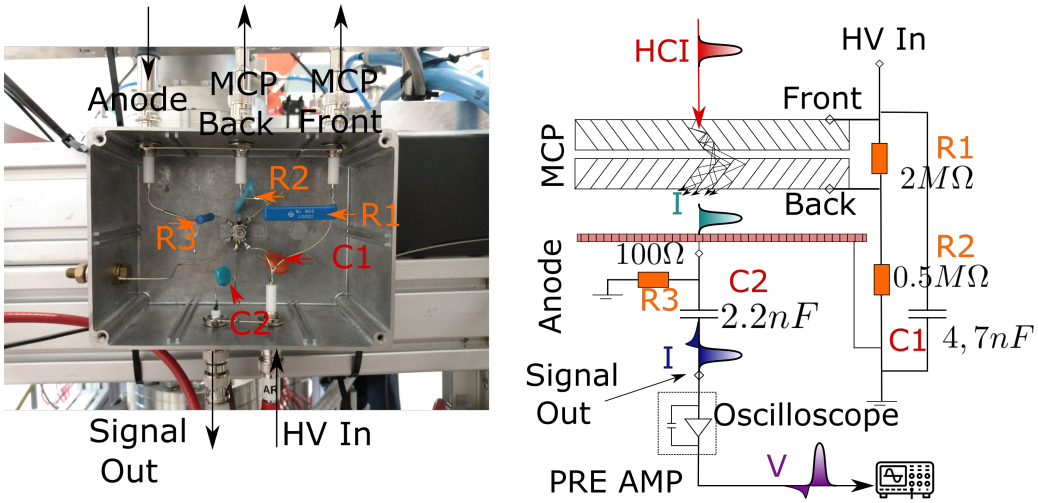

Figure 17: Electrical circuit of the HCI detection/MCP (left picture, right: circuit diagram): The voltage divider ($R_1 + R_2$) causes a negative MCP back potential with respect to the anode, whereby the generated electrical pulse is led to the anode. The discharged charge of the MCP pules generates a charging current at the capacitor. After the pulse, the capacitor discharges via resistor R_3. The related current signal is then converted into a voltage signal in a pre-amplifier and sent to the oscilloscope.

3.7 Control System Electronics

The control system and data acquisition system are divided into three independent areas: The EBIT control system, HCI detection and photon detection. Figure 18 gives an overview of these three systems.

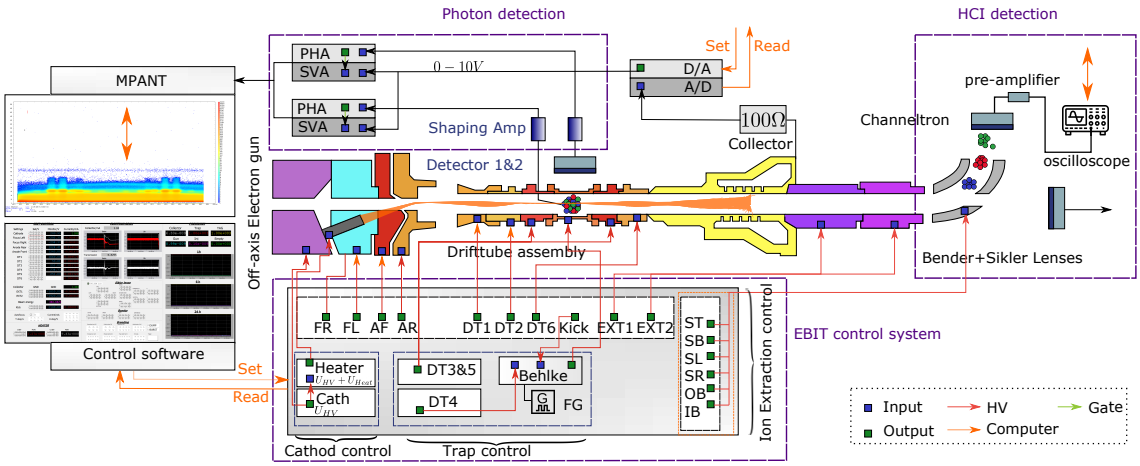

Figure 18: Schematic representation of the control and measurement system of a PolarX EBIT: It consists of control software, which controls and reads all potentials and two measurement systems (HCI and photon detection). The HCI signal is read in digitally directly via the oscilloscope, while the photon detection is read in via separate software and hardware (MPA4/MPANT).

EBIT control system The EBIT control system sets and reads all electrode potentials via central software using EPICS servers. It enables the control of cathodes, traps and ion extraction. Except for DT3 to DT5 and the cathode, all potentials are controlled by a high-voltage NHS unit from ISEG, which can deliver between $100\,\mathrm{V}$ and $6\,\mathrm{kV}$. The cathode control consists of a HV power supply which supplies the cathode holder as well as the heater power supply with the necessary high voltage. In contrast to the HV power supply, this can deliver high heating currents (about $1.25\,\mathrm{A}$ at $10\,\mathrm{V}$). Only in this way can the cathode be heated and at the same time be applied to the negative high voltage required for EBIT operation. The trap is also operated with 2 extra power supplies for DT4 and $3\ \&\ 5$. With the help of a fast high voltage switch/transistor (Behlke), DT4 can be set to a kick potential U_{Kick} as described in section 3.5.2 b) and invert the trap. The Behlke is triggered by a TTL pulse from a controllable function generator (FG), which determines both the breeding time and the kick frequency. If DT$3\ \&\ 5$ are also connected to a Behlke, the trap can be shifted energetically very quickly. This was not necessary in the experiment. In addition, the software has a representation of the four measured pressures (gun, injection, trap and collector) and calculates the transmission measured via the measured voltage at the $100\,\Omega$ collector resistor.

Photon/HCI detection The HCI detection is carried out as described in section 3.6.2. The only difference is that instead of an MCP, a channeltron was used, which performs the same function as an MCP (secondary electron multiplier) but has a slightly different structure. However, like the MCP, it needs a front and back voltage to accelerate the secondary electrons to the anode. The amplified data (several sets of oscilloscope data) are stored in a log file (.json) together with other important parameters

such as pressure, EBIT potentials and additional information, e.g. photon energies of the synchrotron radiation. The photon detection system consists of 2 SDD detectors with two ADC each. The ADC used in the experiment (7072 Dual Timing $500\,\mathrm{ns}$ ADC) has 8192 channels and are operated in two modes [51]: In pulse height analysis mode (PHA), the area of an incoming pulse is converted to its height and assigned to a channel. With the help of a threshold and lower and upper discriminators noise can be minimised, since only certain pulses are processed. In the analog scan analysis (SVA), an applied voltage between 0 and $10\,\mathrm{V}$ is digitalised as soon as a TTL pulse triggers the ADC. This is done via the so-called gate.

Each SDD detector is connected to a shaping amplifier, which is connected to an ADC operated in PHA mode as shown in section3.6.1. In addition, an SVA operated ADC is used to assign the determined photon energy to a second quantity (e.g. electron beam energy or photon beam energy). The PVA ADC is used to gate the SVA ADC, which is supplied with a voltage between $0\,\mathrm{eV}$ and $10\,\mathrm{eV}$ by the control system. This makes it possible to assign a voltage. The system with which all ADCs are read is the MPA4 system (Multiparameter Multichannel Analyzer) from ComTec with the MPANT software. It can analyse the data from 8 different ADC with a resolution of 16bit over a voltage range of $0 - 10\,\mathrm{V}$. If the ADC are displayed one-dimensionally against time (ADC x t) or against each other (ADC x ADC), one obtains coincidence spectra. The data for each event for each ADC are stored with a time stamp in a list file.

4 Synchrotron

4.1 Basics

This chapter explains the general principle of synchronous radiation. One source of this radiation is the synchrotron Elettra in Trieste, Italy, with its associated GasPhase photoemission beamline. This is the second part of this chapter.

4.1.1 Principle

A synchrotron makes use of the fact that accelerated charge emits electromagnetic radiation due to energy conservation. If electrons are kept on a curved path by a magnetic field, as happens in a synchrotron, i.e. accelerated, they emit electromagnetic radiation. The instantaneous radiation power P of an electron with energy E and charge e moving with non-relativistic velocity and acceleration $\frac{dp}{dt} = \dot{v}m$ can be calculated using the Larmor formula (CGS units) [8]:

$$P = \frac{2e^2\dot{v}^2}{3c^3} \tag{58}$$

If the electrons move at relativistic velocities (such as in a synchrotron with GeV), eq. 59 must be converted to relativistic form

$$P_{\mathrm{rel}} = \frac{2e^2}{3m^2c^3}\Big[\left(\frac{d(\gamma\mathbf{p})}{d\tau}\right)^2 - \frac{1}{c^2}\left(\frac{dE}{d\tau}\right)^2\Big], \tag{59}$$

using the four-momentum $\mathbf{p}$. τ describes the proper time and m_0c^2 the rest energy of the electron. The relation $d\tau = (1/\gamma)dt$ and $\gamma = \sqrt{1-(v/c)^2} = \frac{m_0c^2}{E}$ [8] holds. According to [8], the rate of change of energy per time for an electron moving in a circular path is much smaller than the change of momentum. Therefore, in eq. 59, the second term can be neglected:

$$P \simeq \frac{2e^2c}{2R^2}\left(\frac{E}{m_0c^2}\right)^4 \tag{60}$$

For the energy that is lost per revolution (circumference $C = 2\pi R$), i.e. the energy that must be recompensed if one wants to maintain the synchrotron radiation, the following applies:

$$\Delta E(keV/rev) = P\frac{2\pi R}{c} \simeq \frac{88.5E^4[GeV]}{R[m]} \tag{61}$$

4.1.2 Angular distribution

If one considers electrons with non-relativistic velocities ($\beta = v/c \gg 1$) (or observes the electron in his center of mass system), the power distribution corresponds to the radiation of a hertzian dipole, whereby the maximum intensity is emitted perpendicular to the acceleration and does not depend on the electron velocity [47]. However, if the electron moves with $v \approx c \rightarrow \beta \approx 1$, the angular distribution (as a consequence of a Lorentz transformation from the center-of-mass system to the laboratory system) is a narrow cone, with the orientation tangential to the electron orbit and in the direction of motion. The natural vertical half-opening angle Ψ is given by [47]

$$\Psi \approx \frac{mc^2}{E} = 1/\gamma, \tag{62}$$

where $\gamma = 1957E(\mathrm{GeV})$ is a simplified and practical unit. An electron energy of $E = 2.4\,\mathrm{GeV}$ corresponds to a half-opening angle of $\Psi \approx 0.014°$. This radiation characteristic enables high intensities even at large distances from the storage ring. If a horizontal slit with width w and distance D to the electron orbit is installed, only light that fulfills the condition $\Delta\theta = w/D$ is incoherently collected over an orbital angle $\Delta\theta$. This angle is significantly larger than the natural half-opening angle Ψ. Thus, the natural opening is maintained only in the vertical direction. Figure 19 gives an overview of the differences of the described radiation characteristics and angular distributions.

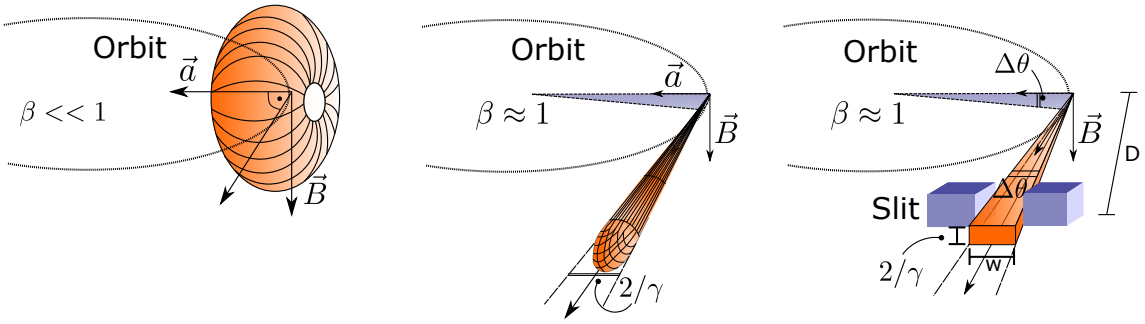

Figure 19: Characteristic radiation behaviour of an electron moving in an orbit due to an applied B-field. The dipole-like radiation for slow electrons develops into a pointed crown-like radiation with a natural half-opening angle Ψ for relativistic velocities. This angular distribution can be further manipulated by an exit slit so that the outgoing light has a horizontal angular distribution of θ and a vertical one of $\Psi = 2/\gamma$. Graph based on [47].

4.1.3 Insertion devices

Each synchrotron has a ring-shaped structure in which the electrons move with an energy that can be set by the synchrotron parameters. In it, there are both straight-line acceleration paths and magnetic ring accelerators (bending magnets), which keep the charged particles in the ring. Thus, a synchrotron is also a storage ring. Only in the first generation of synchrotrons were these magnets also responsible for the actual synchrotron radiation. The second and third generations use wigglers or undulators - so-called "insertion devices" - as synchrotron radiation sources.
An insertion device is a periodically alternating magnet structure that is built into the linear part of the synchrotron ring. In this magnetic structure with a length of L, electrons are moved perpendicular to the direction of motion on N sinusoidal paths with wavelength λ_u, thus emitting synchrotron radiation. λ_u describes the distance between the alternating magnets and is a constant parameter of the insertion device. The difference between undulator and wiggler is the different ratio between the periodic deflection angle α and the natural vertical half-opening angle γ^{-1} of the synchrotron radiation: $K = \alpha\gamma$. For an electron moving in a sinusoidal orbit, K is given by [47] :

$$K = \frac{e}{2\pi mc}\lambda_\mathrm{u}B = 0.934\lambda_\mathrm{u}[cm]B[T] \tag{63}$$

The amplitudes of the trajectories in a wiggler are stronger compared to the undulator (due to the higher B-field). The wiggler has a much bigger α than the natural vertical half-opening angle γ^{-1}, which results in $K \gg 1$. Therefore the emitted radiation of the individual electron bunches cannot interfere. In contrast to the wiggler, the electron bunches in an undulator can now interfere ($K < 1$).

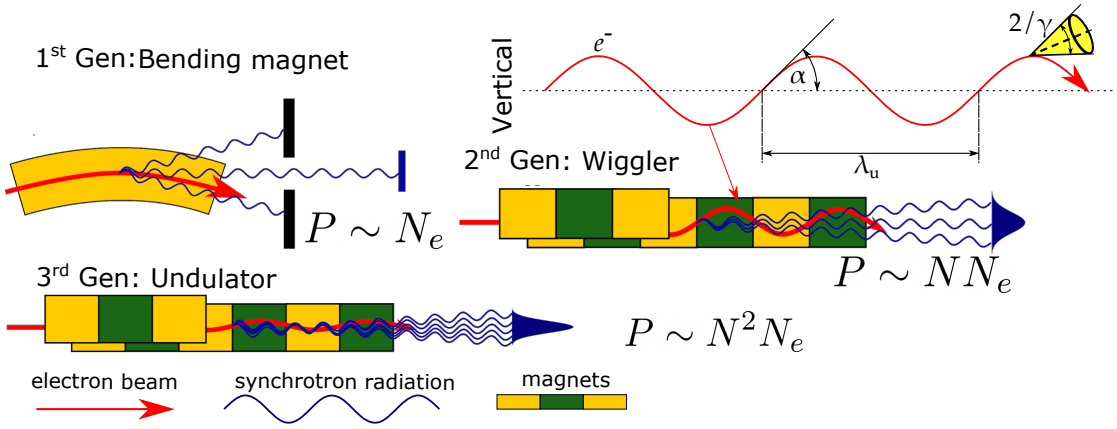

Figure 20: Differences in synchrotron radiation of Bender magnets (1^{st} gen), wigglers (2^{nd} gen) and undulators (3^{rd} gen). For the wiggler, the vertical view is also shown, which represents the sinusoidal course of the electron trajectory with the natural vertical angle γ and the deflection angle α. Adopted from [26, 47].

If one observes the radiation at an angle θ with respect to the main axis of the undulator, then λ applies to the wavelength at which interference occurs [47]:

$$\lambda = \frac{\lambda_u}{2\gamma^2}(1 + \frac{K^2}{2} + \gamma^2\theta^2) \tag{64}$$

Higher harmonics of shorter wavelengths can also interfere constructively ($\lambda_n = \lambda/n$). The intensities of both insertion devices and of the bender depend on the number of electors from N_e. For the insertion devices, the number of periods in the magnetic field also plays a role. The radiation power of the wiggler is only proportional to NN_e because of the non-existing interference, whereas the undulator radiation power is proportional to N^2N_e. In fig. 20, an overview of the three generations of synchrotron is shown. In addition to the possibility of interfering, the undulator offers the advantage that the radiation wavelength can be changed with K according to eq. 64. In turn, K can be changed with the B-field. In the case of insertion devices with permanent magnets, the B-field can be changed by the distance between them. Depending on how the electrons are deflected in the bender, wiggler or undulator, linear, circular or elliptical polarised light can be produced. In the most common case, the insertion devices produce linearly polarised light.

Monochromator

Integral components of a monochromator are the entrance and exit slits and the grating. If light hits the grating, interference is only possible for a wavelength λ (or a multiple thereof) under a certain angle of incidence α and angle of exit β: $m\lambda = d(\sin(\alpha) \pm \sin(\beta))$. Thus the beam is fanned out. With the help of an output slit, the energy can be selected. Figure 21 shows the schematic principle of a spherical grating monochchrator. The larger the slit, the larger the photon flux, but the smaller the energetic resolution $E/\Delta E$. The choice of slit width is therefore a compromise between spectral resolution $E/\Delta E$ (small slit) and the required photon flux (larger slit). The entrance slit has the task of defining the focal

point of the source and that the light waves from the source are as parallel as possible. Parallel light beams reduce scattered light. The additional plane mirror makes it possible to fix the position of the exit and entrance slits. By changing the two mirror angles, any energy can be adjusted.

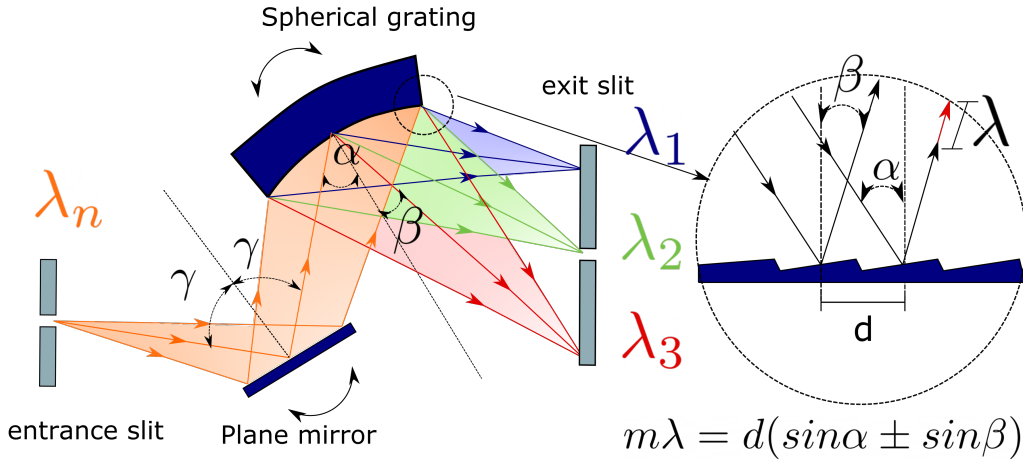

Figure 21: Schematic principle of the monochromator. The incoming polychromatic light is divided into its wavelengths with the aid of a plane mirror and a spherical grating and separated via the output slit. Both the input and output slits can remain fixed in place. The grating (interference distance d) allows for a certain wavelength λ and angle of incidence α only constructive interference for a certain emission angle β.

4.1.4 Elettra

This experiment has been conducted at the synchrotron radiation facility ELETTRA in Trieste, Italy. It is a third generation synchrotron and has been in operation since October 1993. Elettra can deliver photons in the energy range from a few eV to several keV, with a spectral brightness of $10^{19}\,\mathrm{photons/s/mm^2/0.1\ \%}$. The electrons are not first accelerated in the ring, but via a pre-acceleration system. The pre-accelerator, consisting of a long linear accelerator LINAC and a booster, accelerates the electrons to an operating energy of 2 or $2.4\,\mathrm{GeV}$. Until 2007, this system consisted of only one LINAC, which meant that the electrons still had to be upscaled to the end energy in the ring. In the $12\,\mathrm{m}$ long LINAC, the electrons are accelerated to $100\,\mathrm{MeV}$ at a pulse rate of $3\,\mathrm{Hz}$ before being accelerated to their final energy of several GeV in the booster ring with a circumference $C = 118\,\mathrm{m}$. The booster can accelerate from $100\,\mathrm{MeV}$ to $2.5\,\mathrm{GeV}$ with a maximum current of $6\,\mathrm{mA}$ at a repetition rate of $3\,\mathrm{Hz}$. The required electron energy (between $100\,\mathrm{MeV}$ and $2.5\,\mathrm{GeV}$) can be selected by choosing the correct extraction time, whereby the electrons are also transferred into the main ring via the injector at $3\,\mathrm{Hz}$ until the desired ring current is reached. High vacuum is used in both the LINAC and the booster to minimise loss interactions.
To ensure that the energy of the electrons does not decrease constantly due to the radiation (the synchrotron radiation of the Bender already requires $90\,\mathrm{kW}$), the loss energy is compensated by high-frequency cavities with alternating electric fields within the line acceleration range. This RF alternating field can both accelerate and decelerate - so only a small part of the electrons - namely those with the right timing, can be compensated again. According to [47] only 5-10% of the RF period is able to restore the electron energy. Thus, radiation also occurs at certain intervals. There are two limiting cases of

electron bunches in the storage ring. Either there is only one bunch moving in the ring - the period is therefore the round-trip time ($T_0 = C/v_{\mathrm{el}}$ - orders of microseconds) or there are bunches moving with a minimum period from the RF cavity ($\nu_{\mathrm{RF}} = 500\,\mathrm{MHz}, T_{\mathrm{RF}} \approx 2\,\mathrm{ns}$). This can be set freely by the

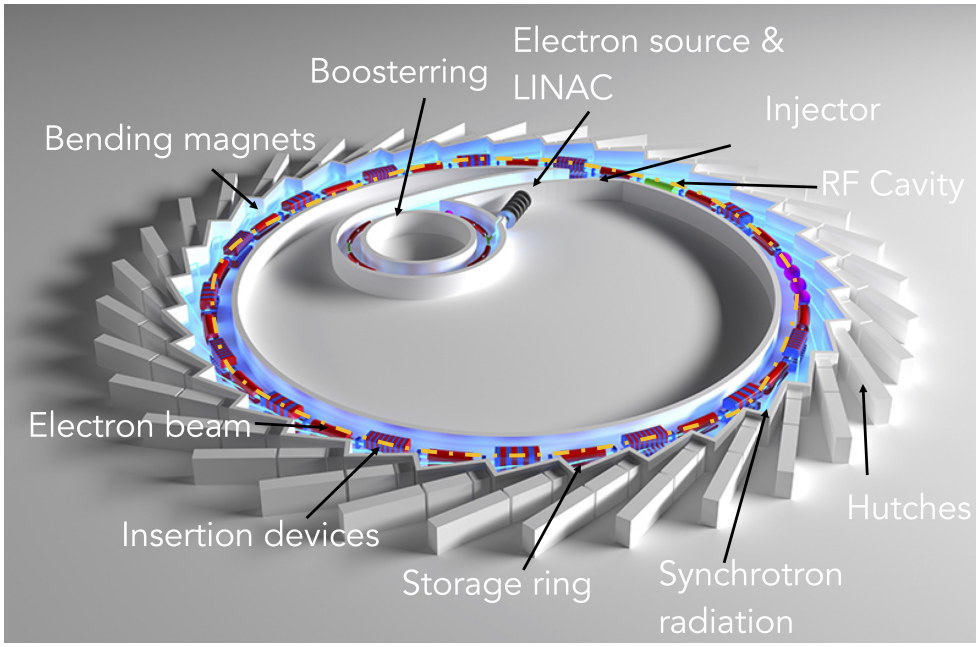

Figure 22: Schematic structure of a synchrotron. The electron beam is accelerated in the linear accelerator and booster ring and transferred to the main ring via the injector. In the ring, bending magnets keep the beam focused in orbit, while the synchrotron radiation is generated in wigglers or undulators ($2^{\mathrm{nd}}/3^{\mathrm{rd}}$ Gen). Adopted from [55] and modified.

user, giving direct access to the maximum radiation pulse frequency ($N = T_0/T_{\mathrm{RF}} = 432$). As a rule, Elettra is operated with a ring [54] filled to 95%. The higher the electron energy, the lower the maximum current in the synchrotron, because the maximum power of the CF cavity is limited. At the same time, the maximum current depends on the number of pulses in the synchrotron, since there is a maximum current that can be stored in one pulse. At $2.4\,\mathrm{GeV}$, a current of up to $150\,\mathrm{mA}$ is possible.
In order to obtain a focused beam, both quadrupole magnets and the bending magnets are used, but they produce chromatic aberration as a side effect. Attempts are made to correct this with sextupole magnets inside the ring. Twelve magnet units (bender magnet, quadrupoles, sextupoles, steering magnets) form the main ring with a diameter of $259.2\,\mathrm{m}$ and offers space for insertion devices up to $4.5\,\mathrm{m}$ in length. There are 28 beamlines in total. The experimental stations (hutches) are tangentially connected to the storage ring. The beam parameters must remain constant, otherwise the intensities of the synchrotron radiation could change rapidly. An example of a slow disturbance would be the temperature of the building or the ring structure. Therefore, later in the experiment, it will be important to take any changes in the beam or its energy into account in the evaluation. The beam position is monitored with the help of Beam Position Monitors BPM.

4.2 Gasphase - Beamline

The main task of the beamline is to produce a spot beam that is as stable as possible, whereby the shape and size change due to the wavelength change should be minimized.
The light generated by the synchrotron radiation sources is guided to the various experimental chambers by the beamlines, which have as their purpose 1) the reduction of radiological risk; 2) the reduction of the passband of the emitted radiation (monochromatization); 3) definition of the size and divergence of the beam in the interaction zone between the light and the sample under examination. The beamline used in this work is the GasPhase beamline. Figure 23 shows the structure of the beamline. There is a plane mirror (SiO_2 with gold coating) in front of the beamline, which has the task of filtering out photons above $1\,\mathrm{keV}$ by acting as a low-pass filter through its reflectivity. The beamline is not designed for photon energies above $1\,\mathrm{keV}$. A lead wall shields the experimental area with the beamline from ionizing radiation such as gamma rays or bremsstrahlung. The beamline is equipped with a $4.5\,\mathrm{m}$ long undulator, which operates at a maximum power of $P_{\mathrm{tot,max}} = 0.95\,\mathrm{kW}$ and generates linearly polarized light. The undulator has 36 periods with $\lambda_{\mathrm{u}} = 125\,\mathrm{mm}$. The undulator gap can be adjusted remotely via the beamline control system (BCS) between $31\,\mathrm{mm}$ and $99\,\mathrm{mm}$.

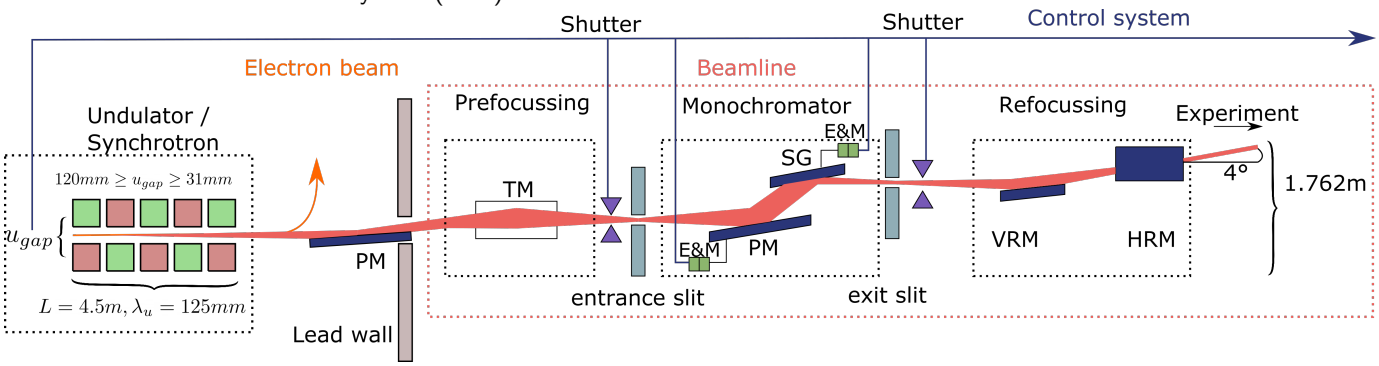

Figure 23: Schematic representation of the Gas Phase beamline. The electron beam moving in the undulator generates synchrotron radiation that hits the monochromator (plane mirror PM, spherical grating SG) through a pre-focusing system (toroidal mirror TM). The selected radiation is refocused to a point-like beam - approx. $150\,\mu\mathrm{m}$ x $150\,\mu\mathrm{m}$ (VRM-vertically refocusing mirror, HRM-horizontally refocusing mirror). The undulator gap, shutter as well as the monochromator angle (E - Encoder, M - motor) can be controlled via a control system. The image is based on [34].

A variable angle spherical grating monochromator is used as the monochromator. The angles are set by stepper motors and controlled by a Heidenhain encoder. To ensure that the entrance and exit slits remain in the same position and that the beam does not change direction when the wavelength is changed, a plane mirror is used in front of the grating. Width of both silts can vary between $5\,\mu\mathrm{m}$ and $200\,\mu\mathrm{m}$. Each mirror and grating angle can be assigned an energy. Utilizing the mathematical model for the mirror and grating angle, the energy selection can be done by a simple SET-command from the beamline control system (BCS). In addition to the direct setting of the energy, the setting of a number of steps of the motors or an angle is also possible. If certain energies are to be set, they can only be set to a precision with which the angles or the motors can be adjusted. The energetic resolution is so high that the mechanical limit of the motors is reached. At steps partly smaller than $100\,\mathrm{nm}$, the motors could make jumps (stick slip) [6] due to a not perfect surface finish.
To cover a total energy range of $13\,\mathrm{eV}$-$900\,\mathrm{eV}$, 5 different gratings are used. Depending on the coating, radius and grating constant, each grating has a different optimum with respect to the maximum photon

flux and the energetic resolution. In table 2, all five gratings are shown with their assigned energy range and possible maximum resolution.

Table 2: Energy range, Resolving Power $E/\Delta E$, flux and line density of different spherical gratings from [53]. The use of Grating 1 at the second order allows to cover an energy range otherwise not accessible.

Grating	Energy range	Lines/mm	Max. Resolving power	Flux (photons/s/100mA)	radius [cm]
G1	13-60	400	>25000	$6.3 \cdot 10^{10}$ @ $45\,\mathrm{eV}$	1700
G1 2^{nd}	40-90	800	>28000	$2.2 \cdot 10^{11}$ @$65\,\mathrm{eV}$	1700
G3	80-180	1200	>10000	$1.5 \cdot 10^{11}$ @$86\,\mathrm{eV}$	1700
G4	160-430	1200	>12000	$1.1 \cdot 10^{10}$ @$401\,\mathrm{eV}$	3200
G5	360-900	1200	>10000	$2.0 \cdot 10^{10}$ @$540\,\mathrm{eV}$	4600
G6	13-25	140	>10000	$2.0 \cdot 10^{11}$@$20\,\mathrm{eV}$	1700

The flux yield with the slit open depends on both the efficiency of the undulator and the beamline efficiency. The undulator reaches its flux maximum at about $600\,\mathrm{eV}$ [53]. The beamline efficiency, which indicates the proportion of incoming and outgoing light at the beamline, depends to a large extent on the gratings. In principle, it can be said that the highest beamline efficiency is at about $100\,\mathrm{eV}$ and drops sharply for higher grids. According to table 2, the GasPhase Beamline delivers significantly larger fluxes, especially in the lower energy range. A toroidal mirror is used for pre-focusing, a horizontal and a vertical focusing mirror for refocusing. The two refocusing mirrors allow an approximately circular spot size ($200\,\mu\mathrm{m}$) with a slit width of $20\,\mu\mathrm{m}$, which decreases towards higher energies. The beams were designed to illuminate a range of $200\,\mu\mathrm{m}$ x $200\,\mu\mathrm{m}$ homogeneously with an angular divergence of about $3\,\mathrm{mrad}$ [53]. In front of and behind the monochromator there is an additional shutter that can also be controlled via the control system. The front shutter is closed whenever the grating is changed to prevent any stress on the monochromator. The rear shutter is closed to evaluate the influence of the incident photon beam. The beamline transfers the beam behind the exit slot at a height of $1.762\,\mathrm{m}$ above the ground with an angle of 4°. In total, the monochromator is $6\,\mathrm{m}$ long next to the mirror system.

Resolution

The determination of a resonance energy is essential for the experiment, and therefore the energetic resolution $E/\Delta E$ should always be maximised.
The spectral resolution of the beamline $E/\Delta E$ is mainly influenced by three factors:
Firstly, as table 2 shows, the resolution is dependent on grating and photon energy. At the same time, the exit slit has an influence. At the same energy, the energy bandwidth decreases with a small slit and thus the resolution increases. However, the intensity decreases (lower slit $\rightarrow$ less intensity). The input slit can also influence the resolution, as it ensures that the light falls as parallel as possible on the mirrors in the monochromator. If the light is no longer parallel, it no longer falls centrally on the output slit, which can lead to defocusing effects that worsen the resolution.
The more accurately the monochromator angles can be read during an energy scan, the higher the energetic resolution of the experiment. But the nominal energy determined by the monochromator angles can deviate significantly from the actual energy. This difference can change over time, for example due to the thermal expansion of beamline components, but also energetically. The angular encoder error, which is based on interpolation function, describes this energy dependent fluctuating change in the energy difference between the actual photon energy and the measured nominal energy of the monochromator.

Interpolation is necessary because the angles to be read are smaller than the readings on the angle encoder. In addition, the return value of the encoders varies slightly even if the angles is kept constant. To improve the resolution with respect to this error, the plane mirror angle was fixed to an angle (and thus optimised to an energy) so that only an angular encoder error contributes to the result. Without this fixation the resolution is limited to 4000 [6]. If, on the other hand, the angle of the plane mirror is fixed, it leads to a much better resolution. Resolutions of up to 60,000 at $48\,\mathrm{eV}$ and 10,000 at $540\,\mathrm{eV}$ are possible.

5 Experiment

In the period between December 2021 and February 2022, a total of 3 beamtimes were conducted at the GasPhase Beamline (GAPH) at Elettra synchrotron in Trieste. The PolarX-EBIT from the Max Planck Institute for Nuclear Physics in Heidelberg (MPIK) has been transported to Elettra in order to be used in combination with the GAPH. The aim of this work is the resonance energy determination of the astrophysically relevant K_α-transition in the photoionization of Be-like oxygen at $554\,\mathrm{eV}$ and the measurement of the isotopic shift of this line between O_{16} and O_{18}. For the absolute energy determination, well-known calibration lines such as those of He-like oxygen and nitrogen are necessary to calibrate the nominal energy of the beamline. In addition, the known $1s - \pi*$ transitions of molecular oxygen were also used for calibration, which were recorded with a gas cell installed upstream of the EBIT. In the third beamtime at GAPH, the isotope shift of the same K_α transition between O_{16} and O_{18} was investigated. In order to determine the absolute energy or isotope shift, the resonance energies of each scan must be determined first. A scan is a process in which the photon energy is driven over a defined energy range with the help of the monochromator. In principle, a scan records both fluorescence data and ion data from the two detection systems (see 3.6). The preferred decay channel of the excited lines (radiative or autoionizing) indicates, which of the two signals show a more pronounced resonance. Since, as described in sections 2.4.1 and 2.4.2, the radiative decay channel for highly charged ions is usually more dominant than the autoionization decay, highly charged ions are in principle stronger in the fluorescence signal, while less strongly ionized ions of the same element are more dominant in the ion signal. In principle, the resonance energy is determined via a projection of the respective signal, whereby the photon energy of the synchrotron radiation is located on the x-axis.
After the previous discussion of the experimental setup, the first half of the evaluation explains the resonance energy determination of both the fluorescence data and the ion data. The focus is on the ion data, whereby a new method of analysing the ion data is presented in this work. The advantages and disadvantages of this method are compared with the methods used in other works. With the help of the now determined resonance energies, the absolute energy of the K_α transition of Be-like oxygen will be determined in the second half of the analysis (beamtime I, II), as well as the isotope shift (beamtime III).

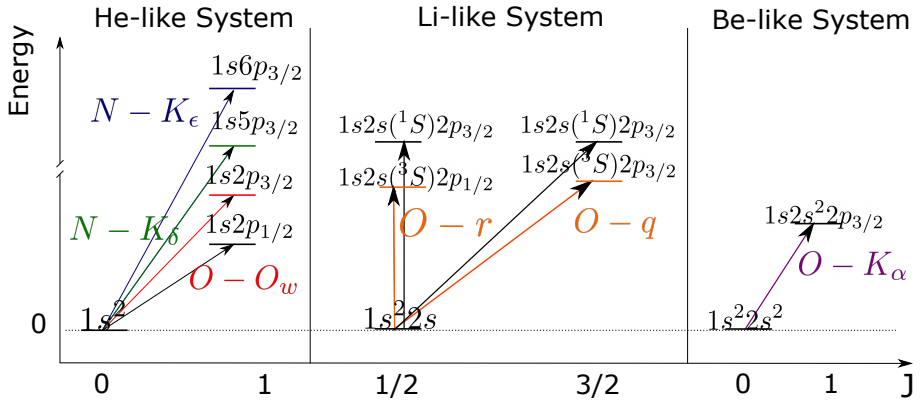

Figure 24: Overview of the transitions used in this evaluation. The associated reference values can be found in table 3.

In order to get an overview of the transitions used in this work, their resonance energies from different

Table 3: Selected transitions in He-like, Li-like and Be-like systems (in eV) which are used in this work. The calculated energies and rates calculated by the relativistic configuration-interaction method with FAC [17] are compared with the values of NIST [1] and of selected references: a:[18],e:[33] experimental values, b:[50], c:[58], d:[57] theoretical values.

Ion	Label	Lower		Upper		NIST [eV]	Ref [eV]	FAC [eV]	Rate	Signal
O_{VII}	w	$1s^2(0)$	$^1S_0$	$1s2p_{3/2}$	$^1P_1$	573.94778	$573.9614(5)^b$	573.599	$3.42 \cdot 10^{12}$	RD
O_{VII}	K_α	$1s^2(0)$	$^1S_0$	$1s2p_{1/2}$	$^3P_1$	568.54442	—	567.707	$4.20 \cdot 10^{8}$	RD
O_{VI}	K_α	$1s^22s$	$^2S_{1/2}$	$1s2s(^1S)2p_{3/2}$	$^2P_{3/2}$	568.213	$567.701(5)^c$	568.056	$2.75 \cdot 10^{11}$	RD
O_{VI}	K_α	$1s^22s$	$^2S_{1/2}$	$1s2s(^1S)2p_{3/2}$	$^2P_{1/2}$	568.213	$567.696(5)^c$	568.051	$2.98 \cdot 10^{11}$	RD
O_{VI}	q	$1s^22s$	$^2S_{1/2}$	$1s2s(^3S)2p_{3/2}$	$^2P_{3/2}$	562.593	$563.110(2)^c$	562.356	$2.64 \cdot 10^{12}$	RD
O_{VI}	r	$1s^22s$	$^2S_{1/2}$	$1s2s(^3S)2p_{1/2}$	$^2P_{1/2}$	562.593	$563.014(2)^c$	562.310	$2.62 \cdot 10^{12}$	RD
O_{V}	K_α	$1s^22s^2$	$^1S_0$	$1s2s^22p_{3/2}$	$^1P_1$	—	$554.144(7)^a$ $554.250(180)^e$	553.4065	$2.63 \cdot 10^{12}$	AU
$O_{\mathrm{V,18}}$	K_α	$1s^22s^2$	$^1S_0$	$1s2s^22p_{3/2}$	$^1P_1$	—	—	553.4084	$2.63 \cdot 10^{12}$	AU
N_{VI}	K_ϵ	$1s^2$	$^1S_0$	$1s6p_{3/2}$	$^1P_1$	538.499	$538.493(1)^d$	537.399	$1.06 \cdot 10^{11}$	RD
N_{VI}	K_δ	$1s^2$	$^1S_0$	$1s5p_{3/2}$	$^1P_1$	532.647	$532.529(1)^d$	531.459	$6.54 \cdot 10^{10}$	RD

sources were compared for all transitions of HCI useful in this evaluation in table 3. The energies calculated with the Flexible Atomic Code (FAC) (with corresponding excitation rates) are compared with the values from NIST and selected references (experimental as well as theoretical). In addition, it is marked whether the respective resonance is mainly to be expected in the fluorescence signal (RD) or in the ion signal (AU). A graphical overview can be seen in fig. 24.

5.1 Experimental Setup

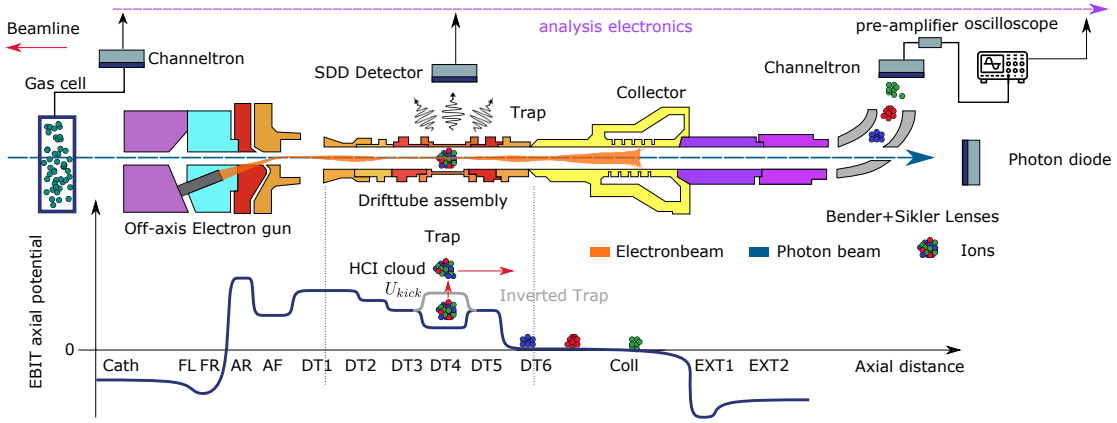

Figure 25: Measuring principle: The monochromatic photon beam of the GasPhase beamline, which is axially overlapped with the ion cloud, excites the HCI stored in the PolarX-EBIT. The fluorescence photons are measured via 2 SDD detectors. The ions are extracted via a beamline and are detected separately via a q/m-dependent ToF measurement.

The components presented in the last chapter are now combined into one experiment. The monochromatic photon beam of the GasPhase beamline excites the HCIs. The fluorescence signal is measured via the two SDD detectors attached to the EBIT and at the same time the ions present in the EBIT are extracted at regular intervals (trap is inverted) and brought to a channeltron detector (see chapter 3.7) via an ion beamline. Via the q/m dependence of the ToF, the different ions are separated and displayed on an oscilloscope. During a scan, the photon energy is shifted over a predefined energy range with the help of the monochromator. Furthermore, a gas chamber was installed between the beamline and the EBIT, which allows additional measurements with gas (e.g., O_2). The experimental setup can be seen in fig. 25 and 26.

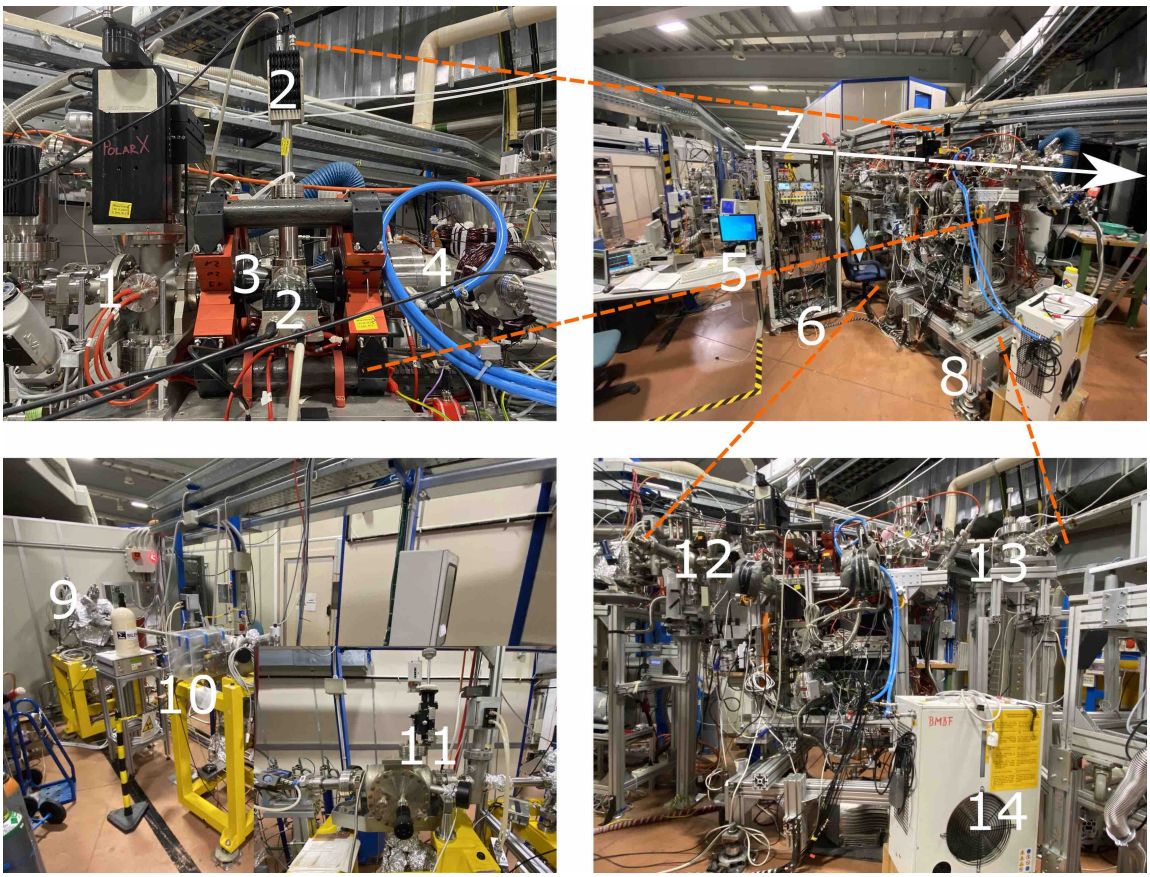

Figure 26: Photographs of the experimental setup at the Elettra Synchrotron, Trieste. In the upper left are the EBIT chamber (3), electron gun with manipulator (1), collector (4) and the two SDD detectors (2). In the upper right can be see the workstation (5), the control- and recording system with PC (6), the EBIT itself (8) and the orientation of the GasPhase beamline (7). The GasPhase beamline is shown in the lower left picture with the hutch (9), the monochromator (10) and the exit slit (11). The lower right picture shows the additional gas chamber, the photodiode and the water chiller (14).

5.2 Settings

Before each measurement, four sections of the experiment generally need to be optimized or checked. This includes optimizing the EBIT potentials, optimizing the photon and ion beamlines, mechanically adjusting the EBIT relative to the photon beam (overlap) and setting the correct scan parameters.

EBIT + Ion Beamline In addition to the classic settings of the EBIT, such as trap depth or transmission, care must also be taken that the EBIT only produces the desired ions. The electron beam energy in PI experiments must always be below the ionization energy of the HCI where the PI is observed. In order to detect the highest possible ion signal, the number of ionizable HCI within the EBIT must increase by increasing the electron current from the gun at the same time as the transmission. Moreover, the optimization of the ion beamline must play a significant role, since different q/m ratios influence the guidance of the HCI beam. Therefore, the beamline is optimised for the ions to be investigated.

Photon Beamline To achieve the optimal photon flux with the best possible resolution with respect to an energy, three things must be taken into account. Firstly, the undualtor gap have to be optimized to this energy (see section 4.1.3), secondly, the correct grating have to be chosen (see section 4.1.3), since the beamline efficiency depends significantly on it. Because the experiment in this work was never operated below $360\,\mathrm{eV}$, grating 5 was always used. The final option is to change the size of the output slit. The larger this is chosen, the stronger the photon flux, but the smaller the resolution. The photoflux is optimized by a photodiode inserted behind the EBIT (see also in fig. 26). The slit must therefore be a compromise between the required flux, and the time available for the measurement. Besides slit size, the grating as well as the angular encoder error (see 4.2) have an influence on the resolution. Therefore, the (plane) mirror angle is fixed as described in 4.2 so that only one angular encoder error (grating) is included in the inaccuracy of the scan. The mirror angle is thereby optimized to an energy in which the light hits the output slit centrally. However, with fixed angle and increasing distance from the energy optimum, defocusing effects become stronger, such that the beam no longer hits the slit centrally and thus resolution and line shape become significantly worse. Therefore, the measured scanning range should never have too large energy differences ($\pm 30\,\mathrm{eV}$).

Overlap For the photons to be ionized at all, an overlap between the photon beam ($200\,\mu\mathrm{m}$ x $200\,\mu\mathrm{m}$) and the ion cloud with a radial spread of $100\,\mu\mathrm{m}$ have to be achieved. This can be ensured either by changing the position of the EBIT in relation to the beamline via XYZ manipulators or by slightly shifting the ion cloud via variations of the electron gun. However, the latter is less suitable, as the gun has an optimal position, namely as described in chapter 3.2, where the magnetic field vanishes. A simple method to check or optimize the overlap is to excite a line with a high cross section resonantly - in this experiment the K_α-line of He-like oxygen (O_w) - where overlap changes are clearly visible in the fluorescence. The position of the EBIT is changed until the fluorescence shown in a real-time diagram is at its maximum.

Scan Settings Each scan requires three input parameters: The scan energy range $[E_1..E_2]$, the number of energy steps, the measurement time per step t_record and the scan mode. In the normal scan mode, the motor commands are sent to the grating motor one after the other in order to only change it during the scan. There is no control whether the command has been converted and whether an acquired energy change has occurred. Since the energetic resolution is so high that the motor works at the edge of its mechanical limits ($< 100\,\mathrm{nm}$ [6]) it can happen that the motor executes the set command only partially

or not at all. This drastically reduces the energy range. To solve this problem, a further scan mode was introduced ("precision scan"), which queries after each positioning command of the stepper motor whether the angle or the energy was set correctly within a tolerance range. Only if the energy is within the tolerance range, the partial measurement with the measuring time t_{record} is started. The output of the scan is the lst. file. file with the fluorescence data and a log file with the ion data. For each measurement step three equivalent scales for the energy are recorded: steps, mirror angle and energy, the latter being the nominal energy. For each fit performed in the upcoming analysis, a least-square fit is applied.

5.3 Fluorescence data

The fluorescence photons from the deexcitation of excited states leave the trap chamber at drift tube 4 and are detected vertically and horizontally by two SDD detectors. The detectors record a 1D spectrum for each monochromator step, resulting in a 2D spectrum. Thus each scan thus has two 2D spectra, which can then be analyzed. If a fluorescence photon energy range - region of interest (ROI) - is defined, a one-dimensional fluorescence spectrum can be obtained by projecting the ROI to the x-axis (monochromator energy axis). Due to anisotropy effects (more on this in [51]), the resonance yield can be different for the two detectors. If the effects are negligible, both spectra can be summed to get a better signal-to-noise ratio. The error of the centroid determination depends significantly on the spectral shape of the signal, which can be changed via the beamline parameters such as the exit slit width. In fig. 5.3 a fluorescence photon data set of O_{w} ($1s^2 \rightarrow 1s2p_{3/2}$) is shown. The projection was fitted with a gaussian curve to determine the nominal resonance energy. Since the measurement process is a counting event, Poisson statistics can be applied meaning that the square root of the number of events has to be used for the error of the single projection value.

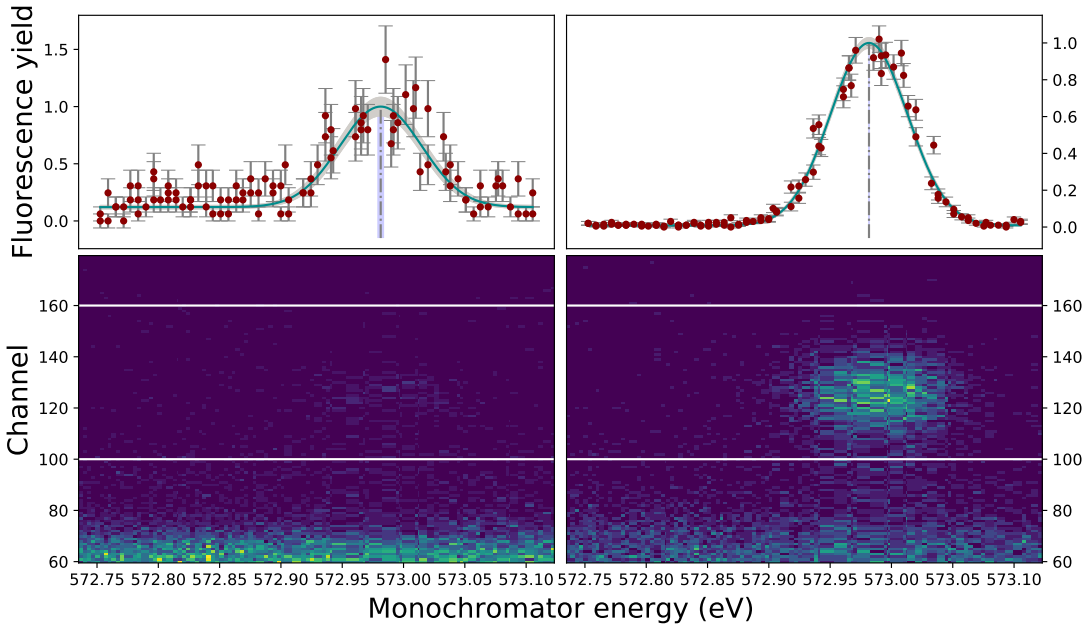

Figure 27: Comparison of the two fluorescence spectra of O_{w} from the vertical and horizontal detector. The ROI is shown with two horizontal lines. A gaussian profile was fitted to the signal in each case.

5.4 Photoion data

5.4.1 Oscilloscope data

Parallel to the fluorescence photon recording of the SDD detectors, the recording of the ToF spectra (28) for the ions stored in the EBIT runs. As described in section 3.6.2, each ToF t_{ToF} can be assigned to a q/m ratio and thus the charge distribution of the EBIT can be measured via a ToF measurement. Each ToF corresponds to an initially unknown q/m ratio, which has to be determined by a calibration. For each monochromator step, a 1D ToF spectrum (consisting of 8192 channels) is recorded by the oscilloscope. The mapping from channel to time is the same for all ToF spectra and they can be converted into each other using a linear assignment. Each scan thus consists of several individual ToF spectra. During a measurement, the trap is dumped with a frequency f_{dump} and each incoming ion stream generates a signal at the channeltron at the end of the ion beamline. Signals measured in t_{probe} ($t_{\mathrm{probe}} \cdot f_{\mathrm{dump}}$) are averaged by the oscilloscope. The ion signal is amplified both in the channeltron, preamplifier and internally in the oscilloscope, which has different amplification levels. As discussed in 3.5.2 b), the dumping frequency has an influence on the signal strength of the ion signal, but it was found that this influence is clearly small in comparison with the influence of the voltage applied to the channeltron. It has been determined that a dumping frequency of 1 Hz is at its optimum for the ion yield. During the beamtime, it has been found that it is very helpful for subsequent data analysis to record a low and a highly amplified oscilloscope image simultaneously in order to provide a large dynamic range for both very strong and weak ions. The full representation of large peaks is relevant for the ToF calibration, the high resolution at small peaks for the determination of HCIs generated by resonant photoionization, which have significantly lower intensities than those produced directly by the EBIT. However, the strongly amplified signal has the disadvantage of oversaturation at large peaks. A typical time-of-flight-1D spectrum (averaged over all monochromator steps) is shown in fig. 28. Both the high and the low gain signals were displayed, whereby the last one was amplified by a factor of 2 for reasons of comparability.

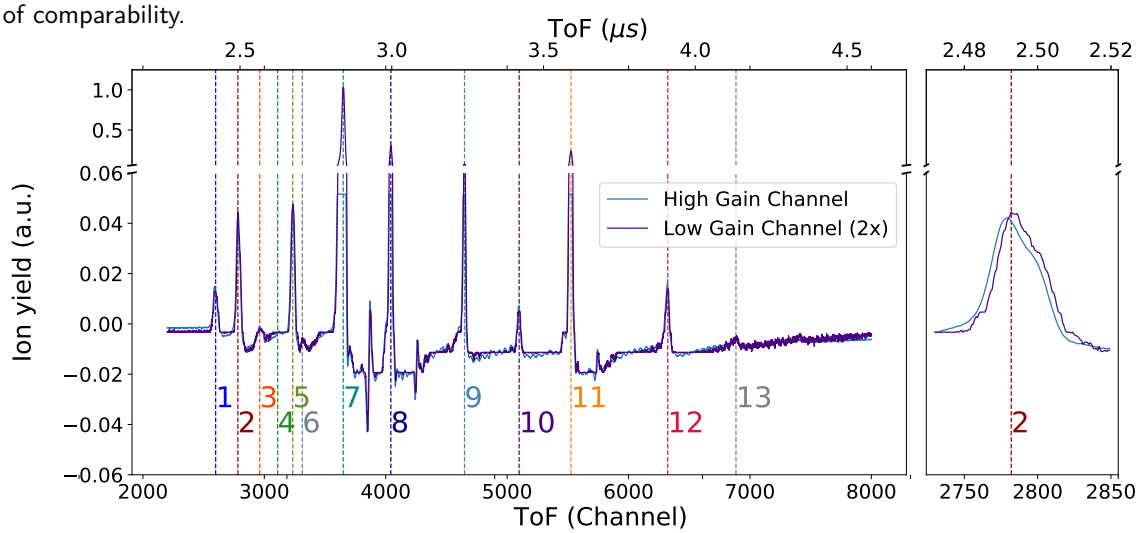

Figure 28: 1D ToF spectrum of the extracted ions from the trap. All ToF spectra (in μs and channel) of a scan were averaged. Each peak (1-13) corresponds to a specific q/m ratio. Both high and low amplified signals are shown, with the last one being displayed by a factor of 2 to better show the differences. A close-up of one peak is shown on the right.

Clearly recognizable are the characteristic features of the two signal amplifications. The high gain signal resolves the signal much better for small intensities and is therefore suitable for the determination of small peaks, whereas the low-amplification signal does not oversaturate. In addition, a characteristic delay pulse can be seen at large peaks. These peaks are initially identified as non-physical pulses, and this assumption is justified in section 5.4.3. The fact that high and low gain signals have a slight horizontal offset (see fig. 28 on the right) also plays a role in the further evaluation.
If the 1D ToF spectra of a scan (usually between 10 and 50 energy steps) are plotted against the monochromator energy, the result is a 2D spectrum. A typical 2D ToF spectrum can be seen in fig. 29 and 30.

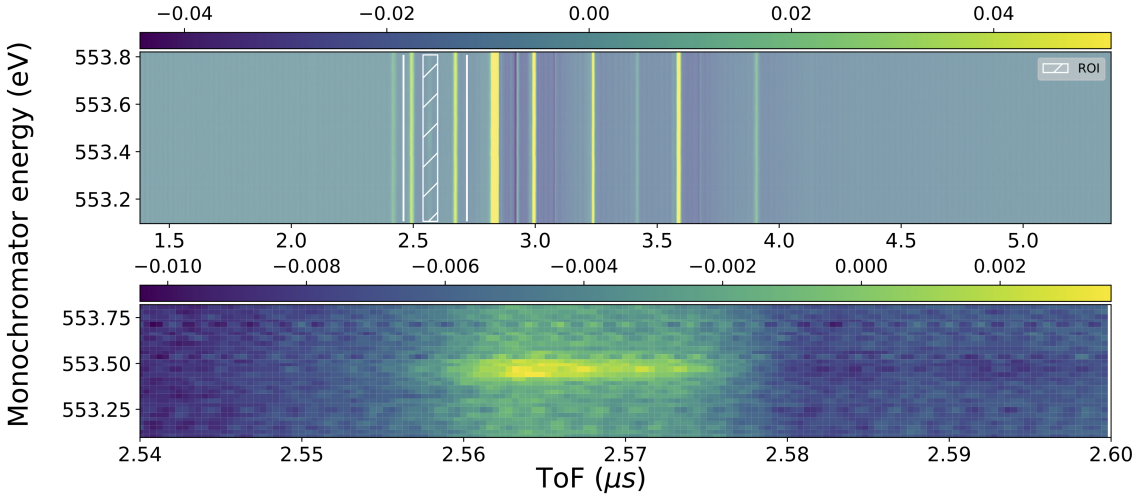

Figure 29: 2D ToF spectrum of the high gain signal: All 1D ToF spectra of a scan were plotted against the monochromator energy. A continuous line represents an ion that was generated directly by the EBIT and does not represent a resonant process. The lower figure shows a close up of a ROI selected in the upper figure (white striped lines). The energy dependent change in intensity is characteristic for a photon induced process.

Each vertical line represents a peak from the 1D ToF spectrum. Similarly, a solid line means that the ion was produced over the entire energy bandwidth and therefore does not represent a resonant process. These ions are produced directly by the electron beam from the EBIT. However, if one selects a small ToF region (white-striped area in the upper diagram of fig. 29), a large dot (instead of a line) can be seen. This dot corresponds to the photoionization of a specific ion. If one now forms the projections on the y-axis by performing the summation in the given ROI (see left plot in fig. 30), the resonance energy can be determined by fitting a gaussian profile to the data. A more sophisticated approach on the modelling of the ToF signal will be discussed in section 5.4.3.
The same ROI from diagram fig. 29 can be seen in fig. 30, where the total section has been slightly enlarged (see white lines in fig. 29) in order to also see two of the saturated lines. The x-axis projection corresponds to fig. 28. With the help of a ToF calibration, which is determined in the section 5.4.2, it is possible to make a clear assignment of the ToF peaks in the x-projection. In fig. 31 a 3D representation is shown where individual ToF spectra can be seen on the right, which results in the overall representation on the left.

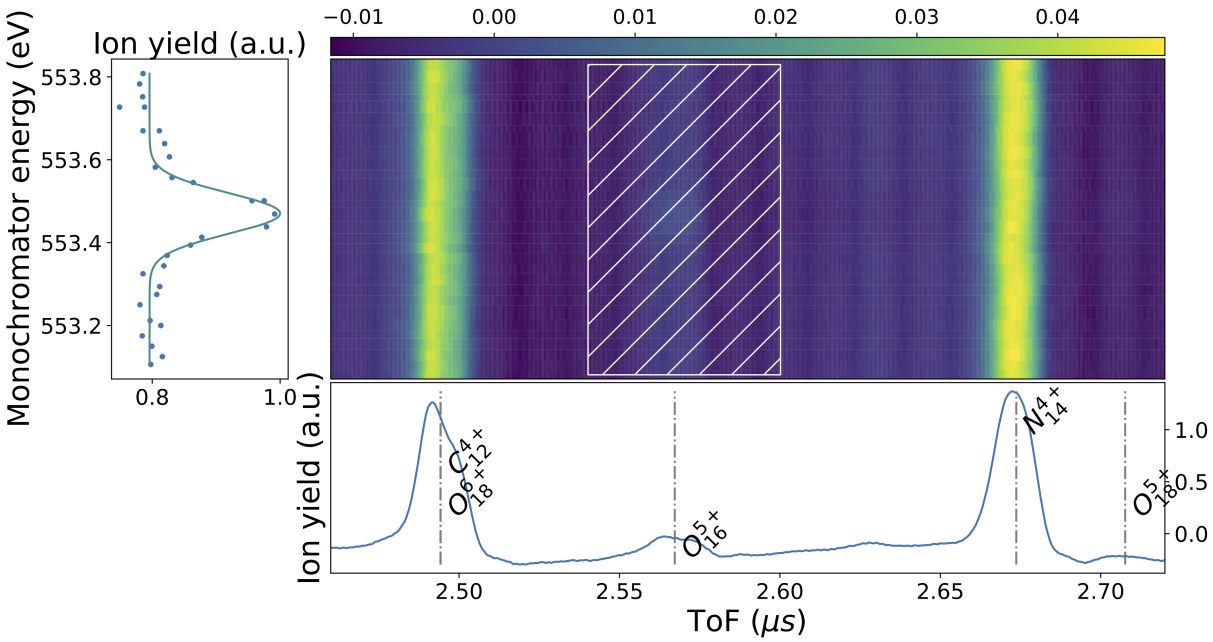

Figure 30: The 2D ToF spectrum of the high gain signal is shown: on the left is the y-projection calculated by summing the white-streaked ROI. The resonance energy can be determined via a gaussian fit. In the bottom plot, the x-projection of the entire image is shown. Using a calibration, obtained from section 5.4.2, a clear assignment of ToF peaks was possible.

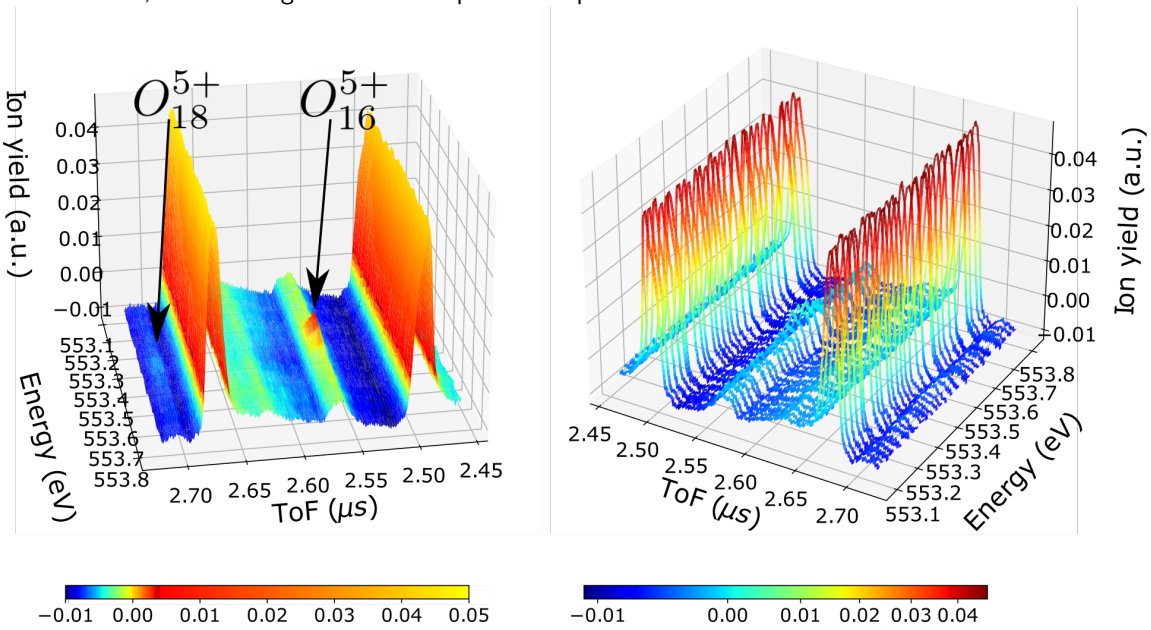

Figure 31: 3D representation of the highly amplified signal from various angles (zoomed in). On the right are the individual 1D ToF, which are shown continuously in the left image. In the left image, a different colour map was used to make the small peaks visible.

5.4.2 Calibration

To assign a q/m ratio or a HCI to a peak of the 1D ToF spectrum, a ToF calibration is necessary. Each time of flight t_{ToF} can be assigned to a q/m using

$$t_{\mathrm{tof}} = \frac{L}{v} = L\sqrt{\frac{m}{2qU}} := sU\sqrt{\frac{m}{q}} + t_0 \tag{65}$$

as described in section 3.6.2. Where L is the path length, U the acceleration voltage and t_0 a time offset. sU and t_0 represent the calibration parameters. The six largest peaks are selected as calibration points (peak no.: 2, 5, 7, 8, 9, 11 from fig. 28). These peaks, which correspond to specific ions, are independent of the photon energy, i.e. they are present throughout the entire scan. Since peaks 7, 8 and 11 are oversaturated in the high gain signal, the low gain signal is used instead. Since the positions of the peaks change slightly over the scans and individual ToF per scan, although the ion beamline remains unchanged, the centroids of the peaks of 20 scans with 30 1D ToF per scan are used for a good error estimation. For each ToF, a total of seven peaks are fitted with a Gaussian, whereby the two strongest peaks (7 and 8) are additionally fitted with a delay pulse in the form of two separate Gaussians. Figure 33 shows an exemplary gaussian fit of a 1D ToF.

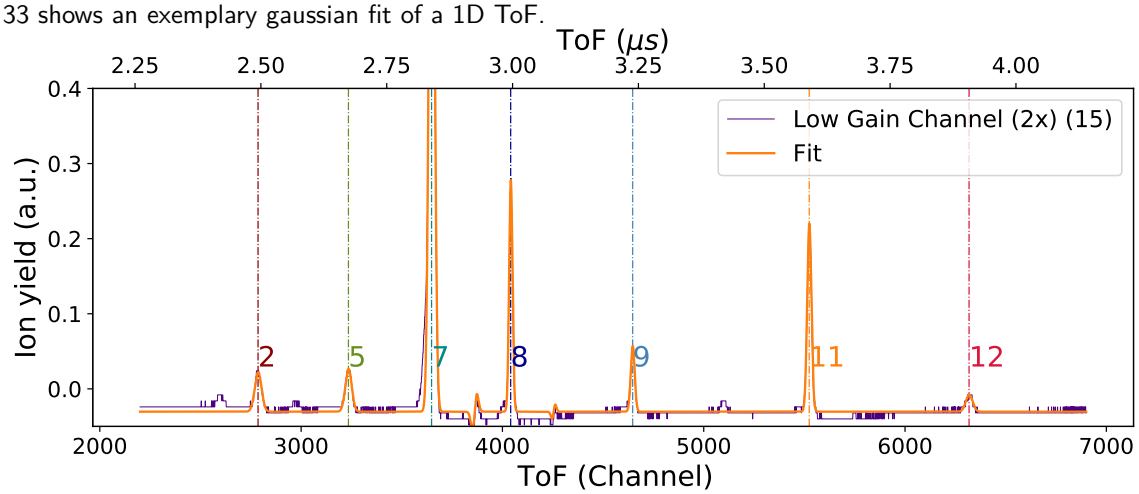

Figure 32: The determination of the centroids for the six calibration peaks using the low gain signal in one 1D ToF of one scan (y-axis is cropped). This fit was carried out for 20 scans with 30 ToF spectra each. For the two largest peaks, an additional signal consisting of two gaussian signals was also fitted.

If the centroids obtained from the individual fits (in ToF channels) are displayed in a histogram and fitted with a gaussian profile, fig. 33. Each of these fits represents the centroid of a calibration point, using the standard deviation as the error.

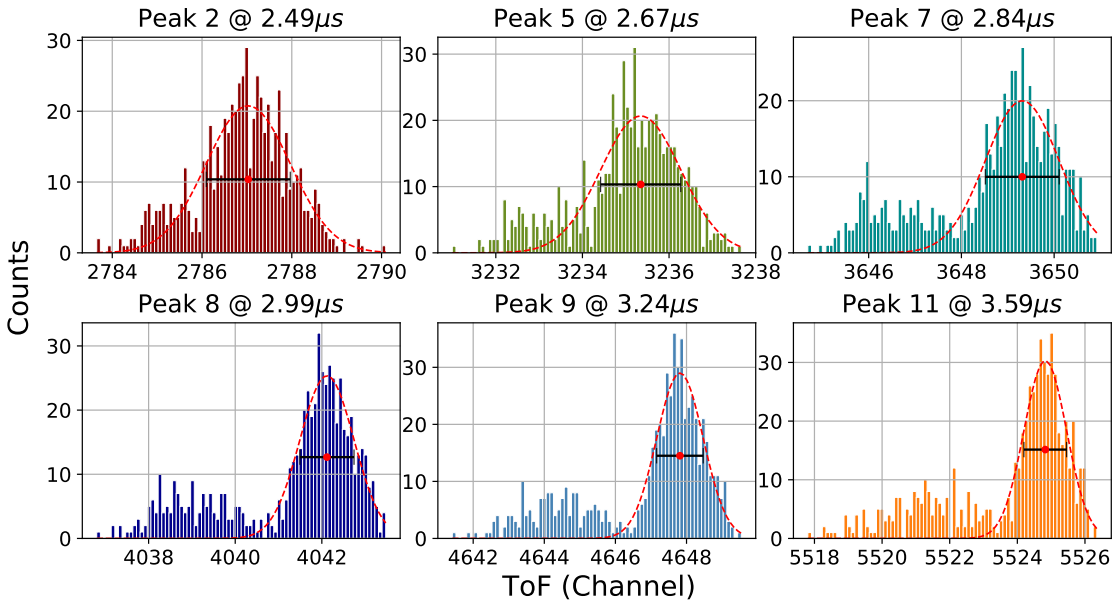

Figure 33: Calibration of ToF spectra. For each of the six calibration points, the centroid was determined (in ToF channel) for all ToF spectra (low gain) (see fig. 32) and plotted in a histogram. Using a gaussian fit, the ToF used for the calibration can then be determined, whereby the σ of the fit is used as an error.

The centroids obtained in ToF channels are converted to a corresponding time by a linear mapping between channel and time (constant for all ToF spectra). If q/m ratios are assigned to these calculated times, the fit parameters sU and t_0 can be determined via the fit with eq. 65. The assigned q/m values can be found in table 4. This can then be used for peak identification of unknown peaks for a particular scan.

Figure 34 shows the high gain signal of a scan averaged over all ToF spectra (black), with the respective peaks marked in purple. The high gain signal was used because the small peaks to be identified are better resolved there. In addition, the inverted fit function (q/m against ToF) with an error band (blue) was plotted. The calibration points used are marked both in the signal curve (green) and in the inverted calibration curve (red). Both points belonging to a calibration point have the ToF determined from the histogram, but once the value of the signal is taken as the y-value (green) and the other time the assigned q/m (red points). The ToF errors of the calibration points were each converted into a q/m error (necessary because of the inverted visualisation) using the error band of the fit and displayed in the residual. If the q/m assignment is correct, the red points lie on the inverted calibration curve, or on the zero line in the residual. Via the calibration, each q/m ratio can be assigned to a ToF (gray lines). If these are in the error band of the peak to be determined (purple band), the peak is identified. For individual peaks, it should be noted that the low gain signal used for the calibration points is clearly different from the high-gain signal (see also fig. 28 right). This can also be seen, in peak 2 in fig. 34, where the calibration point differs significantly from the displayed scan. Since the peak identification of a scan should be valid for all scans (if the beamline is not changed between scans, the calibration should apply to all scans.), the ToF error of a single peak is estimated. Therefore, a 10-fold larger error than that of the calibration points was estimated for the inaccuracy of the ToF peaks in a scan (purple band). In table 4, the determined peaks with estimated error as well as the assigned q/m ratio and HCI are shown for the scan displayed in fig. 34. In addition, the calibration points used in fig. 33 are shown. This identification is valid for all scans where the beamline has not changed.

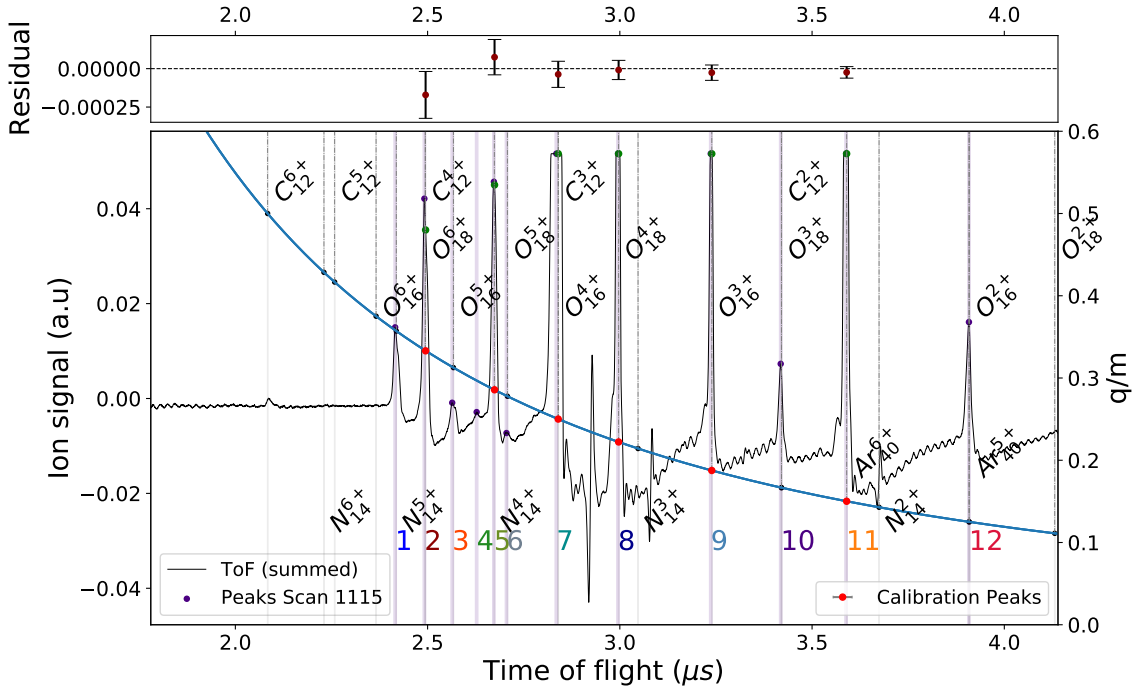

Figure 34: ToF Calibration: The averaged signal of a scan (black) was plotted with the inverted fit function (blue). For selected q/m ratios, the corresponding ToF was calculated and plotted (black dashed). If the ToF time is within an error band of an unknown peak (purple), the peak has been identified. The calibration points are marked on the signal curve (green) and on the inverted fit function (red). Shown above is the residual of the fit function, where the ToF errors of the calibration points were each converted into a q/m error using the error band of the fit.

Table 4: Peak identification: A q/m ratio or HCI can be assigned to each ToF peak for on specific scan with the help of the calibration. The ToF of the signal shown in fig. 34 were identified. In addition, the ToF used for calibration are shown (*). This identification is valid for all scans when the beamline has not changed.

Peak	ToF [μs]	q/m	HCI	q/m HCI	$\mathrm{ToF}_{\mathrm{Calib}}$ [μs]
1	2.415(3)	0.3582(9) →	N_{14}^{5+}	0.3570	—
2*	2.491(3)	0.3343(8) →	C_{12}^{4+},O_{18}^{6+}	0.3333	2.4949(3)
3	2.565(3)	0.3133(7) →	O_{16}^{5+}	0.3126	—
4	2.626(3)	0.2973(7) →	—	—	—
5*	2.673(3)	0.2859(6) →	N_{14}^{4+}	0.2856	2.6741(3)
6	2.705(3)	0.2783(6) →	O_{18}^{5+}	0.2778	—
7*	2.835(3)	0.2510(5) →	C_{12}^{3+},O_{16}^{4+}	0.25	2.8397(3)
8*	2.995(3)	0.2226(4) →	O_{18}^{4+}	0.2222	2.9968(2)
9*	3.238(3)	0.1878(3) →	O_{16}^{3+}	0.1876	3.2391(3)
10	3.418(3)	0.1670(3) →	O_{18}^{3+},C_{12}^{2+}	0.1667	—
11*	3.588(3)	0.1503(2) →	Ar_{40}^{6+}	0.1501	3.5899(3)
12	3.908(3)	0.1251(2) →	O_{16}^{2+},Ar_{40}^{6+}	0.1250	—

5.4.3 Modeling of the ToF signal

For further evaluation, it is important to take a closer look at the ion signal produced by the HCIs. Since in this work ion of relatively small quantities are investigated and these consequently produce low intensities in the ToF signal, it must be ensured that the ToF signal is interpreted correctly. In this way, it is possible to separate the different influences of signals triggered by different HCI from each other, which makes it possible to identify small signals well. In the ideal case, a delta-shaped HCI input pulse triggers a delta-shaped voltage pulse proportional to its height, which is displayed on an oscilloscope. As already explained in 3.6.2, this output signal behaviour does not correspond to the signal detected with the PolarX-EBIT. In fig. 35 the signal response of an ideal delta-shaped HCI input pulse in an ideal electronics is compared with the signal response of a gaussian-shaped HCI input pulse with the electronics used in the experiment.

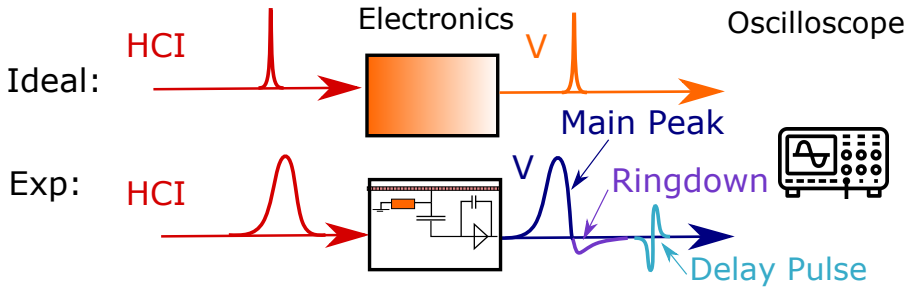

Figure 35: Comparison of the signal response of an ideal delta-shaped HCI input pulse in ideal electronics with the signal response of a gaussian-shaped HCI input pulse with the electronics used in the experiment. The final signal response consists of the main signal and two electronic artifacts, the ringdown signal and a delay pulse.

Each HCI pulse arriving at the channeltron (which has the same function as a secondary electron multiplier as MCP) causes two electrical artifacts (see fig. 35) in addition to the actual main pulse via the channeltron electronics (see fig. 17). The real input pulse of the HCI is gaussian-shaped because the ions with the same q/m ratio do not all arrive at the same time due to an extended ion cloud (see also section 3.6.2). The charge Q generated in the channeltron by the HCI pulse hits the anode within the pulse duration dt and charges the capacitor according to its capacity $\frac{dQ}{C} = dU$. This leads to a current pulse of

$$I_{charge} = C\frac{dU}{dt}. \tag{66}$$

This current pulse represents the main signal and is proportional to the number of incoming HCI. After the main pulse has charged the capacitor, the capacitor is discharged over the resistance of the RC element and generates a negative current that drops exponentially to zero. This discharge process is referred to in the following as the ringdown signal. Both the main signal and the ringdown signal are then converted in a preamplifer into a voltage signal that is displayed on the oscilloscope. In addition, as already shown in fig. 28, a delayed sinusoidal delay pulse appears, which always has the same shape of the input signal and whose amplitude is apparently proportional to the main peak. This signal is referred to in the following as the delay pulse. Both artifacts have no physical origin and do not provide any new information. On the contrary, due to the dependency of the artifacts on the signal strength of the main peak, they may cover small peaks and cause a loss of information. Both artifacts will now be discussed.

Ringdown The ringdown signal is a prominent valley-like development of the signal after each peak. It is generated by the discharge process of the RC element ($\tau = RC$) with the discharge current

$$I_{\text{discharge}}(t) = -I_{max}e^{-t/\tau} = -\frac{U}{R}e^{-t/\tau} \tag{67}$$

after the capacitor has been charged with I_{charge} before (main signal). Q is the charge deposited by the channeltron pulse and $U = Q/C$ is the voltage across the capacitor after charging. Since it is a discharge process, the current is negative and exponentially approaches the zero-line. Depending on whether the input pulse is delta-shaped or gaussian-shaped determines whether eq. 67 is sufficient to describe the ringdown signal. In the case of a delta pulse, the eq. 67 is adequate to describe the (undisturbed) exponential discharge. In the case of a gaussian input signal, this is no longer the case, since the gaussian input pulse not only influences the main signal by becoming Gaussian itself, but also the ringdown signal, since there is a superposition of discharge and charging process due to the broad input signal. This signal can be modelled by a convolution of gaussian function $G(x) = \frac{1}{\sigma\sqrt{2\pi}}e^{\frac{-x^2}{2\sigma^2}}$ and exponential function $F(x) = e^{-\lambda x}$

$$I(y) = F(x) \circledast I(x) = \frac{1}{2}e^{-\lambda(y-\frac{\sigma^2\lambda}{2})}[1 + erf(\frac{y-\sigma^2\lambda}{\sqrt{2}\sigma})]. \tag{68}$$

With the use of I(y) the frequency response of the signal-processing electronics can be modeled. In fig. 36 the expected response signal of the evaluation electronics (blue) was plotted for an assumed delta-shaped input pulse, as well as the response signal (purple) for a gaussian input pulse.

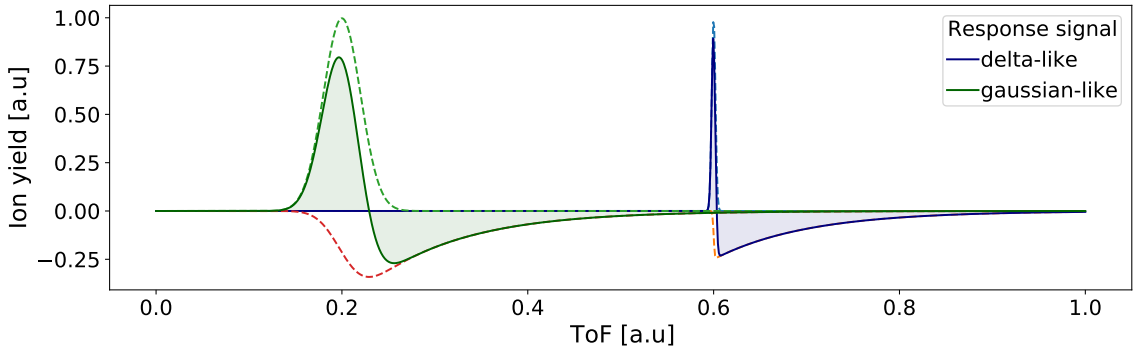

Figure 36: Comparison of the response signal to a delta-shaped input pulse and to a gaussian-shaped input pulse. Both signals consist of a main pulse and a ringdown signal resulting from the discharge process of the capacitor. A gaussian input pulse causes a broadening of both the main and the exponential discharge curves. This is simulated by a convolution of a gaussian and an exponential curve.

Delay Pulse After large peaks (7, 8 or 11), sinusoidal signals appear at regular intervals and their amplitude seems to be proportional to the main peak amplitude (see fig. 28, 34). To check the assumption that the delay pulses are always coupled to a main peak and do not represent a main peak themselves, the distance between the main peak and the delay pulse is determined for the three peaks, which feature

such delay pulses. To model the delay pulses, two Gaussians are used, which are fixed in their distance to each other and have inverse amplitudes.
In order to get a good statistical estimation, analogous to fig. 32 all 1D ToF samples (30) of 20 scans (same as used for fig.32) should be fitted to determine the position of both the main peak and the delay peak. In contrast to fig. 32, the high gain signal is used because only in this one a simultaneous fit of all three delay pulses is possible. In fig. 37, the seven largest main peaks were fitted with a Gaussian, whereby the three delay pulses (two coupled Gaussians each) were also fitted independently.

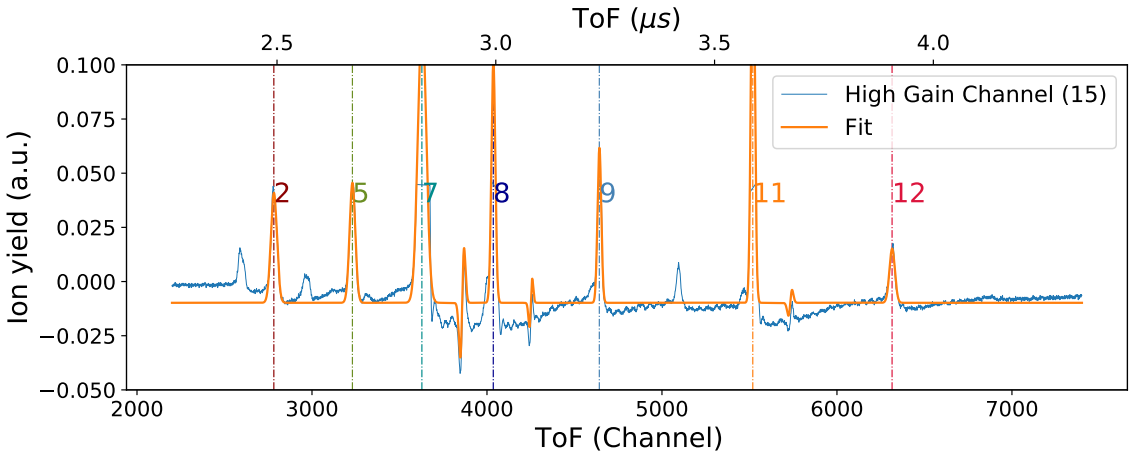

Figure 37: Determination of the centroids for the three delay pulse peaks (belonging to the main peaks 7, 8 and 11). Shown is an exemplary signal fit of a 1D ToF in a scan in the high gain signal. For each ToF, a total of 7 peaks are fitted with a Gaussian, whereby the three strongest peaks are additionally fitted with a delay pulse in the form of two separate Gaussians. The centroid of the delay pulse is always the midpoint of the two gaussian signals (fixed to each other). The fit was performed analogously to fig. 32 for 20 scans with 30 ToF spectra each. The centroids of the main peaks belonging to the delay pulses cannot be used in this fit, because they are oversaturated. For this purpose, the fit from fig. 32 is used.

From the fit of the high gain signal (fig. 37), the centroids of the main peaks cannot be determined precisely because they are oversaturated in the high gain signal. Therefore, the centroids of the main peaks (in ToF channels) are taken from the centroid-evaluation in the low gain signal fit (fig. 32) and the centroids of the delay pulses (in ToF channel) are each taken from the high gain fit. For every ToF spectrum, the difference in time between the main peak and the delay pulse peak has been determined and visualised in fig. 38 in a corresponding histogram.
By fitting a gaussian profile, one obtains an average distance between the main peak and the delay pulse peak for main each peak. The result obtained in bins is converted via a simple linear assignment between channel and time unit, as has already been done several times. The delay times of the delay pulses are in agreement within their error. This leads to an average delay time of the signal of

$$\Delta t = 83.59(8)\,\mathrm{ns} \tag{69}$$

This suggests that the delay pulse has no physical explanation and can be interpreted as an electronic artifact. The origin of the delay pulse signal could be a reflection of the pulse signal. Reflections can occur when the input resistance of the oscilloscope ($\sim M\Omega$) does not match the impedance of the cable ($\sim 1\,\Omega$). Assuming a propagation velocity of $c_{\mathrm{medium}} = 2/3 \cdot c$, this would lead to a system

length of $l = \Delta t c_{medium} = 16.72(1)\,\mathrm{m}$. Another explanation could be an artifact signal produced by the preamplifier.

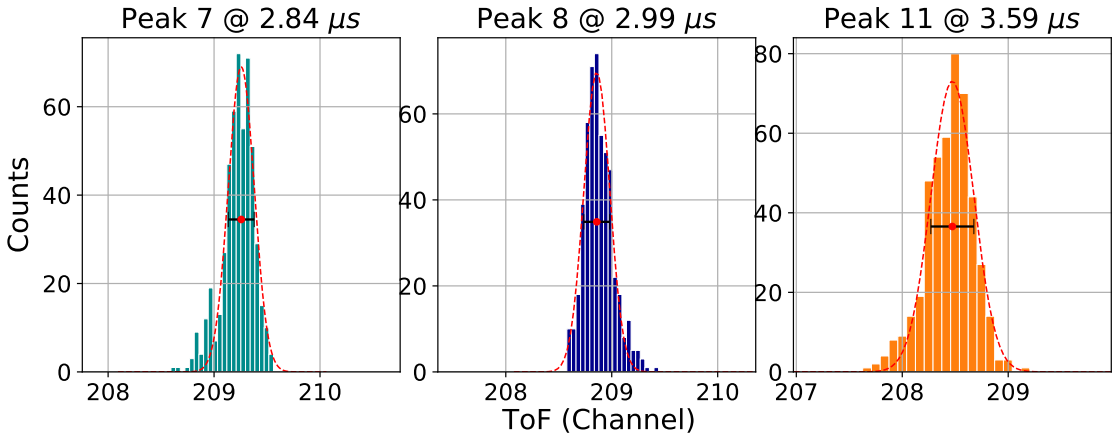

Figure 38: Determination of the time delay between the delay pulse following an initial main peak. The histograms represent the difference for a peak between the main peak and the respective delay pulse for all ToF of each scan (600 values per peak). As data origin for the centroids of the main signals, the fits of the low gain signals were used (see fig. 32), for the centroids of the delay pulses the fits of the high gain signals (see fig. 37) have been used.

As already mentioned, the amplitude of the delay pulse seems to be proportional to the amplitude of the associated main peak. This would explain why only three of the twelve identified HCI peaks have a recognizable delay pulse. It would also be another indication that the delay pulse is not a physical signal. In fig. 39, the amplitude ratios of the main peaks are shown with their respective delay pulses. As a basis for the data, the fit with the low amplified ToF signal (see fig. 37) is used again, because only there the amplitudes of the large peaks can be determined correctly (they are not oversaturated there). Since only two delay pulses can be fitted there, the amplitude ratio can only be determined for two peaks (7 and 8). This results in a ratio of 25.3 ± 0.9 (peak 7) and 20.8 ± 2.0 (peak 8). This makes it clear that it is important to take into account the delay pulse which, despite a factor of $1/20$, can be larger than the main peak under investigation.

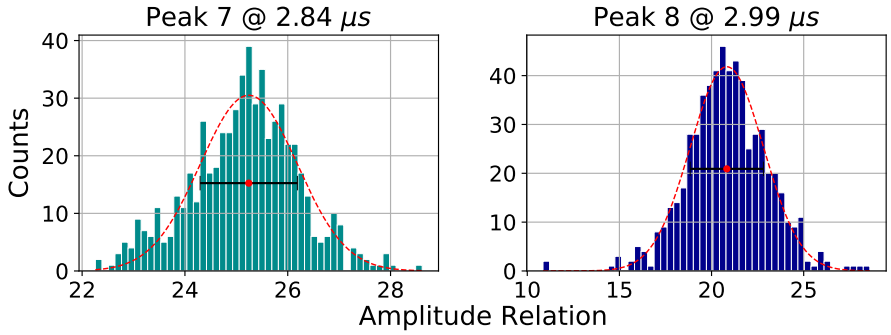

Figure 39: Determination of the amplitude ratios of the main peak and delay pulses. The data from the fit with the low gain signal (see fig. 37) was used.

Model If the entire ToF spectrum can be modelled using the response signal of the signal processing electronics, it is possible to distinguish between the influences of different peaks. This is important to isolate, for example, small peaks that are superimposed by the delay pulse peaks of large peaks. This is particularly important for the photoionized HCI investigated in this work, which has a low intensity in the ToF. For the signal model of the response signal, the main signal $G_{Main}(t)$, Ringdown (RD) $I(t)$ and the delay pulse $G_{Up}(t)$,$G_{Down}(t)$ are combined. The two delay Gaussians have a fixed distance Δt_{UpDown} to each other. Since the delay pulse (DP) triggers exactly the same behaviour as a main peak electronically, an additional ringdown signal $I(t)$ is also used for the delay pulse to simulate the ToF as well as possible. The offset C is responsible for a possible zero shift of the oscilloscope signal. This results in

$$\begin{aligned} S(t) = G_{Main}(t) + I(t - t_{RD}) + G_{Down}(t - \Delta x_{DP}) \\ + G_{Up}(t - (\Delta t_{DP} + \Delta t_{UpDown})) + I(t - t_{DP}) + C \end{aligned} \tag{70}$$

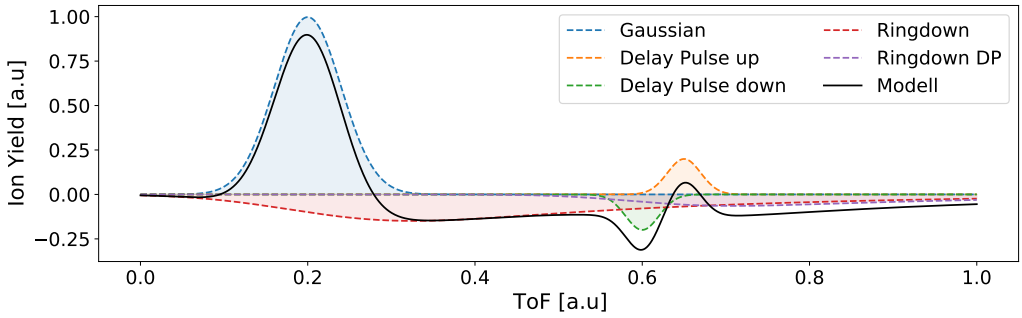

Figure 40: Complete signal model $S(t)$: The full signal model consists of the main gaussian signal peak, the ringdown signal and the delay pulse. the last is only fitted if the main peak is strong. Since the delay pulse triggers electronically exactly the same behaviour as a main peak, an additional ringdown signal for the delay pulse is also used.

With the help of this model, the ToF signal can now be fitted. Due to the 20-25 times smaller amplitude compared to the main signal, the delay pulse can only be fitted if the main signal is large enough. If the main peaks are small, the delay pulse disappears in the noise. Theoretically, the full response signal of an HCI pulse is expected to scale only with the number of incoming HCIs. Then the fit signal for all peaks would be identical except for a scaling factor. Therefore, in fig. 41, the high gain signal of a scan averaged over all ToF is fitted over using two sets of constraints for the fit parameter for eq. 70.
In one case, all fit parameters are unrestricted. In the other case, the fit parameters for the main pulse and the associated ringdown signal are the same for all peaks and coupled to each other and can only be scaled with a variable factor. In both cases, the delay pulse can only be fitted for three peaks (7, 8, 11), whereas the parameters for the delay pulse are unrestricted in both cases, except for the distance between the two Gaussians Δt_{UpDown}.

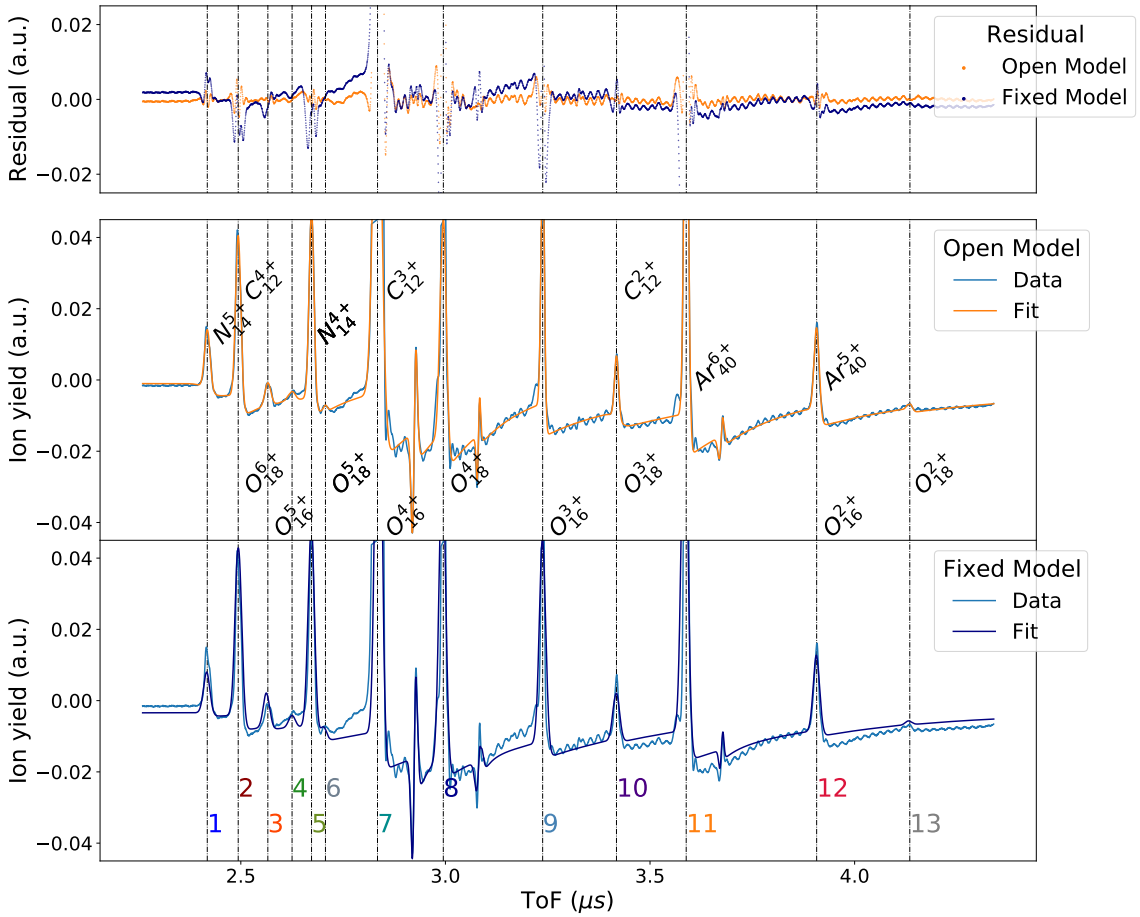

Figure 41: Global fit with eq. 70 of a high gain averaged ToF signal of a scan. Two different fit specifications were set for the main peak with its ringdown: Once all their fit parameters are open and the other time all fit parameters are fixed and only scalable with a variable factor. In both cases, an delay pulse signal was fitted for peak, 7,8 and 11, which was only fixed by Δx_{UpDown}.

First of all, it is noticeable that both fitting procedures using the new signal work very well and in comparison to the pure gaussian fit (see fig. 37), the fit quality has been significantly improved. It also shows very well that the underlying assumption that all peaks are coupled to each other and only differ except for the scaling factor is correct in the first place.
However, it must be stated that the open model approximates the actual signal much better. For further improvement of the fit, it would be necessary to combine the signal with high and low gain to prevent oversaturation of the large peak, which would improve the fit even more. Also, if a fit is only carried out in a small time-window of the ToF spectrum, the fit quality can be improved significantly (see next chapter). However, the fit with the new fit model (eq. 70) can only be performed as long as the highly amplified signal is available. If this is not the case, the simpler gaussian model must be used. In the following section, the advantages of this model for the projection and thus, for the resonance determination are discussed.

5.4.4 Projection

To determine photoionization resonances from the ion-TOF signal, an energy projection must be produced. The simplest way to do this has already been shown in fig. 30 by performing a simple summation for each ToF in a given ToF ROI. However, a suitable ROI must be set, which, if too large, will result in a poor signal-to-noise ratio due to noise and, if too small, will result in a loss of information. Furthermore, no error can be attributed to the ion-yield.
One way to solve this problem was presented in the thesis of M. Togawa [51], where a gaussian profile has been fitted to the ToF peak of interest. The area with its corresponding statistical error has been used as the value and error for each datapoint. For the signal fit, an ROI is also needed here. Again, an ROI is required to which the signal is fitted. In the case of isolated peaks that are not strongly influenced by other peaks (e.g. by ringdown signal), the ROI determination is unproblematic, since no additional signal is generated if the appropriate ROI is chosen larger (in contrast to summation). For closely spaced peaks, however, the situation is different, since the fit quality of the gaussian fit depends on the ROI.
To avoid these problems, a different method was used in this work. For this purpose, the entire ToF spectrum before the peak of interest (with no oversaturated peaks) was fitted in fig. 42 using the signal model 70 presented above. Because all the peaks in this section are small relative to the other cropped peaks, no delay pulse is necessary. Since the model is used for the projection, each of the two peaks is split into a main peak, which is modelled by a Gaussian, and a ringdown part. The area of both are proportional to the incident number of ions. The ringdown signal as well as the gaussian component of each peak has been marked. The model fit has been able to detect all HCI peaks, as there are no other signals in the residual (except for noise-like oscillating signals).

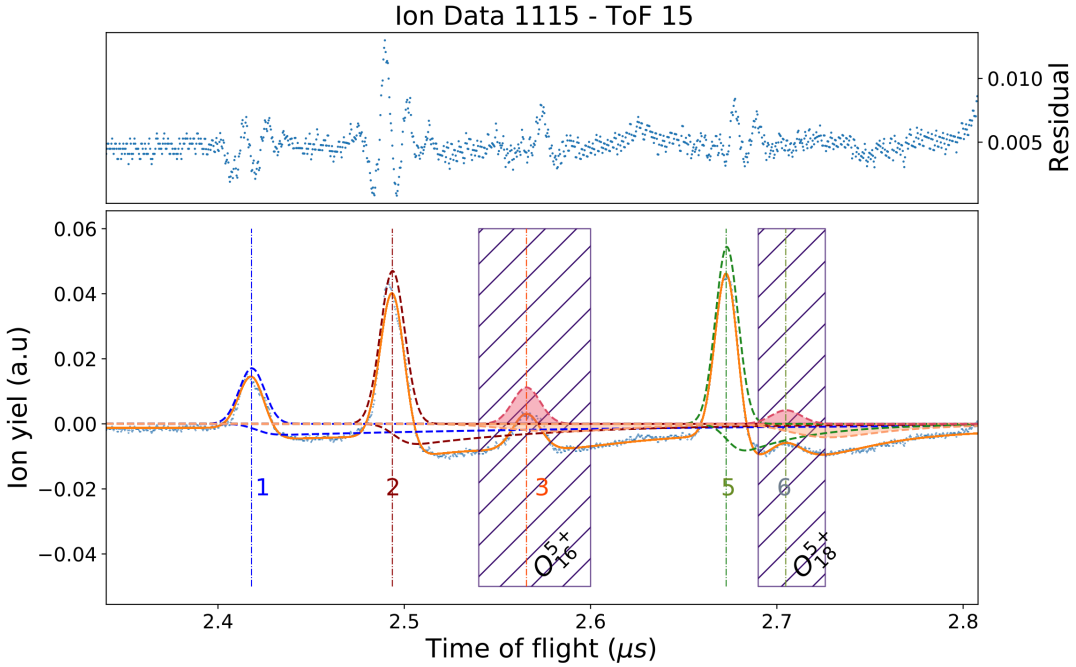

Figure 42: Model fit (orange) of a section of a ToF spectrum for the determination of a data point for the energy projection. For all six identical peaks, the Gaussian and ringdown components were marked. The purple area marks the ROI used for the other methods, the Gaussian fit and the summation.

The three presented projection methods are compared in the following for two different ion signals (O_{16}^{5+} and O_{18}^{5+}). It should be noted that the resonance of an HCI A^{q+} in the ToF is always observed over the photoionized HCI A^{q+1}. In this case, therefore, a transition of Be-like (O^{4+}) oxygen is investigated. For the other two projection methods, an ROI was defined for both HCIs (purple dashed in fig. 42), in which both the summation was formed and the Gaussian was fitted. Analogous to fig. 42 the model fit was performed for all ToF spectra of the scan used (as well as gaussian fit in ROI or summation). By plotting the corresponding projection value of the three methods (summation, area of gaussian fit and area of the gaussian and ringdown of model fit) for each monochromator step, a one-dimensional spectrum can be produced for both ion signals (O_{16}^{5+} and O_{18}^{5+}) which can be seen in 43.
For the model fit, the fit parameters of peaks 1, 2 and 5 were kept constant over all ToF spectra. Since the projection method with the signal fit provides two projection values per ToF spectra, a total of four projections are gained, whereby the respective value originating from fig. 42 (ToF 15) was marked orange.

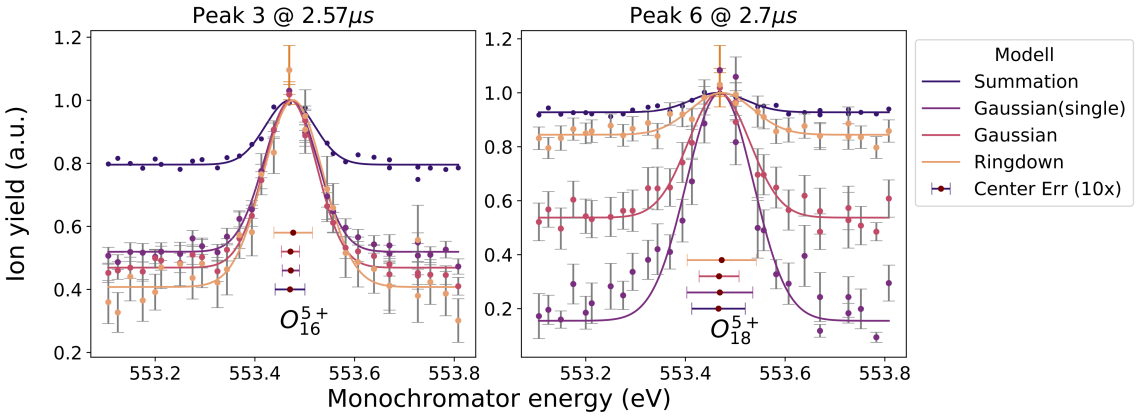

Figure 43: Comparison of the 3 projection methods: summation, gaussian fit and model fit. The resonance energy of a photoionization of Be-like O^{4+} is investigated. The values determined for each ToF, analogous to fig. 42, are plotted for each peak and fitted with the use of a gaussian profile. The result with a 10-fold magnification error is also included in each case.

A gaussian fit was carried out for each projection, whereby the error is displayed at a 10-fold magnification. If a fast and uncomplicated (as no fit is necessary) procedure is required, e.g. during the beamtime for a quick check, the summation method is sufficient. However, regardless of the physical origin of the signal, every signal in the ROI is summed and no error can be attributed to the ion-yield.
A fit is more independent of the ToF ROI, as only data that corresponds to the model is fitted. The Gaussian fit method is suitable for isolated peaks that are not strongly influenced by other peaks and their artifacts. A larger ToF ROI does not lead to a large change in the fit. This changes, however, for mainly small peaks that are under the influence of other peaks. This is not taken into account in the Gaussian model. If the peak to be investigated lies on the ringdown of another peak, then either an attempt must be made to include it locally with the help of a linear fit, or it is accepted that the quality of the fit decreases. Only through the fit of the complete ToF-spectrum is it possible to separate the individual peak influences from each other and also to identify clearly distinct peaks. At the same time, the need for ROI selection is eliminated and two energy projections can be determined for one scan (via gaussian and ringdown signals), which improves the statistical significance. In addition, significantly more signal information (improved signal-to-noise ratio) can be extracted for larger peaks (peak 3) compared to

Gaussian fitting. For small peaks (peak 6), however, the new model fit method has the disadvantage that the fit is more difficult to perform (especially ringdown signal), which leads to a decreasing signal-to-noise ratio. Another disadvantage of the full model fit is that the fit only works for the high gain signal.

5.5 Characterization of the GasPhase beamline

5.5.1 Energy drift

An important aspect of the beamline is that it has a certain energy drift over time. Due to temperature changes and other time-dependent disturbances, an energy drift in the nominal energy can occur. For a later absolute energy calibration, a systematic error must therefore be estimated. To determine the influence and strength of the shift, the K_α-line of He-like oxygen (O_w) was measured in 23 scans (30 steps of 20 seconds each) over a period of about 7 h. O_w is suited optimally for this purpose with its large excitation rate (see table 3). In fig. 44, the fluorescence spectra (projection of fluorescence data) fit 23 scans are shown, where their difference to the weighted mean value of the centroid is shown in the lower plot.

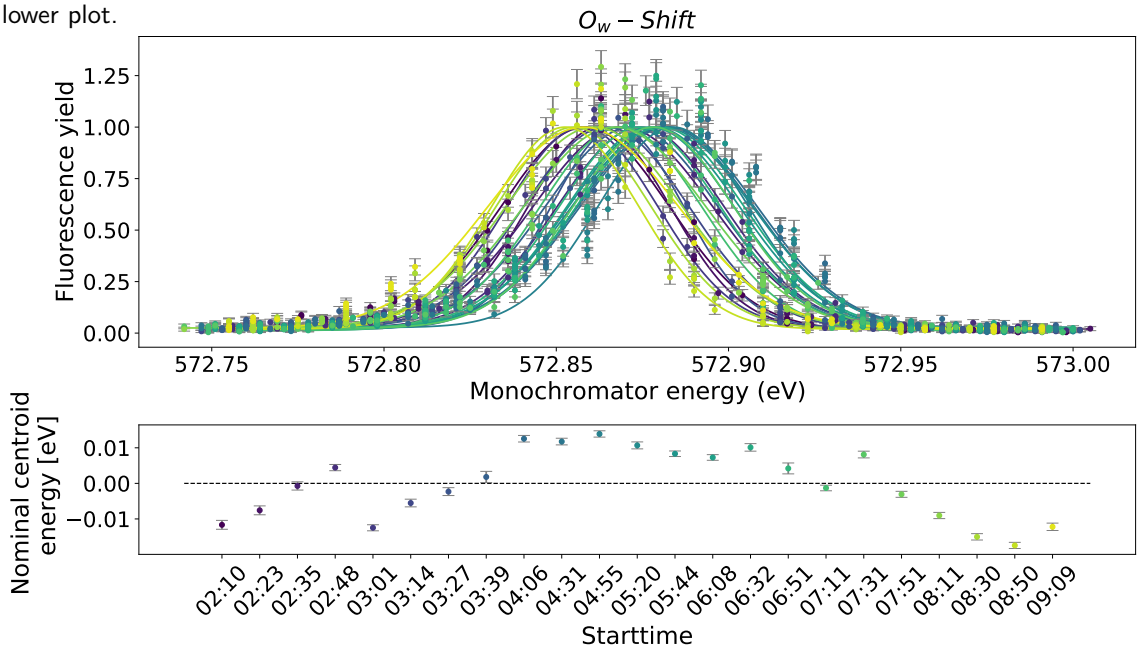

Figure 44: Estimation of the beamline shift with the help of the measurement of K_α transition of He-like oxygen (O_w). Over seven hours, 23 scans of 30 ToF each with t_{probe} 20 s measurement time were recorded and evaluated. The lower figure shows for each scan the difference of the centroid to the mean value.

A systematic drift can be detected, as the deviation of the centroids from the determined weighted mean value (linear fit with a fixed slope of zero) of $572.8700(21)\,\mathrm{eV}$ is significantly larger than the (statistical) error of the centroids. The drift of the beamline can be estimated upwards with $\Delta E_{\mathrm{Shift}} = 10\,\mathrm{meV}$. If systematic errors, such as encoder errors (see next chapter) are included, the true beamline drift is smaller. This value is used for the later evaluation as an estimate of the systematic error of the beamline shift.

5.5.2 Energy resolution

The aim of a scan is to determine the resonance energy as precisely as possible. In general, the higher the spectral resolution E/E_{FWHM} of a scan, the better a resonance can be fitted, since the minimum energy distance that can be resolved is smaller. As already mentioned in chapter 4.2 and 5.2, the energy resolution essentially depends on three things: the grating choice, which in turn depends on the photon energy, the slit size of the input and output slits of the monochromator, and the error of the angular encoder. Of course, the minimum adjustable energy distance of the monochromator also plays an important role (the smaller the better). To test the maximum possible resolution of the beamline, the O_w was used again by setting different output slit sizes. In all six scans shown, the mirror angle was fixed. In table 5, the size of the input and output slits of the monochromator, the nominal resolution energy and the gained resolution are listed.

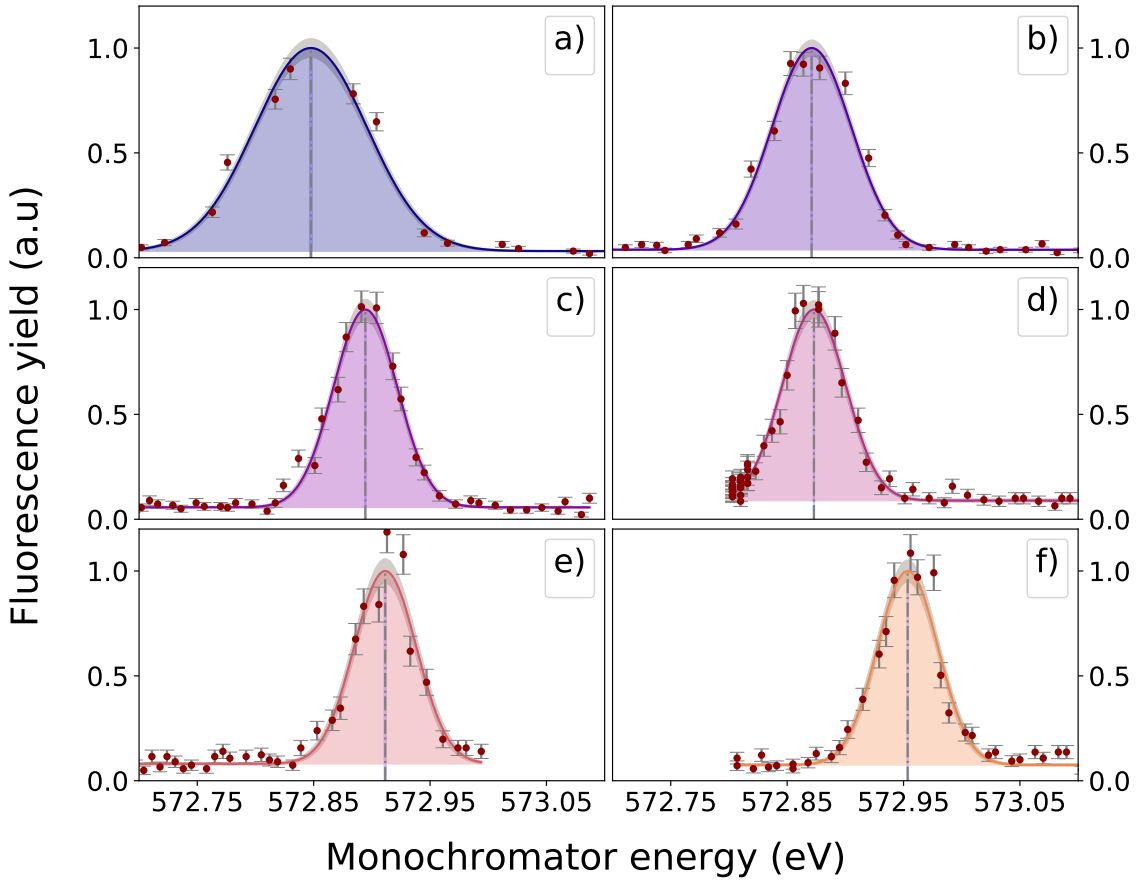

Figure 45: Determination of the maximum resolving power of the beamline. For six scans, the K_α-line of He-like oxygen (O_w) was measured, using different input and output slit sizes. The mirror angle was fixed in all cases. The results can be found in table 5.

In fig. 45 it can be seen very clearly that the scans did not all perform the same energy steps. On the one

hand, this is because the energy range and the number of steps were chosen differently, but also because the motor commands for changing the grating angle were not all accepted correctly. For example, in scan d), it can be seen that the first measuring points almost all have the same energy value. This shows the inaccuracy of the motors mentioned in chapter 5.2 and confirms the necessity of introducing the "precisionscan". The signal shape is insignificantly different for all scans.

Table 5: Overview of the dependency of the resolution of the O_w resonance on the input and output frequency as well as the (fixed) mirror angle).

Line	Entrance Slit[μm]	Exit Slit[μm]	E_{nominal}	Mirror angle [°]	$E/\Delta E_{FWHM}$
$O_w^{6+}(a)$	30	30	$572.848(2)$	19.1532	$5022(142)$
$O_w^{6+}(b)$	30	20	$572.871(1)$	19.1533	$7113(174)$
$O_w^{6+}(c)$	30	10	$572.894(1)$	19.1532	$8849(318)$
$O_w^{6+}(d)$	20	10	$572.873(1)$	19.1529	$8929(273)$
$O_w^{6+}(e)$	10	10	$572.911(1)$	19.1531	$9101(442)$
$O_w^{6+}(f)$	20	10	$572.954(1)$	19.2199	$9327(396)$

This series of measurements confirms that a resolution of more than 4000 can be achieved with a fixed mirror measurement scheme as has been stated by [6]. Furthermore, the maximum resolution found of over 9000 at $\approx 573\,\mathrm{eV}$ supports the upper limit of $10\,000$ (see chapter 4.2) at $540\,\mathrm{eV}$.
As expected, the largest influence on the resolution is given by the output slit size. The smaller this is chosen, the higher the resolution. A smaller input slit also improves the resolution, although the effect is smaller. It can also be seen that the nominal energy is strongly dependent on the input and output slit, which is why the slit sizes are not allowed to be changed during an energy calibration. During the scan, the mirror angle was fixed for all scans, but re-optimized before for the last one (f). This also leads to an improved resolution (despite a larger input slit than in f). This can be explained by the reduced defocusing effect (see 5.2). Although the mirror angle is fixed, the angle (and thus also the energy) varies by $0.003°$. This inaccuracy is part of the angular encoder error, which was mentioned in chapter 4.2 and reduces the resolution. The knowledge of both the encoder error and the defocusing effect is not only important for the energy resolution but also generates systematic errors which must be taken into account in an absolute energy calibration.

But not only a high resolution defines a good resonance determination, but also the quality of the projection values (signal-to-noise ratio, energy distance between the scan steps and errors of the projection values). Since the resolution is usually optimized at the expense of these values, a compromise of the necessary resolution, photon flux and measurement time t_{probe} have to be found. For example, if the output slit is reduced to improve the resolution, the photon flux decreases at the same t_{probe}, which worsens the signal to noise. The resolution can also be affected if the energy distance between the scan steps is too large. Therefore, in the rest of the work, only a resolution of $4000 - 6000$ is achieved.

It should be noted that the resolution is not completely influenced by the beamline. The fitting quality of the ToF in the case of the ion data also has an influence on the resolution, since especially in the case of weak signals, the ToF can be fitted more poorly, which leads to a deterioration of the resonance fit. Therefore, it is important to have a good fit model for ion data in order to fit it as precisely and consistently as possible.

5.6 Beamtime

A total of three measurement campaigns (beamtimes) were carried out at the synchrotron in Trieste. The evaluation of beamtimes I and II is limited to the absolute energy calibration of the astrophysically relevant K_α transition of Be-like oxygen $1s^2 2s^2 {}^1S_0 \rightarrow 1s2s^2 2p_{3/2} {}^1P_1$ at $554\,\mathrm{eV}$ (now $O^{4+}_{K_\alpha}$). The same transition is then used in Beamtime III to determine the isotope shift of O_{16} and O_{18}.

5.6.1 Beamtime I

$\mathbf{O^{4+}_{K_\alpha}}$ Data The excited state of $O^{4+}_{K_\alpha}$ can decay both via an autoionizing channel, which is detected by an increase of the Li-like oxygen yield, and via a radiative decay channel, which is detected in the fluorescence data. In fig. 46, both the projection signal of the SDD detector and the projection of the ion data are shown. Since only the low gain ToF signal was recorded during the first beamtime, the projection can only be determined using the gaussian method (see section 5.4.4). The peaks belonging to O^{5+} (as O^{4+} was photoionized) were previously identified using a ToF calibration as in chapter 34. Both projections are fitted with a gaussian signal, whereby a linear baseline is also fitted for the ion data.

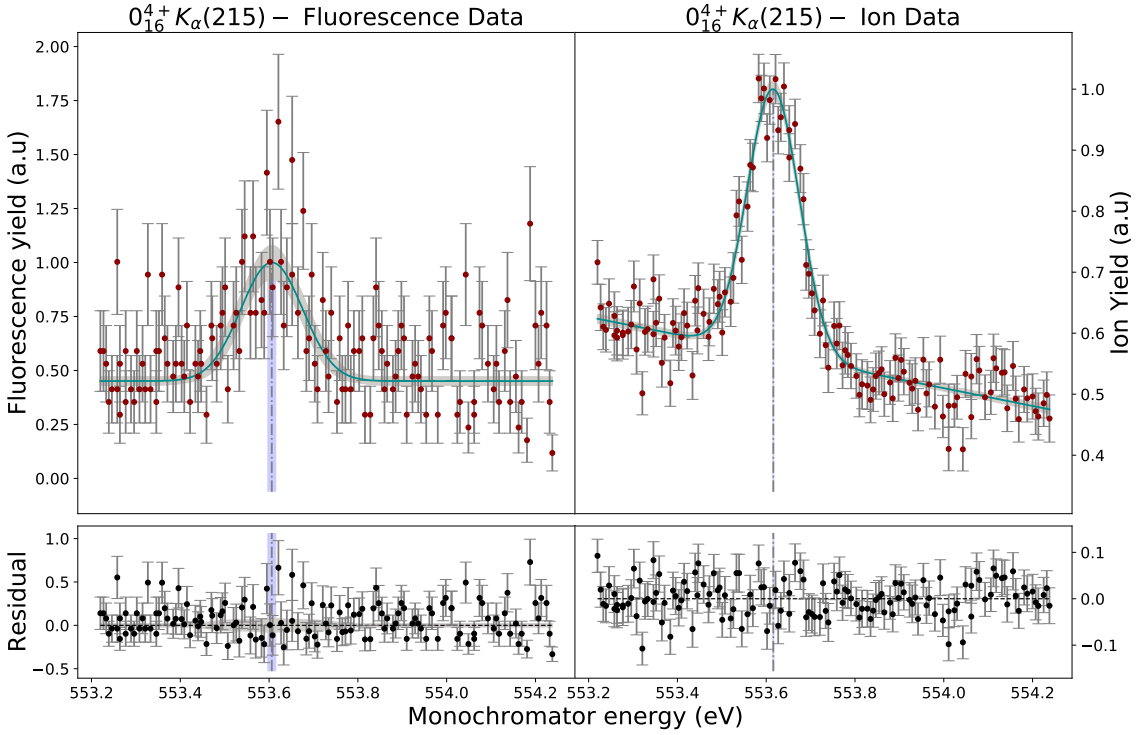

Figure 46: Comparison of the projected spectra of fluorescence (left) and ion data (right). In both cases, Be-like O^{4+} was photo-excited. On the left, the radiative decay channel is detected in the form of the fluorescence photons, on the right, the autoionizing channel is detected in the form of the ionized HCI.

It can be seen very clearly that the resonance signal in the ion data has a better signal to noise relative to the resonance in the fluorescence data. As expected, compared to the K_α transition of He-like oxygen,

the autoionization decay channel increases at lower charge state (see section 2.4.2). Therefore, for the following evaluation of this transition, only the ion signal for $O^{4+}_{K_\alpha}$ is analysed while the corresponding fluorescence spectra are neglected. Figure 47 shows the comparison of the ion yield spectra of the two scans taken in beamtime 1.

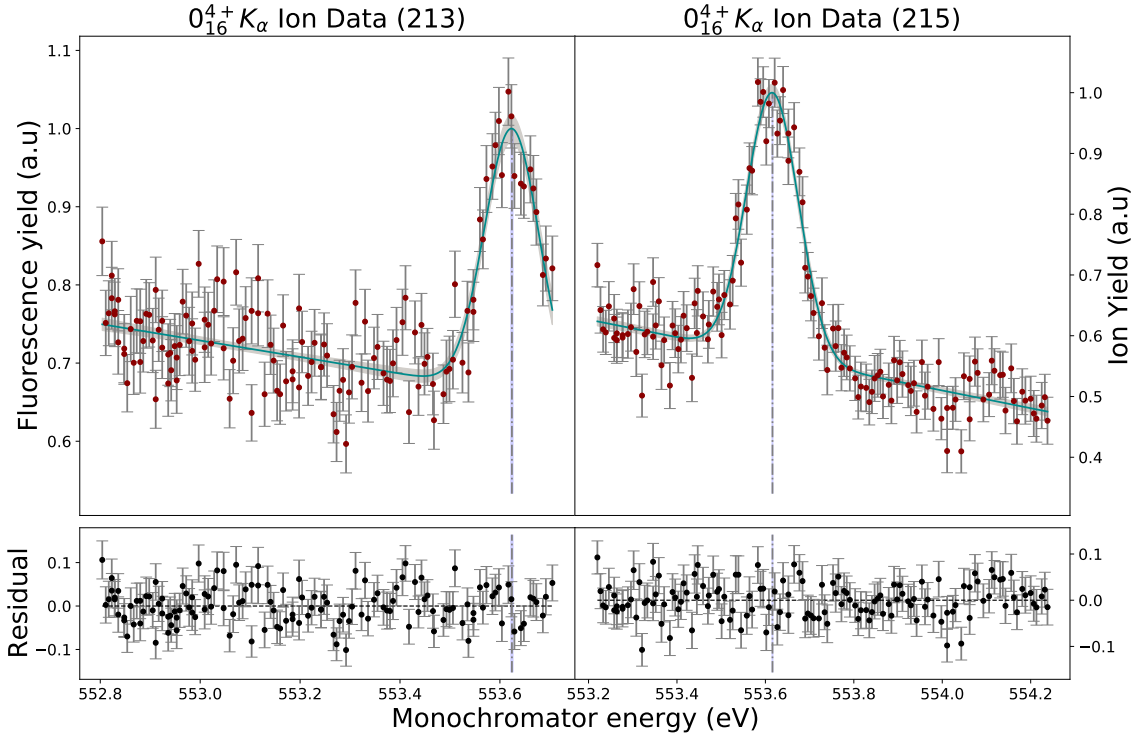

Figure 47: Comparison of the ion-yield spectra for two different scans for $O^{4+}_{K_\alpha}$ in BT1.

The resolution of the two scans are $4277(314)$ and $4001(154)$ respectively and confirms the assumption from chapter 4.2 that the resolution with fixed mirror angle can reach values above 4000.
All parameters belonging to these two scans can be found in table 6. The determined average nominal resonance energy

$$E_{O^{4+}_{K_\alpha},nom}(1s^2 2s^2 \rightarrow 1s2s^2 2p) = 553.618(4)\,\mathrm{eV} \tag{71}$$

provides the starting point for the calibration of the beamline and the absolute energy determination of $O^{4+}_{K_\alpha}$.

Calibration Since, as already mentioned in chapter 45 and 5.2, the nominal energy, which is determined from the two monochromator angles (mirror and grating angle), can deviate from the actual energy ($\approx 1\,\mathrm{eV}$), an absolute energy calibration is required (see 4.2). This difference is influenced both temporally by thermal expansion of the beamline components, but is also dependent on the settings of the beamline (input output slot, grating, etc) as well as the energetically fluctuating angle encoder error. Basically, it is assumed that the difference between nominal energy and actual energy is linearly correlated. For this

purpose, calibration lines of simple systems are used, where theory and experiment are in good agreement. $1s \rightarrow np$ transitions of He-like systems are very well suited for this purpose, since they can be calculated very well in theory [50].
During the calibration measurement, the monochromator is adjusted to the energy of the line to be calibrated. All beamline settings such as grating choice or slot sizes remain constant. The mirror angle is kept constant during the calibration measurement to obtain the highest possible resolution. As described in chapter 5.2, the energy distance between the calibration lines and the resonance energy of $O^{4+}_{K_\alpha}$ must not be too large, since otherwise artifacts resulting from the mismatched mirror and grating angle occur (defocusing effect).
Therefore, K_α $(1s^2 \rightarrow 1s2p)$ of He-like oxygen (O_w), K_ϵ $(1s^2 \rightarrow 1s5p_{3/2})$ and K_δ $(1s^2 \rightarrow 1s6p_{3/2})$ both of He-like nitrogen are chosen as lines, which are both close to the expected resonance energy of $554\,\mathrm{eV}$ and have a high excitation rates. As a further calibration line, the q/r line of Li-like oxygen was chosen $(1s^22s \rightarrow 1s2s2p)$. q/r are two separate resonance with excitation energies so close together that they cannot be resolved. In all transitions, which are used for calibration, the radiative decay channel dominates, so that only the fluorescence spectrum is used for the determination of the resonance.

During the first beamtime, two measurement series were performed, each measures all four calibration lines followed by one measurement of $O^{4+}_{K_\alpha}$ (see fig. 47). For all scans (calibration lines and $O^{4+}_{K_\alpha}$) the relevant scan parameters, as well as the the scan results, such as the nominal energy and the corresponding theoretical values (from table 3), are given in table 6.

Table 6: Overview of the calibration scans and $O^{4+}_{K_\alpha}$ scans: The four calibration lines measured in two measurement series $(*/**)$ are shown with their respective scan parameters, nominal energy and reference values (a:[18],e:[33] experimental),(b:[50], c:[58], d:[57] theoretical). The resolution was determined with E/E_{FWHM}.

Line	E_{Beam}[eV]	Scan range [eV]	ΔE_{Step} [meV]	t_{probe} [s]	E(This work)	E_{ref}	Res.
$O^{6+}_w(207)^*$	229	$572.513 - 573.026$	10.46	10	572.844(2)	$573.9614(5)^b$	4860(123)
$O^{6+}_w(217)^{**}$	229	$572.313 - 572.976$	19.5	20	572.850(1)	"	4918(103)
$O^{5+}_{q,r}(206)^*$	229	$561.97 - 563.29$	13.33	10	562.122(2)	$563.110(2)^c$	4440(116)
$O^{5+}_{q,r}(216)^{**}$	229	$561.576 - 562.498$	38.42	20	562.159(3)	"	4390(224)
$N^{5+}_{K_\epsilon}(197)^*$	229	$537.408 - 537.958$	11.22	15	537.838(5)	$538.493(1)^d$	5862(752)
$N^{5+}_{K_\epsilon}(210)^{**}$	229	$537.649 - 538.193$	6.89	10	537.857(5)	"	6409(790)
$N^{5+}_{K_\delta}(194)^*$	229	$531.400 - 532.426$	13.86	10	531.778(4)	$532.529(1)^d$	5334(450)
$N^{5+}_{K_\delta}(208)^{**}$	229	$531.469 - 532.157$	14.04	10	531.815(4)	"	6555(674)
$O^{4+}_{K_\alpha}(213)$	109	$552.804 - 553.705$	6.72	50	553.624(3)	$554.144(7)^a$ $554.250(180)^e$	4277(314)
$O^{4+}_{K_\alpha}(215)$	109	$553.22 - 554.238$	7.59	50	553.616(2)	"	4001(154)

For all scans, a trap depth of $12\,\mathrm{eV}$ was chosen. The (nominal) electron beam energy $(U_{\mathrm{DT4}} - U_{\mathrm{Cath}})$ for the measurement of $O^{4+}_{K_\alpha}$ was lowered to below the ionization energy of Li-like oxygen $(113.87\,\mathrm{eV})$ to ensure that the ion signal was not contaminated by the ions produced by the EBIT. For the other calibration measurements, He-like oxygen and nitrogen were required, for which the electron beam energy of $229\,\mathrm{eV}$ was chosen to be above the ionization energies for He-like oxygen $138.12\,\mathrm{eV}$ and nitrogen $97.89\,\mathrm{eV}$, respectively. In order to detect as much signal as possible, both t_{probe} and the number of

steps were increased considerably in the ion data. The statistical inaccuracy of the determined centroid positions is between $1 - 5\,\mathrm{meV}$ which corresponds to a precision of less than 10 ppm in all cases. As with the $O^{4+}_{K_\alpha}$ scans, the calibration lines have a resolution of over 4000, which is also in line with the expectations of chapter 4.2 at fixed mirror angle. However, the calibration lines have slightly higher resolutions than those of $O^{4+}_{K_\alpha}$. This can be explained by the fact that that the projection values of the ion data used to determine the resonance of $O^{4+}_{K_\alpha}$ and the resolution were determined by Gaussian fits (see section 5.4.4), which may lead to additional inaccuracies.

For each scan, the resonance energy of the individual line is determined. To obtain an absolute energy calibration, theoretical values are assigned to the nominal resonance energies of the four calibration lines. The resulting calibration points can then be used for a linear fit. This assigns an absolute energy E_{theo} to each nominal energy (E_{exp}). In fig. 48, the calibration is carried out for one of the two calibration measurements.

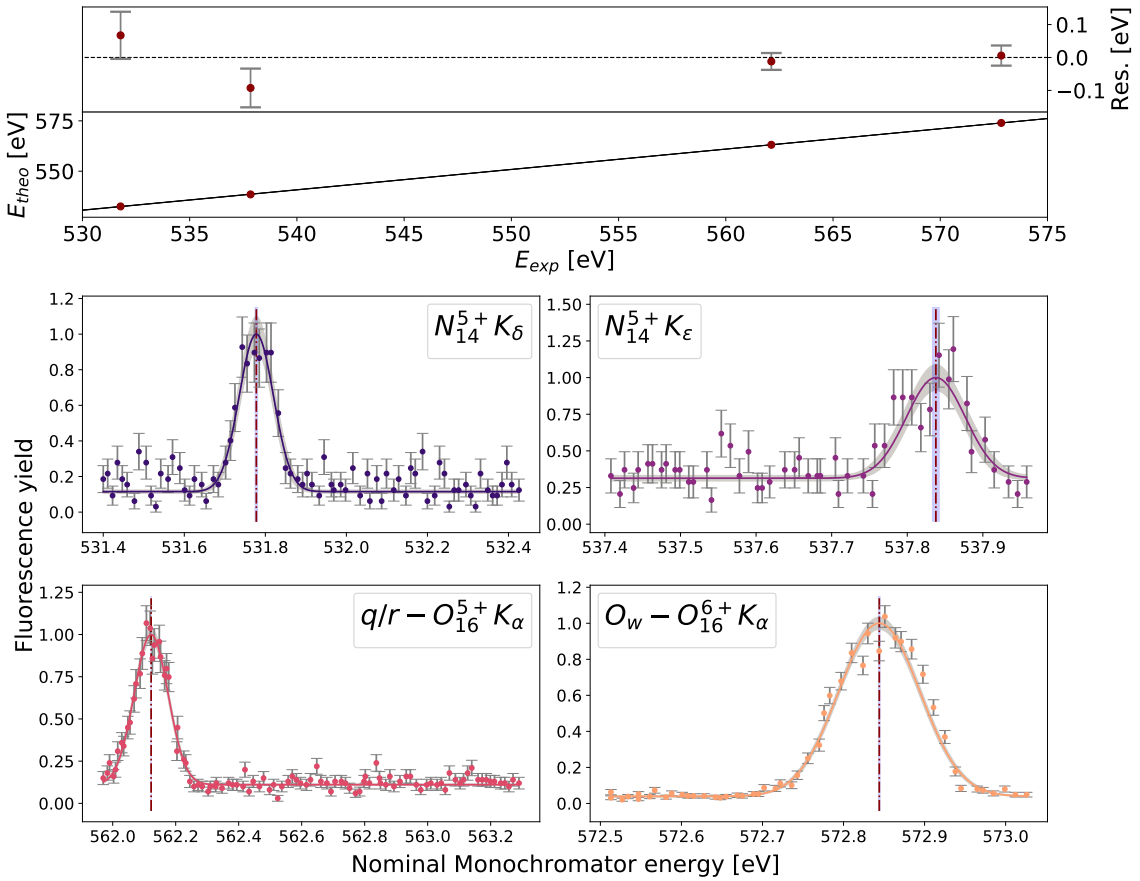

Figure 48: Energy calibration beamtime 1: By assigning the theoretically expected energies to the nominal energies of the four calibration lines (measurement series $*$), a calibration can be carried out with a linear fit. This assigns an absolute energy to each nominal energy.

The calibration is carried out once separately for both calibration measurements ($*/**$).
For measurement series $*$ and $**$ results a slope m and offset c of:

$$m^* = 0.9897(16) \quad c^* = 4.8(9)\,\mathrm{eV} \qquad m^{**} = 0.9888(16) \quad c^{**} = 5.3(9)\,\mathrm{eV} \tag{72}$$

Since the fit plot (E_{exp} versus E_{theo}) was tilted (E_{theo} versus E_{exp}) for clearer visualization, the E_{exp} error was converted to an E_{theo} error using the confidence band. Depending on the choice of calibration line, the nominal energy of $O^{4+}_{K_\alpha}$ (eq. 71) results in the following two values:

$$E_{O^{4+}_{K_\alpha}}(1s^2 2s^2 \rightarrow 1s2s^2 2p) = 554.530(32)\,\mathrm{eV}(*), 554.507(35)\,\mathrm{eV}(**) \tag{73}$$

The results for both calibrations are within their region of agreement. Compared to the two reference values Gu et al. 2005 ([18]) and McLaughlin et al. 2016 ([33]) the result lies outside their given values. However, it must be said that McLaughlin's result is in the 2σ range and in the result from this beamtime no systematic errors were taken into account. These errors influence the resonance determination of the calibration lines and thus also the result of the calibration.

As already mentioned, the energetic distance between nominal energy and actual energy can vary in time as well as in terms of energy. The angular encoder error, which arises due to the interpolation function, causes the energy difference between nominal and absolute energy to depend on the set energy. In addition, the return value of the encoders varies slightly when the angle is kept constant, which can be seen from the variation of the angle in table 5. The angular encoder error can be estimated up to $100\,\mathrm{meV}$. This error causes a degradation of the resolution with which the calibration lines can be measured, but also affects the linear calibration, since the calibration points no longer lie on a linear curve due to the energy-dependent error. More about this in the discussion. Another source for errors is the fact that the mirror angle is only optimally set to the resonance energy of $O^{4+}_{K_\alpha}$. This leads to defocussing effects in the calibration lines, which also have a negative effect on the calibration lines in terms of signal shape, resolution and energy determination. Nevertheless, the advantage of the fixed mirror angle outweighs the disadvantages. The systematic beamline shift also has to be taken into account. Since the time intervals of the beamline drift determination is comparable with the duration of the calibration measurement series, a drift estimation of $\Delta E_{\mathrm{Shift}} = 10\,\mathrm{meV}$ can be added as a systematical error.

5.6.2 Beamtime II

In order to better compare the result for the absolute energy calibration of beamtime 1 (BT1), an energy calibration of $O^{4+}_{K_\alpha}$ was also performed in beamtime II (BT2). However, a different approach has been chosen to calibrate the $\mathbf{O^{4+}_{K_\alpha}}$ line.

$\mathbf{O^{4+}_{K_\alpha}}$ Data As already shown in BT1, it is possible to determine the resonance energy for $O^{4+}_{K_\alpha}$ from both the fluorescence and ion signals. As in BT1, the autoionizing decay channel of $O^{4+}_{K_\alpha}$ is significantly stronger than the radiative one, which is why again only the ion data are analysed while the corresponding fluorescence spectra are neglected. A total of two scans of $O^{4+}_{K_\alpha}$ were taken, which are shown in fig. 49.

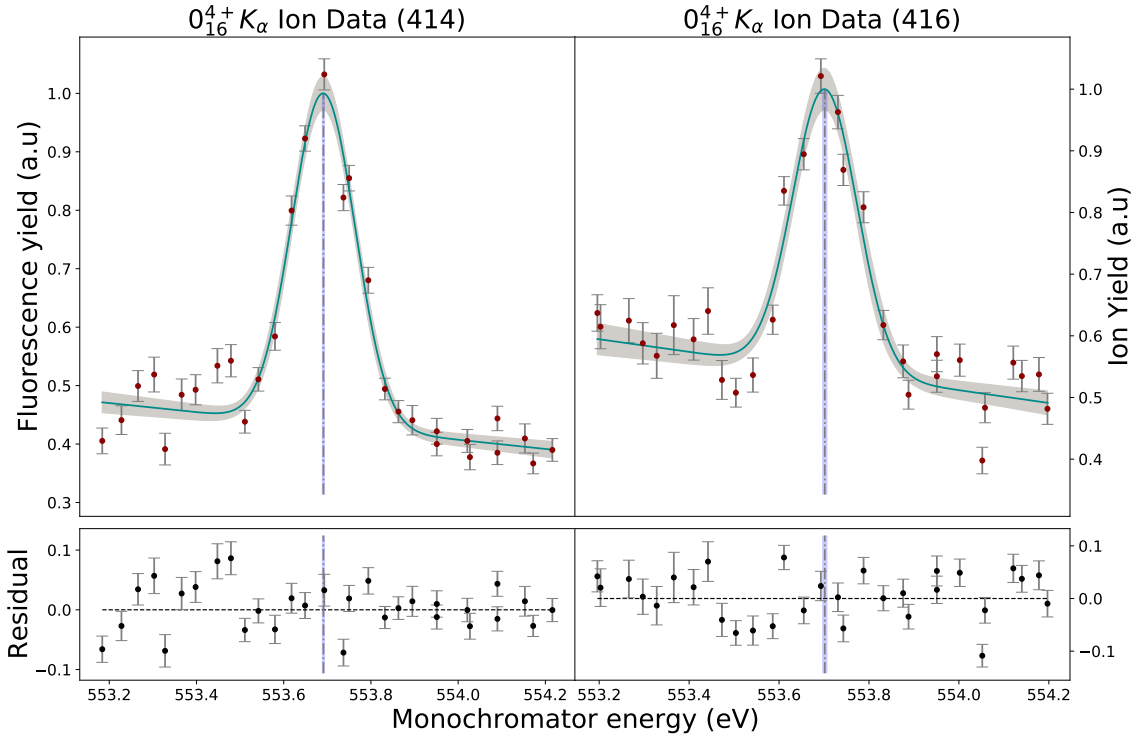

Figure 49: Comparison of the ion-yield spectra for two different scans for $O^{4+}_{K_\alpha}$ in BT2.

The resolution of the scans with $3237(189)$ and $3280(299)$ (scan data for both scan in table 7) is worse than in BT1. Explanation for this are the clearly shorter measuring time t_{probe} compared to the scans from BT1 (see table 7):

$$E_{O^{4+}_{K_\alpha},nom}(1s^2 2s^2 \rightarrow 1s2s^2 2p) = 553.694(5)\,\mathrm{eV} \tag{74}$$

To calibrate this nominal energy, an energy calibration must be carried out again. Since the nominal energy can change over time (see beamline shift section 5.5.1), a new calibration must be carried out.

In contrast to BT1, only two calibration lines are available in BT2. Since a linear fit with two degrees of freedom must be fitted with at least three datapoints for a meaningful result, it is assumed that the linear fraction of the assignment from nominal energy to actual energy has remained constant over the beamtimes. Only the constant offset of the assignment can change. This can be justified by the fact that the angular encoder can measure relative angle changes consistently, whereas the absolute angle offset is subject to fluctuations. Therefore, the slope for the calibration of BT2 is taken from that of BT1 from eq. 72. Since two calibrations could be performed in BT1 with two different slopes, two calibrations can be performed for the same calibration lines in BT2 but different fixed slope.

Again $K_\alpha(O_w)$ of He-like oxygen ($1s^2 \rightarrow 1s2p$) is chosen as a calibration line. This line was measured in two scans and the mean value was used as the calibration value (see fig. 51). Analogous to BT1, the reference value $E_{\text{theo}} = 573.9614(5)\,\text{eV}$ from Togawa et al. 2020 [50] is used.
As a second calibration line, a molecular transition of O_2 is used, where a $1s$ electron is excited into a π^* orbital. During the subsequent autoionization, the resulting Auger electrons are measured with an channeltron. This measurement does not take place inside the EBIT but in a gas cell upstream of the EBIT, which is continuously supplied with O_2 at a controlled pressure. The gas cell is located approximately $1\,\text{m}$ upstream from the EBIT (see also fig. 25). A molecular spectrum of the well known $1s - \pi^*$ vibronic transitions has been recorded (shown in fig. 50) to calibrate the $O^{4+}_{K_\alpha}$ transition. Due to its proximity to the $O^{4+}_{K_\alpha}$ line, the $1s - \pi^*$ transition is in principle well suited as a energy reference.

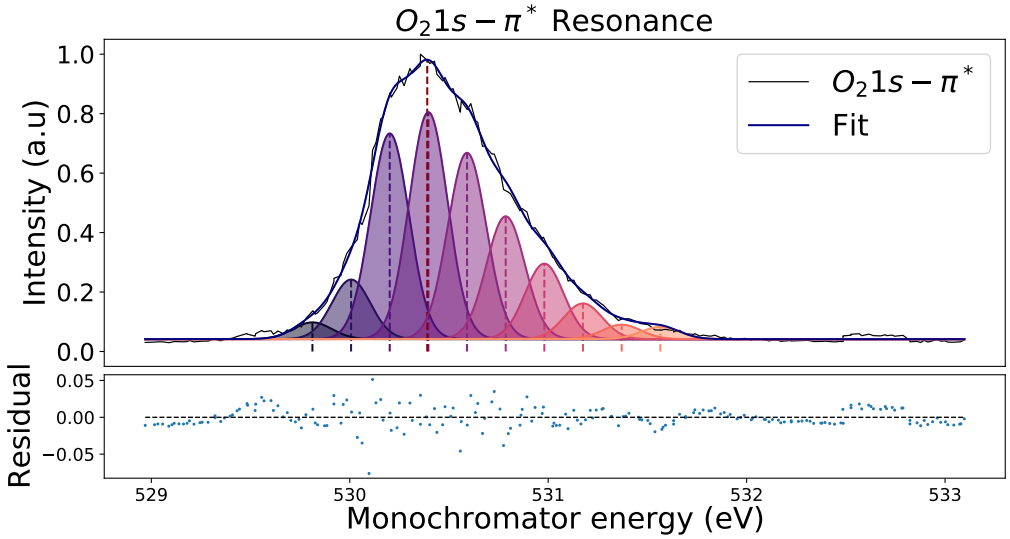

Figure 50: Resonance determination of the molecular excitation of O_2 in which a 1s electron is lifted into the π^* orbital. Ten equidistant Gaussians were fitted, which represent the vibrational spectrum. The maximum of the fit curve represents the resonance energy of $1s - \pi^*$.

To model the observed molecular spectrum, a sum of several equidistant gaussian profiles have been used for the vibrational components. Since the experimental resolution has not been sufficient to resolve the vibrational progression of the π^* level, the number of gaussian profiles has been tuned for the best χ^2_{red} result of the least-squares fitting procedure. Furthermore, the determined vibrational-distance of $195\,\text{meV}$, which corresponds to the vibrational constant ω_e, is comparable to the value $\omega_e = 138.4(3)\,\text{meV}$

determined by Coreno et al. 1999 [9], however in clear disagreement. We determine the maximum of the molecular spectrum as

$$E(1s \rightarrow \pi^*) = 530.39(5)\,\mathrm{eV} \tag{75}$$

Since the fit quality is strongly influenced by the choice of the number of Gaussians used, the error is estimated to be one quarter of the determined vibrational constant. The discrepancy with the experimental reference value $E_{ref}(1s - \pi^*) = 530.8(2)\,\mathrm{eV}$ of Wight et al. 1974 [56] shows the necessity of calibration. In table 7 all scans necessary for the calibration with the relevant scan parameters, nominal as well as reference energies are listed. The statistical inaccuracy of the determined centroid positions is between $4 - 6\,\mathrm{meV}$ which corresponds to a precision of less than 10 ppm in all cases. The O_w, which is used as a second datapoint for the calibration curve, is again modelled by a gaussian profile (see fig. 51).

Table 7: Overview of the calibration scans for BT2: Beside the calibration line $O^{4+}_{K_\alpha}$ (two scans), the relevant scan parameters, resolution as well as nominal and reference energies (a:[18],c:[56] d:[33] experimental), (b:[50] theoretical) are given for the two calibration lines $K_\alpha(O_{w)}$ of He-like oxygen and the molecular transition of $1s - \pi^*$.

Line	E_{Beam}[eV]	Scan range [eV]	ΔE_{Step} [meV]	t_{probe} [s]	E_{nominal}	E_{theo}	Res.
$O^{6+}_w(413)$	194.7	$572.594 - 573.619$	35.35	10	573.120(5)	$573.9614(5)^b$	3242(161)
$O^{6+}_w(415)$	194.7	$572.594 - 573.619$	35.35	10	573.103(5)	"	3088(133)
$O_2(424)$	-	$528.969 - 533.097$	20.74	15	530.39(5)	$530.8(2)^c$	6555(674)
$O^{4+}_{K_\alpha}(414)$	108.4	$553.184 - 554.216$	35.59	20	553.691(4)	$554.144(7)^a$ $554.250(180)^d$	3237(189)
$O^{4+}_{K_\alpha}(416)$	108.4	$553.196 - 554.197$	34.52	20	553.702(6)	"	3280(299)

If one assigns to the two nominal energies of the calibration lines their reference values from the table 7 and fits the resulting calibration points with a linear fit, one obtains the energy calibration in fig. 51. The slope was taken from the measurement series $*$. This assigns an absolute energy E_{exp} to each nominal energy (E_{theo}). Depending on the measurement series from BT1 from which the slope was taken (see eq. 72), the result for the fitted offset and the calibrated energy for eq. 74 differ.

For the offset of the two calibrations results $c^* = 5.0615(6)\,\mathrm{eV}$ and $c^{**} = 5.577(7)\,\mathrm{eV}$ respectively. If the nominal energy eq. 74 is calibrated with these, the result is:

$$E_{O^{4+}_{K_\alpha}}(1s^2 2s^2 \rightarrow 1s 2s^2 2p) = 554.343(4)\,\mathrm{eV}, 554.326(8)\,\mathrm{eV}. \tag{76}$$

where the first energy correspond to the fit with slope from measurement series $*$ and the second to the fit slope from measurement series $**$.

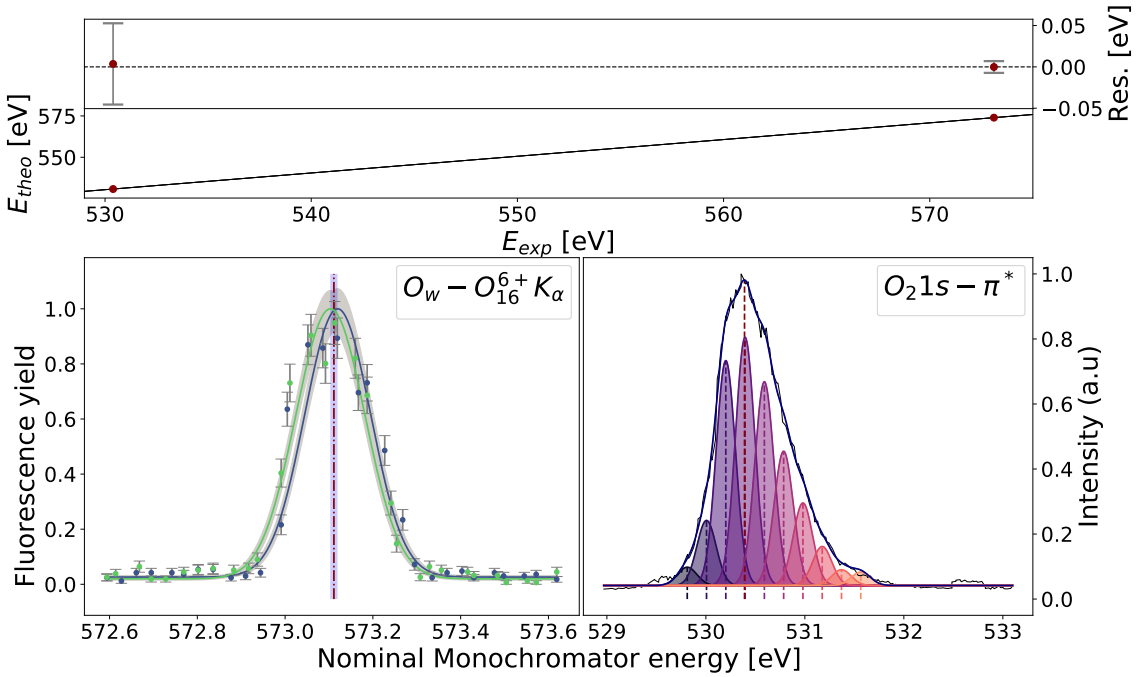

Figure 51: Energy calibration BT2: By assigning the theoretically expected energies to the nominal energies of the two calibration lines O_w and $1s - \pi^*$, a calibration can be carried out with a linear fit. Since only two calibration lines are available, only the offset of the linear line is fitted while the slope is adopted from BT1. In the calibration shown, the slope from measurement series $*$ was used.

The systematic errors mentioned in the context of BT1, such as the encoder interpolation error of the angular encoder, defocusing effects of the synchrotron radiation, but also the beamline shift, must be taken into account. The results of BT2 for the absolute energy for $O_{K_\alpha}^{4+}$, like that of BT1, lies outside the experimentally determined reference value of Gu et al. 2005 [18]. In contrast to BT1, both result is in agreement with the experimentally determined reference by McLaughlin et al. 2016 [33].

However, this result should be seen with a reservation, as the assumption of the constant slope from BT2 can be questioned. The O_w energies determined in BT2 are systematically larger than in BT1 (compare table 6, 7) with an energy difference of more than $0.3\,\mathrm{eV}$. Although the energy for $O_{K_\alpha}^{4+}$ is also higher in BT2 than in BT1, the energy difference is only $0.076\,\mathrm{eV}$. This argue both against the assumption that there is only a constant offset between calibrations. Either it has to be assumed that the slope of the calibration also changes or other systematic effects that have taken place between the two beamtimes have to be taken into account. To address this discrepancies, a calibration with more datapoints would have been required. More on that in the discussion.

5.6.3 Beamtime III

Besides the absolute energy calibration of K_α of Be-like oxygen ($O^{4+}_{K_\alpha}$) in BT1 and BT2, the aim of the third beamtime (BT3) was to measure the isotope shift of O_{16} and O_{18} of the same transition. The goal is to determine the resonance energies of $O^{4+}_{K_\alpha}$ for both isotopes (now always O^{4+}_{16},O^{4+}_{18}) whose difference is just the isotope shift. To measure the isotope shift, the resonances of O_{16} and O_{18} must be resolved from each other for each scan step (respectively for each energy). This can only be done in the ion data, as the two fluorescence photons cannot be distinguished in the fluorescence data. The resolution of the SDD with ($FWHM \approx 60\,\mathrm{eV}$, see section 3.6.1) is too low compared to the expected isotope shift calculated with FAC ($\approx 1.9\,\mathrm{meV}$, see table 3). In contrast to this, in the ion data, the Li-like oxygen O^{5+} HCI formed during photoionization of Be-like oxygen O^{4+} can be distinguished by their different q/m ratio ($5/16$ to $5/18$).

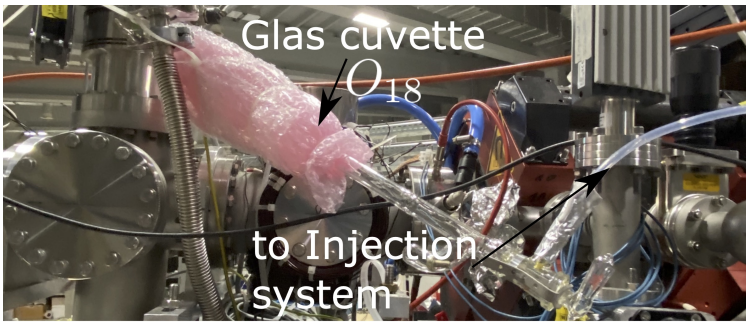

Figure 52: Injection of O_{18} into the EBIT. This is necessary to detect O_{18} in the ion data.

To be able to measure the resonance energy of the photoionization of O_{18}, the relative amount of O_{18} has to be increased. Therefore, almost pure O_{18} from a gas cuvette has to be injected into the EBIT trap chamber. In fig. 52, the external O_{18} glass cuvette is shown which is connected to the injection system of the EBIT.

Data As already described, a ToF calibration have to take place to assign a q/m to each ToF. For this set of data used in BT3, the energy calibration has already taken place, since the exemplary data presented in chapter 5.4 refer to data which have just been taken from BT3. i.e., fig. 34 corresponds to the ToF calibration for the whole measurement series, which was taken in BT3. All labels from chapter 5.4 can also be transferred. A new calibration is therefore not necessary.
In order to determine the resonance energy for O^{4+}_{16} and O^{4+}_{18}, the fit model is applied to each ToF spectrum. Since the model is used for the projection, each of the two ToF peaks (isotopes) is split to a main peak, which is modelled by a Gaussian, and a ringdown part. The area of both is proportional to the incident number of ions. In fig. 53, the projection formation for the gaussian and ringdown signal of both peaks belonging to one scan is shown. The upper plot shows the model fit for a specific ToF spectrum (a), where the projection values are graphically represented by the colored areas. The model fit has been repeated analogously for all monochromator steps and by plotting the area of the Gaussian and ringdowns for each monochromator step, two one-dimensional spectra per isotope can be produced (b-e). Using a Gaussian fit to fit these spectra, O^{4+}_{16} and O^{4+}_{18} can be determined. The projection values determined from (a) are marked in orange. All projections are shown together in d). As mentioned in section 5.4.4, the parameters for the constant ToF peaks, which do not depend on energy, were kept constant in the model fit.

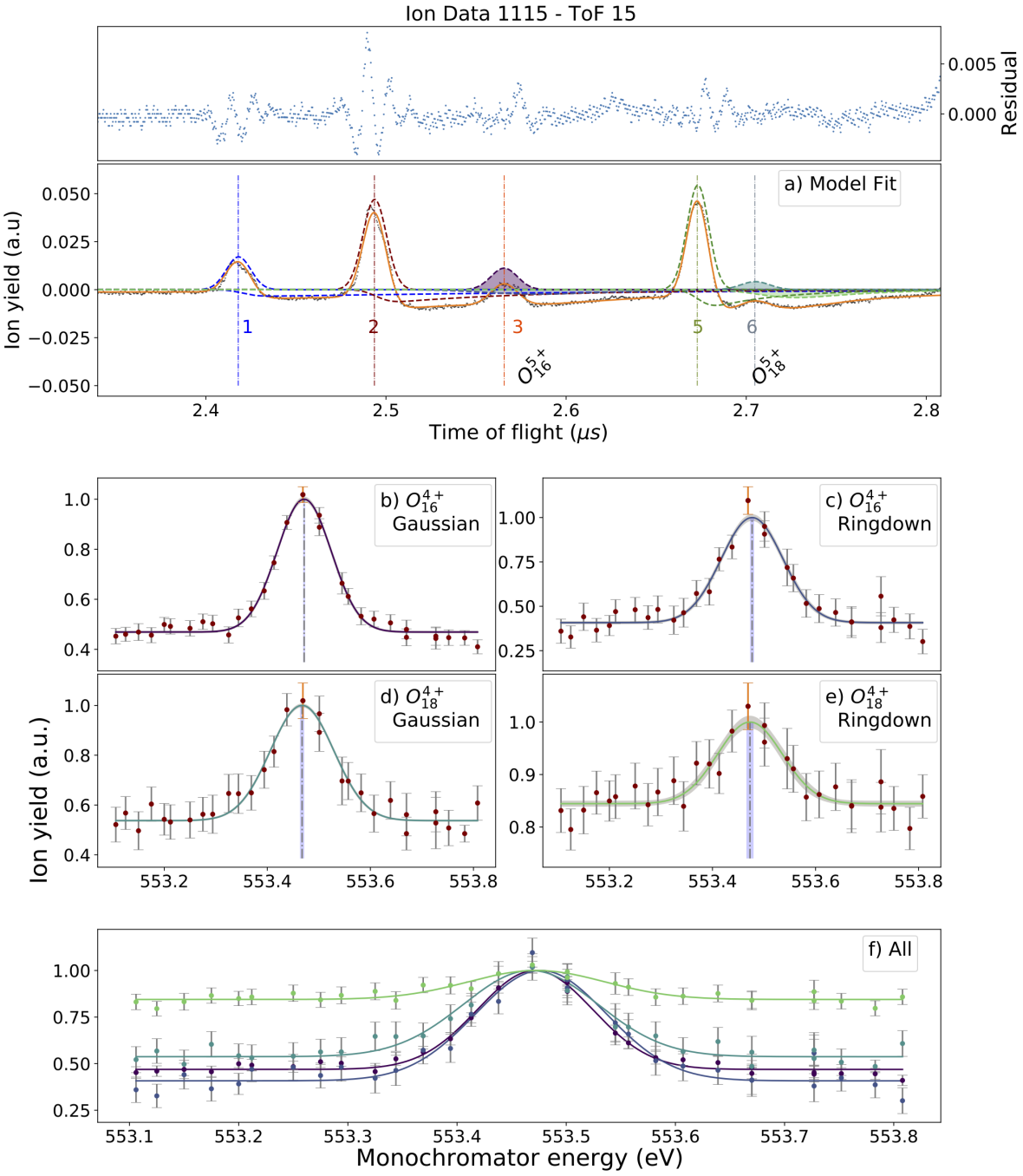

Figure 53: Projection and resonance determination of $O_{K_\alpha}^{4+}$ from O_{16} and O_{18}. a) The signal model is applied to a ToF-spectrum of an arbitrary monochromator step. The gaussian and ringdown signal produced by the ToF-peaks 3 and 5 can be used individually for a projection. These, in total four projections, are plotted in figure b, c d and e. In the upper plot, the model fit for a selected ToF is formed (a), where the color-coded areas represented the respective projection value. The middle part presents the four fitted projections (b-e). The four spectra are overlapped in f) to compare the varying Signal to Noise ratios.

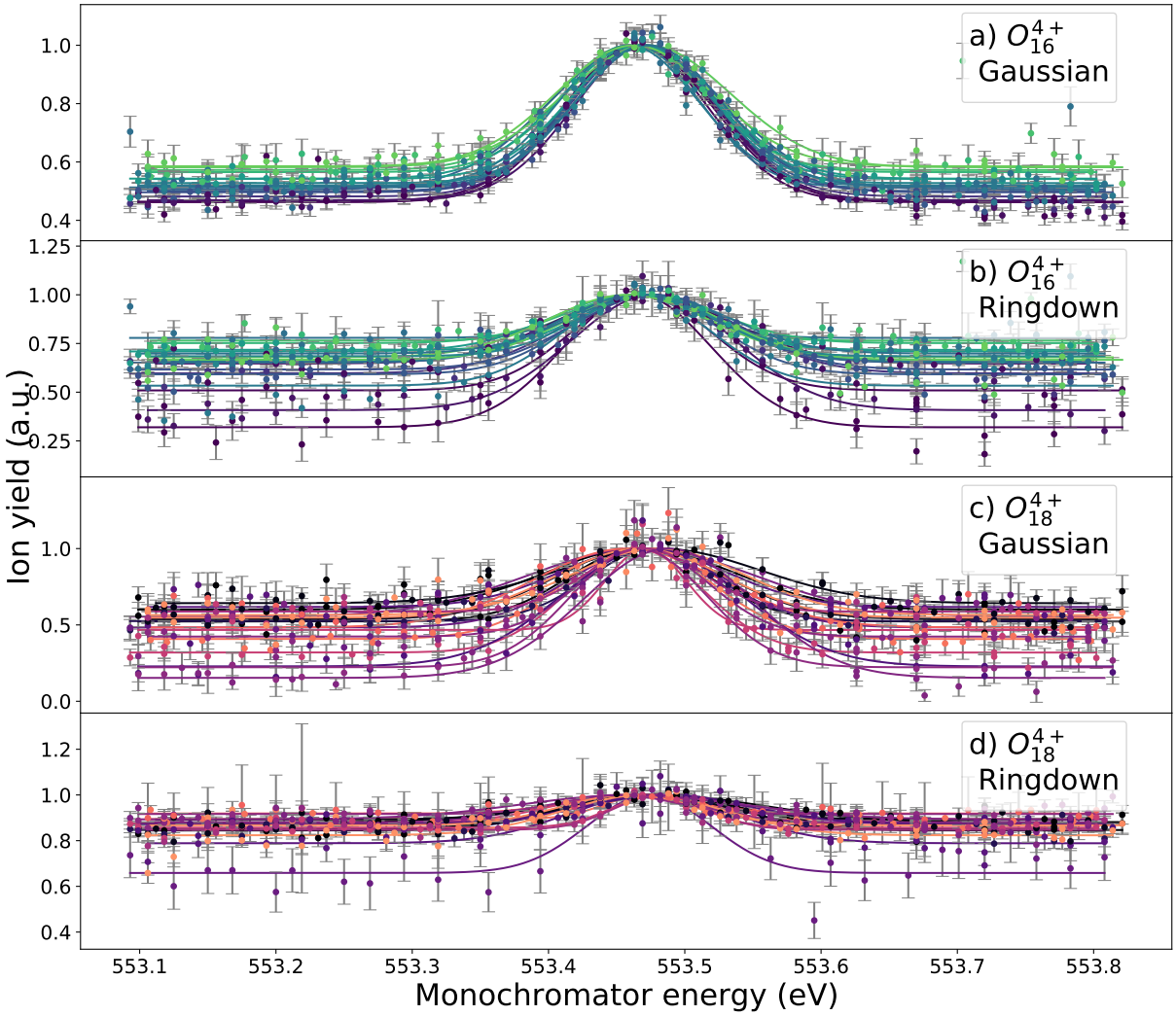

Figure 54: Projection overview of gaussian (a, c) as for ringdown signals (b,d) for O_{16} and O_{18} for 18 scans. Each projection value for a scan and HCI (green/red) was marked accordingly. With the help of the obtained centroid energies, the isotope shift can be determined.

The four spectra, which can be extracted from every scan, are plotted in fig. 54. In total, 18 spectra have been recorded for the determination of the isotope shift. For comparison purposes, the mean single resonance energy error, the weighted mean values of resolution $E/\Delta E_{FWHM}$ and signal to noise (SNR) are compared in table 8:

Table 8: Comparison of mean single resonance energy error ΔE_{single}, energy resolution $E/\Delta E_{FWHM}$ and signal to noise ratio SNR of all projections are shown in fig. 54.

	O_{16}^{4+} Gauss	O_{16}^{4+} Ringdown	O_{18}^{4+} Gauss	O_{18}^{4+} Ringdown
ΔE_{single} [meV]	2.6	6.0	5.9	8.7
$E/\Delta E_{FWHM}$	4300(67)	4113(86)	4116(171)	3916(216)
SNR	1.910(33)	1.443(39)	1.883(90)	1.144(7)

The resolution also confirms the advantage of the fixed mirror angle, as otherwise resolutions of over 4000 are not possible.
When all three parameters are compared in the table 8 and in fig. 54, one can observe that the projection quality of the photoionization signal of O_{16}^{4+} is slightly better than that of O_{18}^{4+}. This can be explained by the fact that the O_{16}^{4+} ion yield is larger than the O_{18} yield. Moreover, the O_{16}^{4+} peak in the ToF spectrum is more isolated than the O_{18}^{4+} peak, which leads to a better fit quality and thus a better projection quality.
At the same time, it is noticeable that there is a difference in quality between the Gaussian and ringdown signals. The reason for this is that the Gaussian signals of the respective peaks are much better to fit than the ringdown signal, because the Gaussian signals are more isolated than the ringdown signals, which strongly influence each other. Despite the differences between Gaussian and ringdown signals, the advantage is that two resonance energies can be determined per ion and scan. Thus, the model fitting method has a statistical advantage (compared to the Gaussian method (see section 5.4.4).

Isotope shift

The isotope shift is the difference between the resonance energies of the K_α transition of the two isotopes O_{16} and O_{18}. There are two methods to determine this.
Each scan from fig. 54 produces two resonance energies for both isotopes, one determined via the Gaussian and one via the ringdown signal. The resonance energies of the Gaussian and the ringdown of an isotope are expected to be the same (they originate from the same peak in the ToF spectrum). Therefore, one way to determine the isotope shift is to first form the resonance energies of the two isotopes, using both Gaussian and ringdown of an isotope each time. The two resulting resonance energies are then subtracted from each other to obtain the isotope shift (method 1). The other method works the other way round. Here, the energy difference between the two isotopes is first formed, i.e. the resonance energy that was determined for one isotope via the Gaussian signal is subtracted from the resonance energy of the other isotope, which was also determined via the Gaussian signal. An analogous process will be conducted for the ringdown resonance energies. The isotope shift is then determined from from all determined energy differences (method 2).

In principle, the isotope shift determined from nominal energies O_{16}^{4+}, O_{18}^{4+} does not need to be calibrated, since a good relative energy calibration between the two nominal resonance energies is assumed and the calibration becomes obsolete due to the difference. There are also two possibilities to determine the isotope shift from the individual resonance energies in method 1 and the energy differences in method 2.

Histogram For method 1, a histogram is produced from all resonance energy values of O_{16} and O_{18} (see in the left and middle plot of fig. 55). The centroid of the normal distribution is obtained by a least square fit of a gaussian profile. Subtracting the two centroid values the isotope shift

$$\left.\begin{aligned} E_{O_{16}^{4+}} &= 553.4677(13)\,\mathrm{eV} \\ E_{O_{18}^{4+}} &= 553.4705(12)\,\mathrm{eV} \end{aligned}\right\} \quad \Delta E_{\mathrm{Shift}} = 3.9 \pm 1.8\,\mathrm{meV}(E_{O_{18}} - E_{O_{16}}) \tag{77}$$

is obtained. For method 2, a histogram is produced from all energy difference values of O_{16} and O_{18} (see in the right plot of fig. 55). The centroid of the normal distribution is again obtained by a least square fit of a gaussian profile. Thus, via method 2, one directly obtains the isotope shift of

$$\Delta E_{\mathrm{Shift}} = 2.6 \pm 1.8 meV \tag{78}$$

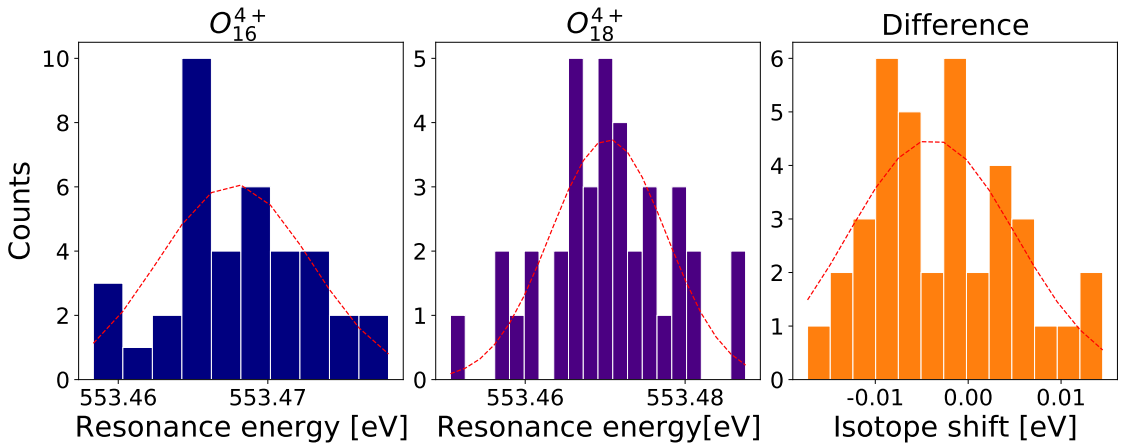

Figure 55: Determination of the isotope shift with method 1 and 2 via the formation of a histogram. Thereby, the resonance energies for $O_{K_\alpha}^{4+}$ are determined from O_{16} (left) and O_{18} (centre), from which the shift is determined with method 1. The histogram on the right shows the energy differences, from which the isotope shift can be determined directly with method 2.

Weighted average Instead of a histogram, a weighted average value can also be used to determine both the corresponding resonance energies in method 1 and the isotope shift in method 2. The weighted mean takes into account the statistical error of each fit of the resonance energies.
Therefore, in fig. 56 for method 1, the two resonance energies O_{16}^{4+} and O_{18}^{4+} are determined by a weighted average value, using for each of the two isotopes all determined resonance energies from Gaussian (blue) and ringdown (red) projections. It is clearly recognisable that the ringdown signals have a significantly larger variance, which which is in accordance with the discussion in table 8.
By subtracting the two resonance energy values for O_{16} an O_{18} the isotope shift is determined as

$$\left.\begin{aligned} E_{O_{16}^{4+}} &= 553.4681(7)\,\mathrm{eV} \\ E_{O_{18}^{4+}} &= 553.4696(10)\,\mathrm{eV} \end{aligned}\right\} \quad \Delta E_{\mathrm{Shift}} = 1.5 \pm 1.2\,\mathrm{meV}(E_{0_{18}} - E_{0_{16}}) \tag{79}$$

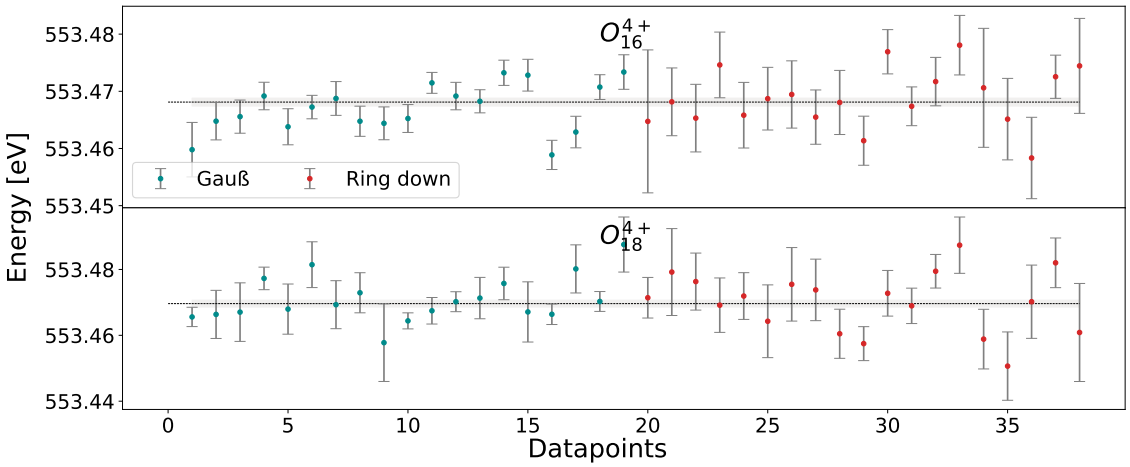

Figure 56: Method 1: Determination of the resonance energy of $O_{K_\alpha}^{4+}$ from O_{16} and O_{18} via a weighted mean (linear fit with slope zero). For this, both the corresponding resonances determined via the Gaussian (blue) and ringdown data (red) are used. The error of the mean is shown in the grey band. Their difference is the isotopic shift of O_{16}/O_{18} (method 1).

The weighted average can also be used with method 2 to directly determine the isotope shift from the differences of the corresponding Gaussian/Gaussian or ringdown/ringdown energies of the two isotopes. In fig. 57, the weighted mean value for the differences are shown, where again the differences of the Gaussian signals are shown in blue and those of the ringdown signals in red.

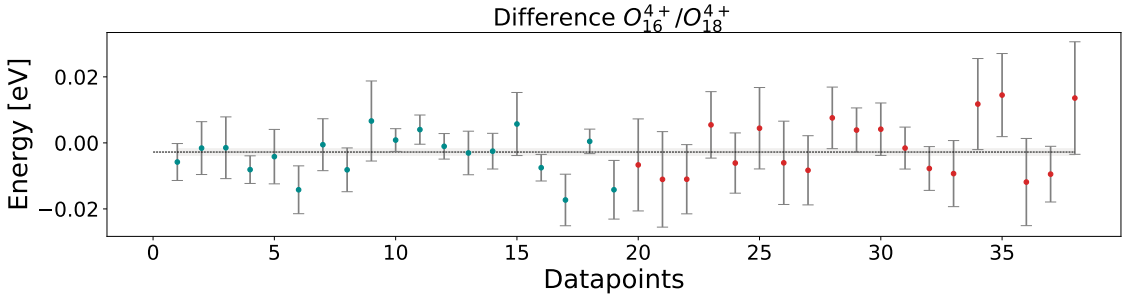

Figure 57: Isotope shift O_{16}/O_{18} is determined directly via the difference of the corresponding energies gaussian/gaussian (blue) and ringdown/ringdown (red) of both isotopes with a weighted mean value. The error of the mean value is shown in the grey band.

From the weighted average, which has been carried out in fig. 57, the isotope shift is given as

$$\Delta E_{\mathrm{Shift}} = 2.8 \pm 1.0\,\mathrm{meV} \tag{80}$$

6 Discussion and Outlook

The aim of this work was to investigate the transition of the K_α-line of Be-like oxygen O^{4+} at $554\,\mathrm{eV}$ by resonant excitation with soft X-ray synchrotron radiation. Since the excited state of this transition decays mainly by autoionization, photoionization is observed when resonance excitation with photons has previously occurred. The PolarX electron beam ion trap was used to generate and trap highly charged ions, which were then excited with synchrotron radiation from the Elettra synchrotron in Trieste, Italy. The EBIT can measure, both radiative decay channels and autoionizing decay channels and is capable of controlling the maximum available charge state of an element. With the help of a time-of-flight measurement, the charge state distribution within the EBIT can be detected. This determination of the charge state of ions, can be used to analyze photoionization processes. Since ions can be distinguished not only by different charge states but also by their masses, it is possible to measure the change in a transition energy due to the isotope shift. In addition to searching for an isotope shift of O_{16}/O_{18} in the photoionization from the K_α transition of Be-like oxygen, the absolute energy for this transition is determined.

Energy calibration The first part of the analysis focused on the absolute energy calibration of $O^{4+}_{K_\alpha}$. In each of the two beamtimes, two of these transitions were detected in the ion signal and a mean nominal resonance energy was determined. To identify the correct HCI peak in the ion signal, a time-of-flight calibration had to be performed previously, which assigned a q/m ratio to each ToF.
Theoretically well known and lines like K_α of He-like oxygen (O_w), K_ϵ and K_δ, both of He-like nitrogen, were chosen as calibration lines in beamtime 1 (BT1), being energetically close to the expected resonance energy of $554\,\mathrm{eV}$ and showing a high excitation rate. In contrast to the line of Be-like oxygen detected in the ion data, all calibration lines were detected in the fluorescence spectrum. In beamtime 2 (BT2), only two calibration lines were measured, namely K_α of He-like oxygen as well as the molecular excitation of O_2 ($1s - \pi^*$). This measurement was carried out upstream in a gas chamber, and the Auger electrons resulting from autoionization were measured. All calibration lines except the one of the molecular O_2 could be determined with a precision of more than 10ppm.
Since all calibration lines were measured twice in beamtime 1 (BT1), two independent calibrations could be performed there. For the calibration fit in BT2 it has to be taken into account that one calibration parameter had to be fixed as only two calibration points were available. For a complete fit of a linear function at least three data points are needed. Only the constant offset between nominal energy and absolute energy was fitted, taking the slope from the calibration of BT1. This choice was justified by the assumption that the angular encoder can measure relative angle changes precisely, while the absolute offset of the angle determination is subject to fluctuations. The two calibration lines for BT2 were measured only once, but were fitted with two different slopes from BT1.

Table 9: Comparison of the nominal and absolute resonant energies of $O^{4+}_{K_\alpha}$ determined from both beamtimes with the experimental reference energies: a) Gu et al. [18] and b) McLaughin et al. [33].

Beamtime	$E_{\mathrm{nominal}}[eV]$	$E_{\mathrm{calib}}[eV]$	$E_{\mathrm{ref}}[eV]$
1	553.618(4)	554.507(35)	
		554.530(32)	$554.144(7)^a$
2	553.694(5)	554.343(4)	$554.250(180)^b$
		554.326(8)	

In table 9 a comparison of the reference lines (Gu et al. 2005 [18] and McLaughin et al. 2016 [33]) with the nominal and calibrated resonance energies for the two beamtimes is shown.
First, the energy difference between the nominal energy and absolute energy of $0.6 - 0.9\,\mathrm{eV}$ makes an energy calibration inevitable. Also notable is the large error of the reference by McLaughin et al. This can be explained by a different experimental setup. There, in contrast to this work and the work of Gu et al., no EBIT was used for ion production but an ion beam was generated which was brought to overlap with the photon beam over a distance of $60\,\mathrm{cm}$ [33]. The photoionization resulting from this overlap was then measured. Since there are only ions with a certain q/m ratio in the ion beam, only transitions of this HCI can be used as calibration lines. This limitation in the choice of calibration lines complicates the calibration and leads to a larger error.

So far, the results of BT1 and BT2 have not taken into account systematic errors that affect both the calibration lines and the resonance $O^{4+}_{K_\alpha}$ itself. These systematic errors must be added to the statistical error given in the table 9. The largest systematic error can be assumed to be the angular interpolation encoder error ΔE_{AE}. This error describes the fluctuating change in the difference between the actual photon energy and the required energy of the monochromator. The differences can vary depending on the energy that is set. The deviation is due to interpolation functions, which are necessary because the demanded angular changes of the monochromator are too small in relation to the reference points in the measuring device. In addition, the return value of the encoders varies slightly when the angle is kept constant, which are also included in the angular encoder error. This error causes a degradation of the resolution with which the calibration lines can be measured, but also affects the linear calibration, since the calibration points no longer lie on a linear curve due to the energy-dependent error. To minimise at least one of the two angular encoder errors (mirror and grating), the plane mirror angle was fixed. This reduces the total error of the two angular encoder errors and increases the resolutions significantly. The energy depend angular encoder error can be measured with a photoelectron spectrometer as shown in the work of S. Kühn [26]. The error of the encoder can be estimated up to $\Delta E_{\mathrm{AE}} = 100\,\mathrm{meV}$.
Due to the mirror angle being optimised and fixed to a certain photon energy, an additional systematic error, the defocussing effect, occurs when the energy changes. This is due to the fact that the photon beam no longer optimally hits the exit slit, which can also influence the nominal energy. Also energy shifts occuring over time, such as the beamline shift, must be taken into account, which can be estimated with $\Delta E_{\mathrm{Shift}} = 10\,\mathrm{meV}$ upwards.
Despite these systematic errors and the large error of McLaughin et al. [33], the results of BT1 do not agree with the reference values. The values of BT2 indeed agree with the reference [33], but can only be compared with other results to a limited extent. The choice and quantity of calibration lines with their corresponding theoretical reference values plays a crucial role in the quality of a calibration. The more precise the calibration lines can be measured and the more accurate the corresponding reference value is, the better the calibration. For example, the O_2 measurement in BT2 is only suitable as a calibration line to a very limited extent because both the measured value and the (experimental) reference value have a comparatively large error. The fact that only two and different calibration lines were used in BT2 worsens the comparability, as for example the angular encoder error can be different for the calibration lines used. Furthermore, the assumption of constant slope can be questioned. The energy differences between the nominal energies of the calibration lines in BT1 and BT2 are not shifted by a constant offset. Either it has to be assumed that the slope of the calibration also changes or systematic effects that have taken place between the two beamtimes have to be taken into account. Since the reliability of the calibration of BT2 must be questioned due to the problems described above, only the results of BT1 can be compared with the references.

In conclusion, it can only be said that the results of this work differ significantly from the existing experimental references. To confirm this discrepancy, further measurements must be conducted. This would require several complete calibrations (with slope and offset), keeping the number and selection of calibration lines constant (in contrast to BT1 and BT2) in order to optimally compare the obtained resonance results. The choice of theoretical reference values also needs to be re-examined. To reduce systematic effects, especially the energy dependency of the angular encoder error, the error of the encoder would have to be reduced by determining the actual photon energy with a photoelectron spectrometer.

Isotope shift The second aim of this work was to measure the isotope shift of O_{16}/O_{18} using the resonant photoionization of the K_α-line of Be-like oxygen. In contrast to the energy determination, the isotopic shift can be determined exclusively in the ion data, since the transition $O^{4+}_{K_\alpha}$ must be resolved separately for each of the two ions. The isotope shift is then simply formed by the difference of the two excitation energies O^{4+}_{16} and O^{4+}_{18}. In principle, the isotope shift does not need to be calibrated, since a good relative energy calibration between the two nominal resonance energies can be assumed and the calibration becomes obsolete due to the difference. Since this shift, which was calculated with the felxible atomic code (FAC), is just $1.9\,\mathrm{meV}$, the resonance energies must be determined with the highest possible precision in order to measure it at all. However, the signal strength of the O^{5+}_{18} ions in the time-of-flight spectrum produced during photoionization is very weak and is often overlaid by electronic artefact signals from other larger peaks. Therefore, in this work, a signal model was developed to fit any time-of-flight spectrum. This signal model manages to separate the influences of individual HCI from each other in contrast to the gaussian model used so far and thus to increase the relative signal strength of the signal. At the same time, the statistical significance is increased, as two resonance energies per HCI can be determined for each scan examined.

With the help of this model fit, for a total of 18 scans, two resonance energies could be determined for each of the two isopes O_{16}/O_{18}. These energies were converted into an isotope shift using two methods. Either a mean resonance energy is first determined for both isotopes (O^{4+}_{16} and O^{4+}_{18}), which are then used to calculate the isotope shift via their difference (method 1). Conversely, in a second method, the two energy differences of the two isotopes were first calculated for each scan. The isotope shift can then be determined by averaging these energies. The method of averaging was again carried out in two ways. One is a weighted mean value and the other is by a histogram in which all the energy differences are ploted. The centroid of the normal distribution is obtained by a least square fit of a gaussian profile.
Table 10 shows the comparison between the isotope shifts determined using these methods.

Table 10: Comparison of the isotope shift determined by two different methods. In each method, two types of averaging were used: Histogram and weighted mean.

Method	Histogram	Weighted average
1	$3.9 \pm 1.8\,\mathrm{meV}$	$1.5 \pm 1.2\,\mathrm{meV}$
2	$2.6 \pm 1.8\,\mathrm{meV}$	$2.8 \pm 1.0\,\mathrm{meV}$

All determined results for the isotope shift agree within the error with the result of $1.9\,\mathrm{meV}$ calculated by FAC (see in table 3). The isotope shift determined by method 2 and the weighted mean has the smallest error. The weighted mean has the major advantage over the histogram that the individual error of the determined single resonance energy or the difference energy is taken into account. Since the errors

of the individual resonance energies according to table 8 are higher than the expected shift, this is a considerable limitation. The fact that, due to the small number of events, the error of the histogram fit depends strongly on the choice of bin size is also a disadvantage. Nevertheless, the histogram has the advantage of taking the expected statistical normal distribution into account in the fit. If more individual scans were available and the error would be smaller than the bin size, so that the histogram fit could be weighted with an error, both of these problems could be solved. If the resonance energies of both HCI had only statistical errors, one would expect method 1 and 2 to give the same result. The difference between method 1 and 2 is that possible systematic errors leading to an energy shift between scans (e.g. the shift of beam energy) are not taken into account in method 2 in contrast to method 1. Since the gaussians and ringdown signals are produced with the same nominal energy, their influence is eliminated by the difference formation. All this explains why the isotope shift determined with method 2 and the weighted mean is the best result and has the smallest error, which, however, is still very large at 35%.

The reason for this large error is the inaccurate determination of the individual resonance energies of O_{16}^{4+} and O_{18}^{4+}. The mean single error of the resonance energies of $2.6 - 8.7\,\mathrm{eV}$ is higher than the shift to be determined (see table 8). A high resolution is crucial for the exact determination of the centroid energies. This is for all determined resonances with ≈ 4000 clearly lower than the maximum possible resolution of the gas phase beamline with almost 9000 (see section 5.5.2). The resolution could be increased by a smaller slit width, however, only at the expense of the flux. A smaller flux means less Li-like oxygen ions O^{5+} produced by photoionization and thus a weaker signal. If the signal is too weak, the influences of the individual peaks (especially the small ones) can no longer be properly fitted, so that the error of the centroid determination becomes significantly larger again.
Since O_{18} has an extremely weak signal, the resolution cannot be improved even more at the expense of the flux, as is possible with an O_w measurement due to the high effective cross-section. The GasPhase beamline delivers the maximum flux in the energy range of about $100\,\mathrm{eV}$ and loses beamline efficiency significantly at higher energies (see chapter 4.2). In comparison, the P04 beamline at the PETRA III synchrotron in Hamburg would be better suited in the investigated energy range of $550\,\mathrm{eV}$, since significantly higher fluxes ($> 10^{12}\,\mathrm{photons/s}$ compared to $> 10^{10}\,\mathrm{photons/s}$ at the GasPhase) and above all significantly higher maximum resolutions of > 30000 are possible [39].

In any case, the result provides a good estimate of the isotope shift and confirms the expectation of the calculated FAC value. It can also be stated that this shift can be clearly attributed to $O_{16}/\ O_{18}$, since all influences of other peaks could be removed with the help of the model fit, which has been developed in the framework of this thesis. Since the fit model provides two resonace energies for each scan and HCI (Gaussian and ring down component - see section 5.4.3), the statistical relevance can be increased.
For future beamtimes, it is suggested to choose another synchrotron source, which has higher flux rates and resolution in the used energy range of $530\,\mathrm{eV}$ - $575\,\mathrm{eV}$. Then, in combination with a larger measurement series, the isotope shift could be measured more easily and more precisely. Then it would also be possible to investigate the low-charged states of oxygen (B-like and C-like oxygen), which are also relevant for astrophysical models. These could not be measured in this experiment because the flux is too low and their effective cross-section is too small. In the case of measuring C-like oxygen, an isotope shift could then also be tried to be measured. For B-like oxygen O^{3+} this cannot be done, because O_{16}^{4+}, which is produced by photoionization, cannot be distinguished from C_{12}^{3+}. With the help of these measurements, the signal model could also be further tested and optimized.

References

[1] A. Kramida et al. NIST Atomic Spectra Database (ver. 5.9), [Online]. Available: https://physics.nist.gov/asd [2022, April 7]. National Institute of Standards and Technology, Gaithersburg, MD. 2021.

[2] Thompson/Vaughan/Kirz/Attwood/ et. al. *X-ray Data Booklet. Lawrence Berkeley National Laboratory Second edition*. Accessed on: 14.04.2022. Jan. 2001.

[3] Peter Beiersdorfer and Ming Feng Gu. "K-shell Emission from O vi Near 19 Å". In: 931.1 (May 2022), p. 49. DOI: 10.3847/1538-4357/ac5684.

[4] Christian Beilmann. "Über die Stärke mehrelektronsicher Resonanzen bei der Photorekombination und -ionisation". PhD thesis. 2012.

[5] Sven Bernitt. "Resonante Anregung astrophysikalischer Röntgen-Übergänge in hochgeladenen eisenionen mit dem Freie-Elektronen-Laser LCLS". PhD thesis. 2013.

[6] R.R Blyth et al. "The high resolution Gas Phase Photoemission beamline, Elettra". In: *Journal of Electron Spectroscopy and Related Phenomena* 101-103 (June 1999), pp. 959–964. DOI: 10.1016/s0368-2048(98)00381-8.

[7] N. Bohr. "I. On the constitution of atoms and molecules". In: *The London, Edinburgh, and Dublin Philosophical Magazine and Journal of Science* 26.151 (July 1913), pp. 1–25. DOI: 10.1080/14786441308634955.

[8] K Codling. "Applications of synchrotron radiation (ultraviolet spectral light source)". In: *Reports on Progress in Physics* 36.5 (May 1973), pp. 541–624. DOI: 10.1088/0034-4885/36/5/002.

[9] M Coreno et al. "Vibrationally resolved oxygen $K \rightarrow \Pi^*$ spectra of O2 and CO". In: *Chemical Physics Letters* 306.5 (1999), pp. 269–274. ISSN: 0009-2614. DOI: https://doi.org/10.1016/S0009-2614(99)00468-6. URL: https://www.sciencedirect.com/science/article/pii/S0009261499004686.

[10] Wolfgang Demtröder. *Experimentalphysik 3*. Springer-Verlag GmbH, June 2016. 588 pp. ISBN: 9783662490945. URL: https://www.ebook.de/de/product/27952543/wolfgang_demtroeder_experimentalphysik_3.html.

[11] Wolfgang Demtröder. *Laserspektroskopie Grundlagen und Techniken*. BerlinHeidelbergNew York: Springer, 2007. ISBN: 9783540337928.

[12] Stepan Dobrodey. "Charge-exchange studies of bare and hydrogen-like low-Z ions in the X-Ray and extreme-ultraviolet ranges inside an electron beam ion trap". PhD thesis. 2019.

[13] Joseph Fraunhofer. "Bestimmung des Brechungs- und des Farbenzerstreungs-Vermögens verschiedener Glasarten, in Bezug auf die Vervollkommnung achromatischer Fernröhre". In: *Annalen der Physik* 56.7 (1817), pp. 264–313. DOI: 10.1002/andp.18170560706.

[14] *Fundamental Physics in Particle Traps*. Springer-Verlag GmbH, Jan. 2014. 411 pp. ISBN: 9783642452017. URL: https://www.ebook.de/de/product/25047319/fundamental_physics_in_particle_traps.html.

[15] R. GIACCONI, H. GURSKY, and J. R. WATERS. "Spectral Data from the Cosmic X-Ray Sources in Scorpius and Near the Galactic Centre". In: *Nature* 207.4997 (Aug. 1965), pp. 572–575. DOI: 10.1038/207572a0.

[16] J D Gillaspy. "Highly charged ions". In: *Journal of Physics B: Atomic, Molecular and Optical Physics* 34.19 (Sept. 2001), R93–R130. DOI: 10.1088/0953-4075/34/19/201.

[17] M F Gu. "The flexible atomic code". In: *Canadian Journal of Physics* 86.5 (May 2008), pp. 675–689. DOI: 10.1139/p07-197.

[18] Ming Feng Gu et al. "Laboratory Measurement and Theoretical Modeling of K-Shell X-Ray Lines from Inner-Shell Excited and Ionized Ions of Oxygen". In: *The Astrophysical Journal* 627.2 (July 2005), pp. 1066–1071. DOI: 10.1086/430666.

[19] D.E. Harris and D. Irwin. *Einstein Observatory Revised User's Manual. Harvard-Smithsonian Center for Astrophysics,*. 1984. URL: https://heasarc.gsfc.nasa.gov/docs/einstein/RUM_Chapter1-2.pdf.

[20] D. R. Hartree. "The Wave Mechanics of an Atom with a Non-Coulomb Central Field. Part I. Theory and Methods". In: *Mathematical Proceedings of the Cambridge Philosophical Society* 24.1 (Jan. 1928), pp. 89–110. DOI: 10.1017/s0305004100011919.

[21] Gabriel Herrmann. "Optical Theory of Thermal Velocity Effects in Cylindrical Electron Beams". In: *Journal of Applied Physics* 29.2 (Feb. 1958), pp. 127–136. DOI: 10.1063/1.1723053.

[22] D. S. Hughes and Carl Eckart. "The Effect of the Motion of the Nucleus on the Spectra of Li I and Li II". In: *Physical Review* 36.4 (Aug. 1930), pp. 694–698. DOI: 10.1103/physrev.36.694.

[23] Zoltan Hárman (Chapter 10) José R. Crespo López-Urrutia. *The Physics of Multiply and Highly Charged Ions: Volume 1: Sources, Applications and Fundamental Processes*. SPRINGER NATURE, Sept. 2003. 389 pp. ISBN: 1402015658. URL: https://www.ebook.de/de/product/3881376/the_physics_of_multiply_and_highly_charged_ions_volume_1_sources_applications_and_fundamental_processes.html.

[24] G. Kirchhoff and R. Bunsen. "XLII Chemical analysis by spectrum-observations.—Second memoir". In: *The London, Edinburgh, and Dublin Philosophical Magazine and Journal of Science* 22.148 (Nov. 1861), pp. 329–349. DOI: 10.1080/14786446108643164.

[25] Ernst H. Krause. "High Altitude Research with V-2 Rockets". In: *Proceedings of the American Philosophical Society* 91.5 (1947), pp. 430–446. ISSN: 0003049X. URL: http://www.jstor.org/stable/3143424 (visited on 06/12/2022).

[26] Steffen Kühn. "High-precision soft X-ray transition measurements of neon-like mid-Z ions using ultra monochromatic synchrotron." PhD thesis. 2021.

[27] Steffen Kühn. "Inbetriebnahme und Charakterisierung einer Elektronenkanone mit optischem Zugang zur Strahlachse in einer kompakten Elektronenstrahlionenfalle". MA thesis. 2017.

[28] Steffen Kühn et al. "High Resolution Photoexcitation Measurements Exacerbate the Long-Standing Fe XVII Oscillator Strength Problem". In: *Physical Review Letters* 124.22 (June 2020), p. 225001. DOI: 10.1103/physrevlett.124.225001.

[29] P. Lechner et al. "Silicon drift detectors for high count rate X-ray spectroscopy at room temperature". In: *Nuclear Instruments and Methods in Physics Research Section A: Accelerators, Spectrometers, Detectors and Associated Equipment* 458.1-2 (Feb. 2001), pp. 281–287. DOI: 10.1016/s0168-9002(00)00872-x.

[30] M. A. Leutenegger et al. "High-Precision Determination of Oxygen Kα Transition Energy ExcludesIncongruent Motion of Interstellar Oxygen". In: *Physical Review Letters* 125.24 (Dec. 2020), p. 243001. DOI: 10.1103/physrevlett.125.243001.

[31] Wolfgang Lotz. "An empirical formula for the electron-impact ionization cross-section". In: *Zeitschrift für Physik* 206.2 (Apr. 1967), pp. 205–211. DOI: 10.1007/bf01325928.

[32] Wolfgang Lotz. "Electron-impact ionization cross-sections and ionization rate coefficients for atoms and ions from hydrogen to calcium". In: *Zeitschrift für Physik* 216.3 (June 1968), pp. 241–247. DOI: 10.1007/bf01392963.

[33] B. M. McLaughlin et al. "K-shell photoionization of O4 + and O5 + ions: experiment and theory". In: *Monthly Notices of the Royal Astronomical Society* 465.4 (Nov. 2016), pp. 4690–4702. DOI: 10.1093/mnras/stw2998.

[34] P. Melpignano et al. "Optimization of spherical grating monochromators operating with variable included angle for different applications". In: *Review of Scientific Instruments* 66.2 (Feb. 1995), pp. 2125–2128. DOI: 10.1063/1.1145748.

[35] P. Micke et al. "The Heidelberg compact electron beam ion traps". In: *Review of Scientific Instruments* 89.6 (June 2018), p. 063109. DOI: 10.1063/1.5026961.

[36] F. Nicastro et al. "Observations of the missing baryons in the warm–hot intergalactic medium". In: *Nature* 558.7710 (June 2018), pp. 406–409. DOI: 10.1038/s41586-018-0204-1.

[37] Fabrizio Nicastro, Smita Mathur, and Martin Elvis. "Missing Baryons and the Warm-Hot Intergalactic Medium". In: *Science* 319.5859 (Jan. 2008), pp. 55–57. DOI: 10.1126/science.1151400.

[38] Rosario Soria Orts. "Isotopic effect in B-like and Be-like argon ions". PhD thesis. 2005.

[39] *P04 - Beamline Performance*. Accessed on: 18.06.2022. URL: https://photon-science.desy.de/facilities/petra_iii/beamlines/p04_xuv_beamline/beamline_parameters/index_eng.html.

[40] Frederik B.S. Paerels and Steven M. Kahn. "High-Resolution X-Ray Spectroscopy with Chandra and XMM-Newton." In: *Annual Review of Astronomy and Astrophysics* 41.1 (Sept. 2003), pp. 291–342. DOI: 10.1146/annurev.astro.41.071601.165952.

[41] Max Planck. "Ueber das Gesetz der Energieverteilung im Normalspectrum". In: *Annalen der Physik* 309.3 (1901), pp. 553–563. DOI: 10.1002/andp.19013090310.

[42] E. Rutherford. "LXXIX. The scattering of α and β particles by matter and the structure of the atom". In: *The London, Edinburgh, and Dublin Philosophical Magazine and Journal of Science* 21.125 (May 1911), pp. 669–688. DOI: 10.1080/14786440508637080.

[43] Maria Santos-Lleo et al. "The first decade of science with Chandra and XMM-Newton". In: *Nature* 462.7276 (Dec. 2009), pp. 997–1004. DOI: 10.1038/nature08690.

[44] E. Schrödinger. "Quantisierung als Eigenwertproblem (I+II)". In: *Annalen der Physik* 384.4/6 (1926), pp. 361–376 / 489–527. DOI: 10.1002/andp.19263840404.

[45] E. Schrödinger. "Quantisierung als Eigenwertproblem (III)". In: *Annalen der Physik* 385.13 (1926), pp. 437–490. DOI: 10.1002/andp.19263851302.

[46] E. Schrödinger. "Quantisierung als Eigenwertproblem (IV)". In: *Annalen der Physik* 386.18 (1926), pp. 109–139. DOI: 10.1002/andp.19263861802.

[47] Carlo Meneghini Settimio Mobilio Federico Boscherini. *Synchrotron Radiation*. Springer-Verlag GmbH, Aug. 2014. 799 pp. ISBN: 9783642553158. URL: https://www.ebook.de/de/product/23042819/synchrotron_radiation.html.

[48] C. David Sherrill and Henry F. Schaefer. "The Configuration Interaction Method: Advances in Highly Correlated Approaches". In: *Advances in Quantum Chemistry*. Elsevier, 1999, pp. 143–269. DOI: 10.1016/s0065-3276(08)60532-8.

[49] J. J. Thomson. "XL. Cathode Rays". In: *The London, Edinburgh, and Dublin Philosophical Magazine and Journal of Science* 44.269 (Oct. 1897), pp. 293–316. DOI: 10.1080/14786449708621070.

[50] M. Togawa et al. "Observation of strong two-electron–one-photon transitions in few-electron ions". In: *Physical Review A* 102.5 (Nov. 2020), p. 052831. DOI: 10.1103/physreva.102.052831.

[51] Moto Togawa. "Investigation of the M-shell unresolved transition array of aluminium-like iron using monochromatic soft x-ray synchrotron radiation". MA thesis. 2021.

[52] I. I. Tupitsyn et al. "Relativistic calculations of isotope shifts in highly charged ions". In: *Physical Review A* 68.2 (Aug. 2003), p. 022511. DOI: 10.1103/physreva.68.022511.

[53] *Webside: Elettra Gasphase Beamline - Trieste, Italy*. Accessed on: 14.03.2022. URL: https://www.elettra.trieste.it/lightsources/elettra/elettra-beamlines/gas-phase/bl-description.html.

[54] *Webside: Elettra Machine - Trieste, Italy*. Accessed on: 14.03.2022. URL: https://www.elettra.trieste.it/lightsources/elettra/machine.html.

[55] *Webside: Rigaku - Synchrotron and beamline components*. Accessed on 24.05.2022. URL: https://www.rigaku.com/sites/default/files/2020-10/Synchrotron_Industry_800x600.jpg.

[56] G.R. Wight and C.E. Brion. "K-shell excitations in NO and O2 by 2.5 keV electron impact". In: *Journal of Electron Spectroscopy and Related Phenomena* 4.4 (Jan. 1974), pp. 313–325. DOI: 10.1016/0368-2048(74)80062-9.

[57] V. A. Yerokhin and A. Surzhykov. "Theoretical Energy Levels of 1sns and 1snp States of Helium-Like Ions". In: *Journal of Physical and Chemical Reference Data* 48.3 (Sept. 2019), p. 033104. DOI: 10.1063/1.5121413.

[58] V. A. Yerokhin, A. Surzhykov, and A. Müller. "Relativistic configuration-interaction calculations of the energy levels of the 1s22l and 1s2l2l′ states in lithiumlike ions: Carbon through chlorine". In: *Physical Review A* 96.4 (Oct. 2017), p. 042505. DOI: 10.1103/physreva.96.042505.

Acknowledgments

At the end of this thesis, I would like to thank all the people who helped me to write this thesis. In particular, I would like to thank Prof. Dr. Jośe Crespo Lopez Urrutia, who made me aware of both the highly interesting topic of the EBITs and the MPIK through his seminar "Schlüsselexperimente der Quantenphysik". I also want to thank him for the opportunity to have conducted this experiment at the Elettra synchrotron in Italy. Also, many thanks to all the people who were involved in this experiment. Furthermore, I would like to thank Moto Togawa, who provided me with detailed supervision during my bachelor thesis and many suggestions for improving the work. Last but not least, I would like to thank all the people from the Studentenbüro and my family who have supported me during this time.

Erklärung

Ich versichere, dass ich diese Arbeit selbstständig verfasst und keine anderen als die angegebenen Quellen und Hilfsmittel benutzt habe.

Heidelberg, den 20.06.2022

Jonas Danisch